

A 1000 kV TEM Running Over 25 Years



Gerhard Kästner and Ulrich Messerschmidt

Max Planck Institute of Microstructure Physics, Halle (Saale)

A JEOL 1000 kV High-Voltage Electron Microscope has been running since 1971 when it was installed in Halle (Saale), Germany, with 280 thousand micrographs being exposed up to now .

1. Background

Halle (Saale) is an old university town located in the former East Germany (German Democratic Republic, GDR). It was in the late 60s when economy was rapidly growing even in a socialist country like the GDR. Governmental research funds were provided to expand the facilities and staff of the Academy of Sciences of the GDR. An institute belonging to this academy, the Institute of Solid State Physics and Electron Microscopy, had been established in Halle (Saale) in 1959 by Heinz Bethge. Owing to his activity and the scientific reputation of the institute, it was possible to raise the necessary amount of money for buying a JEOL high-voltage transmission electron microscope (HVEM), serial # 6, operated at 1000 kV. Worldwide, there were about 30 HVEMs running in the 70s — mainly in Japan, the UK, and the U.S.A., among them two in Stuttgart/Germany and one each in Stockholm/Sweden, Moscow/USSR and Halle (Saale) /GDR.

The HVEM in Halle (Saale) — shown in **Fig. 1** — was installed in a new dedicated building between 1970 and 1971. From the very beginning of constructional work, a staff of a leading scientist (one of the authors, G. K.), two technicians, and an increasing number of scientific co-workers were involved in all details. It was very stimulating to assist the Japanese team of up to five engineers in the assembly and during the test period of all parts of the big machine. Various provisional installations had to be made, including a wooden 1 m² basement for a heavy (1000 kg) motor-generator supplying the 3 kHz input of the high-voltage system. When connecting this provisional installation for the first time, all persons kept at a safe distance of several meters. Right from the beginning, the staff was involved in all details of the later operation, including the scheduled annual overhaul, according to a five-year contract with JEOL. Subsequently,

the staff was able to overhaul the whole system — including the complete disassembly and cleaning of the high-voltage system and the accelerator tube — with only occasional help by JEOL. This was essential as it saved much money in convertible currency, which was very rare in the GDR. Later on, it turned out that the accelerator was working well for several years without cleaning, and the annual downtime for repair and cleaning other parts was reduced to about 3 weeks. Up to now, more than 280,000 micrographs have been exposed.

In general, it was advantageous to have an experienced team of permanent employees. Thus, a lot of difficulties could be solved which arose from the chronic shortage of materials and convertible currency typical of all socialist economies. Two examples may be mentioned: After running the microscope for about 6 years, a set of 20 spare insulators for the 1 MV accelerating vacuum tube was managed to be produced in a GDR factory according to drawings kindly provided by JEOL. It was a similar but more tedious in-house work to design and build a new 1 MV resistor column — located within the high-voltage gas-pressurized tank — as the measuring resistor to provide the feedback voltage for the 1 MV voltage control and stabilization circuit. After several trials, the 14 stages of this column were built from 4480 thin-film resistors individually pre-tested. This resistor column has been working well for 4 years.

The background changed drastically after the reunification of Germany in 1990. Since 1992, the HVEM facility has been part of the new Max Planck Institute of Microstructure Physics established in Halle with the directors of the experimental departments Ulrich Gösele and Jürgen Kirschner. The instrument has now mainly been used for *in situ* investigations. Accordingly, the responsibility has been passed to the other author (U. M.). Owing to the skill of Christian Dietzsch (physicist) and Wolfgang Greie (technician), both from the most experienced former staff, all technical problems and breakdowns have been solved

without help from outside so that the microscope is still working stably most of the time. Because of the still high demand for conventional applications and, particularly, because of the unique possibilities of *in situ* experiments, it is planned to maintain the instrument also over the next few years.

2. Technical upgrade and *in situ* facilities

Because of the low budget of convertible currency available during GDR times, the HVEM was bought at a very low price level so that its technical facilities had to be upgraded and expanded in various ways. Nearly all improvements were laboratory-made in order to achieve unique facilities.

2.1. Upgrade

At the very beginning, two upgrades badly needed were done: a film numbering device (where an electromechanical display is optically exposed) and an automatic starting unit, switching on the pumps, etc. after sudden power cuts (which were quite often during construction work within the campus). This starting unit was built by using electromechanically driven switches since no IC's were available. In addition, the noisy 3 kHz transformers of the high-voltage supply were put in insulating boxes (and therefore water-cooled) to ensure sound protection.

Later on a TV system was installed, consisting of a transmission fluorescent screen, a 45° mirror, a lens-coupled TV camera, and an extension of the X-ray lead shielding.

A quite useful feature of the HVEM is the large diameter (about 300 mm) of its specimen chamber as well as the diameter of 36 mm of the upper bore of the top-entry objective pole piece. This provides enough room for attaching special cartridges and devices.

A precise universal goniometer was built in 1977 by one of the authors (G. K.) in order to improve and expand the routine facilities for using electron diffraction and diffraction contrast. First, the specimen airlock and top-entry

Halle (Saale), D-06120, Germany
E-mail: kaestner@mpi-halle.mpg.de

transfer were completely redesigned to better manipulate a new standard specimen cartridge for larger samples. It may clamp specimens of up to 8 mm in diameter and 1 mm in height. This cartridge also enables double-tilting of up to 45° at all azimuth angles by means of the top-entry goniometer mechanism shown in Fig. 2. The cone-shaped specimen cartridge C (shown separately on the right) is kept by a cartridge holder H, which is supported by a universal joint precisely located within the specimen plane of the objective lens. At about 13 mm above this plane, a small brass ball is fixed to the cartridge holder (below the letter H). This ball is gripped between actuating tongs T, each arm coupled to a horizontal gear drive G. On moving these drives into opposite directions, the opening angle of the tongs is varied, thus tilting the cartridge in y direction. If the drives are moved synchronously into the same direction, the tongs translates without altering the angle, thus tilting the cartridge in x direction. Tilt angle and azimuth are displayed in two dimensions on a screen in front of the

operator. This screen is shown as a bright area above the viewing chamber in Fig. 1. It is connected to the vertical tilting drive rods with their handle knobs conveniently located on the left and right sides of the viewing window.

2.2. In-situ facilities

Together with the microscope, various top-entry attachments for *in situ* investigations were bought:

Specimen heating stage:

An airlock-exchangeable specimen cartridge can be resistance-heated up to 1070 K and tilted up to 30° in any direction.

Specimen cooling stages:

Airlock-exchangeable specimen cartridges can be cooled by liquid N₂ down to 150 K with double-tilting facilities up to 10°, or down to 120 K without tilting.

Transversal magnetic field stage:

On inserting this stage into a specially shielded objective pole piece, a horizontal magnetic field of up to 30 kA/m can be applied across the specimen plane and rotated mechanically

into all azimuths.

Tensile stage:

A specimen can be fixed to a non-tiltable stage where a blade spring extends the specimen, controlled by heating a wire.

After some years of work and respective experience, a number of new stages were laboratory-made in order to meet particular requirements and to extend the facilities.

2.2.1. Heating/tilting stage

To attain higher temperatures, a new stage was built in 1983 [1] where the tantalum/molybdenum specimen cartridge is heated by electron bombardment from a surrounding W filament, a method which was introduced into the design of *in situ* stages by Fujita and Komatsu [2]. The cartridge holder, including the filament heating and high-voltage leads as well as water cooling and a thermocouple, can be double-tilted up to 23° via the tongs mechanism shown in Fig. 2. The cartridge itself is exchangeable via the redesigned specimen airlock transfer mechanism. Temperatures of



Fig.1. The JEOL 1000 kV high-voltage transmission electron microscope installed in Halle (Saale), Germany.



Fig.2. Laboratory-made universal 45° double-tilting stage viewed from the top. The specimen cartridge C shown separately is airlock-transferred to the cartridge holder H. It is tilted on moving the tongs T by means of gears G (G. Kästner, 1977).

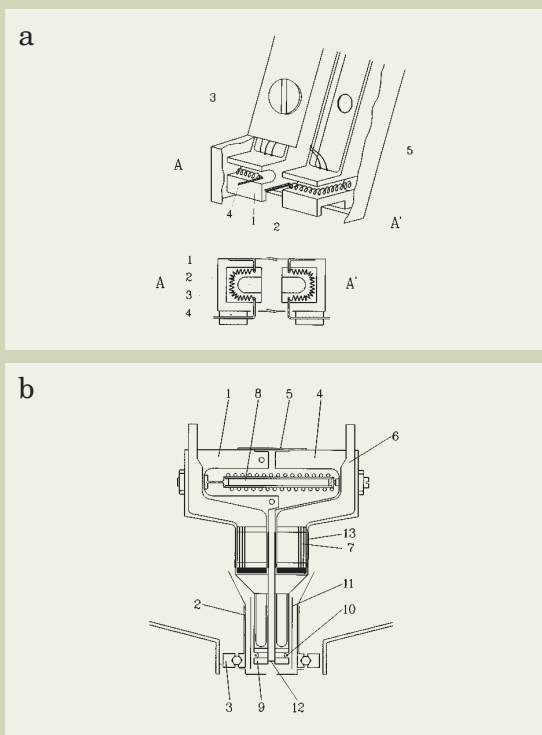


Fig.3. Schematic drawing of the double-tilting high-temperature straining stage. a) Perspective view of the hot zone. 1 - specimen grips, 2 - coil filaments, 3 - thermal shields, 4 - electric connections of filaments. b) Drive and cooling system. 1 - fixed lever, 2 - tilted cone carrying the deformation device, 3 - ring of cardanic suspension of the double-tilting stage, 4 - moveable lever, 5 - leaf spring, 6 - cooling water pipe, 7 - lamellae heat exchangers, 8 - stainless steel tube with heating coil, 9 - W-27Re specimen grips, 10 - W filaments, 11 - thermal shields, 12 - specimen, 13 - semiconducting strain gauges (U. Messerschmidt, 1994, after [4]).

1470 K were routinely applied.

2.2.2. Quantitative straining/tilting stage

A double-tilting straining stage was designed in 1975 [3]. Double-tilting of about 23° in most azimuth directions is possible owing to design features similar to those of the universal goniometer described above. The deformation is driven by the thermal expansion of an aluminium rod operating against a water cooling system. The displacement is transmitted to the specimen grips and enlarged by two symmetrical levers resulting in a relatively high elastic stiffness and a smooth action. Two full bridges of semiconducting strain gauges allow the measurement of load and specimen elongation. These features are sometimes necessary for interpreting the results, e.g., during unloading studies, but are always very helpful in performing the experiments.

2.2.3. High-temperature straining/tilting stage

To enable the study of the plastic deformation of high-temperature materials, including ceramics, a stage was designed for temperatures above 1300 K using again electron bombardment to heat the specimen grips [4]. Fig. 3 shows an outline of this stage. Two small coil filaments (2 in Fig. 3a) are attached to the thermal shields (3). The electron current hits the specimen grips (1 in Fig. 3a, 9 in Fig. 3b). As for the room temperature stage described in the foregoing section, the deformation is driven by thermal expansion, this time of a stainless steel tube (8 in Fig. 3b). The load is transmitted to the specimen (12) by a fixed (1) and a movable lever (4). The heat of the thermal drive and of the hot specimen grips is carried off by water pipes (6) and small lamellae heat exchangers (7). The load is measured by a full bridge of semiconducting strain gauges (13). The whole stage is controlled via a personal computer. It has a maximum load of 15 N. Experiments have been performed at grip temperatures of up to 1520 K.

2.2.4. Electric fields

The 45° goniometer shown in Fig. 2 has been equipped with electrical contacts and with a special cartridge that allows one to apply a voltage of up to 1 kV to the specimen.

An attachment was built where the specimen is a fine metal tip which can be wetted with a liquid metal. On applying high voltage to the tip, one can observe the field-induced formation of a liquid metal cone. Image distortion by the electric field of the tip is reduced owing to the high acceleration voltage of the microscope.

2.2.5. Transverse bending stage

A bending stage was designed by Eckhard Langner of the Halle Branch of the Fraunhofer Institute of Mechanics of Materials in about 1993. The stage was mainly used to study the dislocation generation at cracks in silicon.

2.2.6. Environmental cell

To study the oxidation of metals, an environmental cell was designed for the HVEM [5]. To separate the gas near the specimen from the vacuum of the microscope, a differ-

ential pumping system with two inner and outer apertures each is applied using an additional turbo pump. The specimen is heated by a small furnace of alumina carrying a platinum heating coil. The system allows gas pressures between 10^{-3} and 150 Pa and temperatures above 1300 K.

The *in situ* techniques of the Halle HVEM are open for the cooperation with guest scientists from other institutions.

3. Scientific output

3.1. Further education

The facilities reported above as well as further instruments of the institute comprising scanning and high-resolution transmission electron microscopy soon became attractive to researchers not only of the GDR but of various formerly socialist countries. Consequently, an

"International Centre of Electron Microscopy of the Socialist Countries" at the Institute of Solid State Physics and Electron Microscopy in Halle (Saale) was initiated in 1975 by Heinz Bethge, the director of the institute. The centre coordinated scientific collaboration and organized annual spring and autumn schools for training electron microscopists. The center was headed by H. Bethge from 1975 to 1984 and by J. Heydenreich from 1984 to 1995. The centre was supervised by a Scientific Council of scientists from the member countries. This framework was also useful to overcome the stringent governmental restrictions on inviting scientists and lecturers from non-socialist countries. A total number of about 35 autumn or spring schools, resp., with 100 participants on an average, were held until 1995, including two International Symposia (in 1979, on *In*



Fig.4. Thin section of high-impact polystyrene: Tensional strain (applied in vertical direction) is elongating the globular rubber particles P (of about $2 \mu\text{m}$ in size) and opening crazes (bright, horizontal layers). Within each craze, fine fibrillae represent polystyrene heavily elongated by strain. Without the optimized fraction of rubber particles, the crazes would elongate catastrophically until the material breaks (G. Michler, 1976).



Fig.5. Liquid-crystal thin film prepared by vapour deposition onto a carbon film. The rod-shaped organic molecules of $\text{C}_7\text{H}_{15}\text{O}-\text{C}_6\text{H}_4-\text{CH}=\text{N}-(\text{C}_6\text{H}_4)_2-\text{CN}$ are hexagonally packed within smectic layers of finite grain size. Overlapping layers give rise to Moiré patterns. Accelerating voltage 1000 kV (G. Kästner, Ch. Dietzsch, 1980).

situ High Voltage Electron Microscopy in Materials Science, and in 1989, on Electron Microscopy in Plasticity and Fracture Research of Materials). In 1995, the centre was reorganized by forming an International Centre of Materials Science and Electron Microscopy, supported by the Max Planck Society and headed by Ulrich Gösele.

3.2. Methodical work

Since the HVEM is chiefly applied to study crystal defects by means of diffraction contrast, the operating contrast mechanisms had to be studied both experimentally and theoretically with particular emphasis on many-beam diffraction, on the anomalous absorption of thick specimens, and on kinematical bright-field imaging — a convenient technique similar but complementary to weak-beam dark-field imaging.

A comprehensive theoretical treatment as well as experimental illustrations and tabulated many-beam extinction distances for electron energies of up to 1000 keV are given in [6].

3.3. Routine applications of the HVEM

Because of the activity of the "International Centre of Electron Microscopy", the HVEM facilities in Halle were easily accessible to many scientists from the socialist countries for almost 20 years. Thus, the applications covered a wide field of materials research including semiconductors, metals, ceramics, polymers, and thin films. It would be useless here to refer to the great variety of routine investigations. Instead, two examples of non-standard applications will be given.

Elevated acceleration voltages (electron

energies) reduce the ionizing electron damage to organic specimens. Therefore, an HVEM is useful to transmit such specimens at a reduced damage rate or for a longer time. For this reason, since about 1975 Georg Michler and coworkers (Martin Luther University of Halle (Saale)) [7] performed *in situ* straining experiments on various polymers, using the stage supplied by the manufacturer. **Figure 4** shows an example of these studies.

For the same reason of reduced electron ionization damage, liquid crystals of the smectic type (of low vapour pressure) have been transmitted for the first time [8]. Certain types of dislocations were identified by means of diffraction contrast experiments, and the crystallographic space groups were determined from selected area electron diffraction patterns. An example is given in **Fig. 5**.

3.4. Applications of laboratory-made *in situ* devices

The stages described in Section 2.2 have largely been used to study different topics and materials. Only a few can be mentioned here.

3.4.1. Annealing studies

The high-temperature heating/tilting stage (cf. 2.2.1.) has been used to study various annealing problems, e.g., the recrystallization of ion-implanted silicon. Depending on the implantation conditions (i. e., the ion dose, energy and mass) the crystalline material is damaged (up to amorphization) so that it has to be annealed. **Figure 6** shows the interaction and transformation of dislocations that are created during *in situ* annealing of ion-implanted silicon in an identical specimen area [9]. The antiparallel arrows indicate the transformation of a rod-like defect into an elongated dislocation dipole. Dislocation loops can glide to the surface, dislocation segments of opposite sign interact and annihilate, leading to the intended reduction of the dislocation density.

Solid state reactions were observed in cross section specimens of a TiO_2 layer on an MgO substrate as shown in **Fig. 7**. The interface is sharp at room temperature (R.T.). At about 1000 K a polycrystalline layer of MgTiO_3 forms rapidly followed by the slow growth of a single crystal of the stable phase of Mg_2TiO_4 at higher temperatures [10]. Such processes at temperatures above 1300 K cannot be studied by conventional *in situ* heating stages.

3.4.2. Deformation at room temperature

Very detailed studies were performed on the plastic deformation of magnesium oxide single crystals. As shown in the sequence of images of **Fig. 8**, dislocations bow out between obstacles under load. Due to the cusps, forming at the obstacles, forces are exerted on them. After their thermally activated overcoming, new equilibrium positions are occupied. Detailed quantitative data were obtained from such micrographs and from video recordings, and compared with current theories. These data include the statistical frequency distributions of the distances between the obstacles and the forces acting on them, the distribution of jump distances during motion, the orientation dependence of the line tension of dislocations [11], or radiation-hardening inside the HVEM.



Fig.6. *In situ* annealing of Si implanted with $10^{15} \text{ B}^+/\text{cm}^2$ at 150 keV. Letters designate equal places in b) and c) (D. Hoehl, 1989).

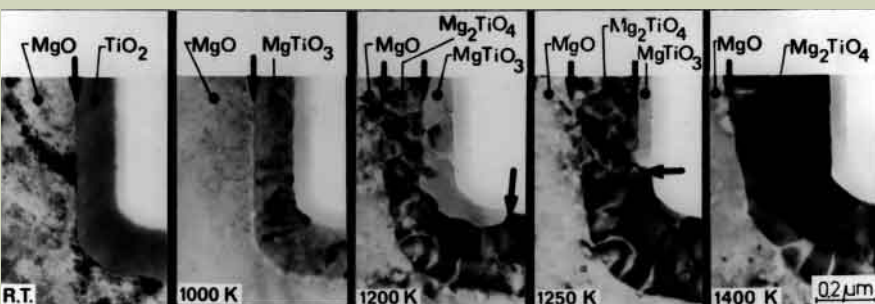


Fig.7. Solid state reactions in a MgO/TiO_2 cross section specimen during *in situ* annealing (D. Hesse, L. Berthold, D. Hoehl, 1994).

Other materials studied comprise Ni, age-hardened Al-Mg-Zn and Al-Ag alloys and Al-Li alloys with precipitates of the ordered phase Al_3Li . The results of the *in situ* experiments yielded quantitative data on the interaction between dislocations and precipitates. In some cases, they showed that the deformation is controlled by other defects than those considered before the results of the *in situ* experiments were known.

3.4.3. Deformation at high temperatures

In situ straining tests at high temperatures were performed on a number of materials including TiAl materials of different microstructures, NiAl, NiAl containing Ta, an oxide dispersion strengthened material, $\text{ZrO}_2\text{-Y}_2\text{O}_3$ alloys of different microstructures, and Al-Pd-Mn single quasicrystals.

$\text{ZrO}_2\text{-Y}_2\text{O}_3$ crystals may contain precipitates of tetragonal crystal structure which form a complicated domain structure. In the so-called t'- ZrO_2 , this domain structure fills the whole crystal volume. During loading at high temperatures, the tetragonal domains may switch the orientations of their c-axes, giving rise to ferroelastic deformation. Fig. 9, taken during *in situ* deformation at 1420 K, shows the original domain structure in strong contrast in the lower part of the figure. The transformed regions form a tetragonal single crystal so that the strong electron microscopy contrast disappears. Details of this ferroelastic deformation are described in [12]. The ferroelastic deformation was proven for the first time also in the tetragonal precipitates in partially stabilized zirconia. It changes the microstructure for the subsequent dislocation mechanisms so that the models of precipitation hardening in these materials have to be revised.

At present, a challenging problem is the

understanding of the microprocesses of the plastic deformation of quasicrystals. According to the non-periodic structure of these materials, dislocations have to produce a special kind of structural disorder during their motion. Therefore, they have been considered immobile. *In situ* straining experiments at high temperatures gave the first direct evidence that, nevertheless, the dislocations carry the deformation also in quasicrystals [13]. Further details of the dislocation motion are being studied.

In conclusion, the described *in situ* experiments in the HVEM gave important insight into the deformation processes, frequently also by observing very different mechanisms in different temperature ranges.

References

1. Hoehl D. and Kästner G.: A 1600 K specimen heating top entry goniometer stage for a 1000 kV TEM. *Proc. 8th Europ. Cong. Electron Microscopy, Budapest*, Vol.1, pp. 469-470 (1984).
2. Fujita H. and Komatsu M.: *In situ* experiments of refractory materials at very-high temperature. *Proc. 7th Int. Conf. on High Voltage Electron Microscopy, Berkeley*, pp. 371-376 (1983).
3. Messerschmidt U. and Appel F.: Quantitative tensile-tilting stages for the high voltage electron microscope. *Ultramicroscopy*, **1**, 223-230 (1976).
4. Messerschmidt U. and Bartsch M.: High-temperature straining stage for *in situ* experiments in the high voltage electron microscope. *Ultramicroscopy*, **56**, 163-171 (1994).
5. Blümchen Th. and Messerschmidt U.: *In situ* oxidation cell for the high-voltage electron microscope. *Rev. Sci. Instrum.*,

66, 2837-2842 (1995).

6. Kästner G.: *Many-beam electron diffraction related to electron microscope diffraction contrast*, (Physical Research; Vol. 18) VCH Weinheim, Akad.-Verl., 1993.
7. Michler G.H.: Correlation between craze formation and mechanical behaviour of amorphous polymers. *J. Mater. Sci.*, **25**, 2321-234 (1990).
8. Kästner G. and Dietzsch Ch.: Liquid crystals investigated by HVEM. *Proc. 6th Int. Conf. High Voltage Electron Microscopy, Leiden*, Vol.4, pp. 400-403 (1980).
9. Hoehl D. and Bartsch H.: Results of *in situ* annealing of ion-implanted silicon in a high voltage electron microscope. *Phys. Status Solidi*, **A112**, 419-424 (1989).
10. Hesse D. and Heydenreich J.: Analysis of solid state reactions at film/substrate interfaces by electron microscopy. *Fres. J. Anal. Chem.*, **349**, 117-121 (1994).
11. Messerschmidt U., Appel F. and Schmid H.: The radius of curvature of dislocation segments in MgO crystals stressed in the high voltage electron microscope. *Philos. Mag.*, **51**, 781-796 (1985).
12. Baufeld B., Baither D., Messerschmidt U., Bartsch M., Foitzik A. and Ruhle M.: Ferroelasticity of t' zirconia: II, *In situ* straining in a high-voltage electron microscope. *J. Amer. Ceram. Soc.*, **80**, 1699-1705 (1997).
13. Wollgarten M., Bartsch M., Messerschmidt U., Feuerbacher M., Rosenfeld R., Beyss M. and Urban K.: *In situ* observation of dislocation motion in icosahedral AlPdMn single-quasicrystals. *Philos. Mag. Letters*, **71**, 99-105 (1995).

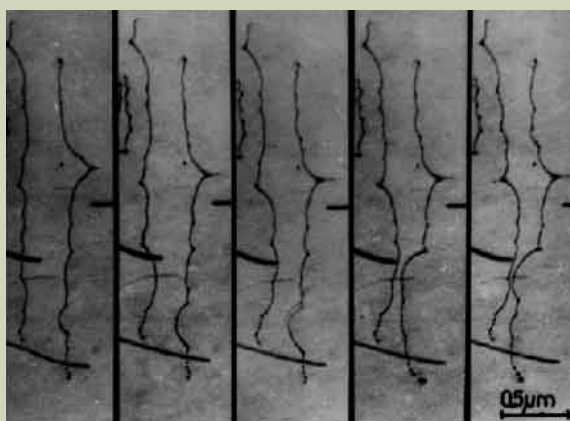


Fig.8. Moving dislocations in a magnesium oxide single crystal during deformation inside the HVEM at room temperature. The dislocations bow out between small precipitates where they form cusps. The dislocations move forward by overcoming the obstacles individually and assuming new equilibrium positions (U. Messerschmidt, F. Appel, 1976).

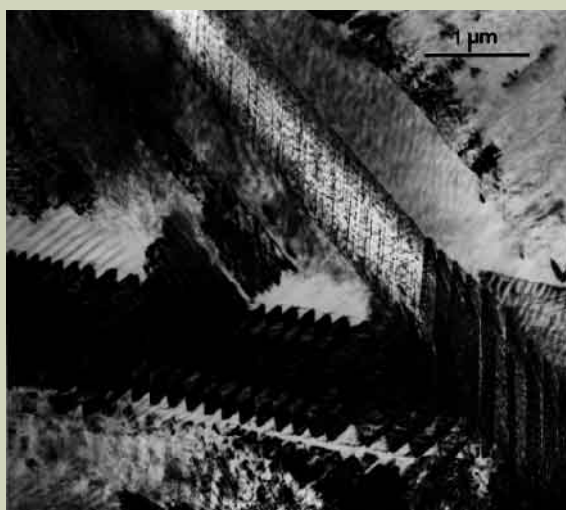


Fig.9. Ferroelastic deformation of t' zirconia during *in situ* straining in the HVEM at 1420 K. The dark structures are the untransformed tetragonal domains. Bright areas are transformed by ferroelastic deformation, which reduces the electron microscopy diffraction contrast (D. Baither, B. Baufeld, M. Bartsch, U. Messerschmidt, 1995).

Atomic Resolution Z-contrast Imaging of Interfaces and Defects



Edward M. James, Kiyosuke Kishida and Nigel D. Browning

Department of Physics, University of Illinois at Chicago

Z-contrast images of defects and interfaces in crystalline materials can be obtained at atomic resolution in the field emission transmission electron microscope (FEGTEM). Sophisticated simulation methods are not required to qualitatively interpret such images in terms of the position of atomic columns in the structure. Here we illustrate the power of this technique to image aperiodic structures in an ohmic metal contact to GaAs and a high temperature superconductor ($\text{Bi}_2\text{Sr}_2\text{Ca}_2\text{Cu}_3\text{O}_{10}$). A resolution of 0.15 nm is demonstrated with this incoherent imaging technique.

Introduction

The atomistic structure at interfaces and defects in crystalline materials can be investigated by transmission electron microscopy (TEM). For some time it has been possible to form phase contrast images with a resolution of 0.2 nm and better on instruments operating at practical accelerating voltages where beam-induced specimen damage is often not severe. However, the phase contrast image is hard to interpret without recourse to complex simulation and through focal series techniques [1]. In general, it is extremely difficult to invert the images to yield a model specimen structure. The effects of multiple scattering within the crystal and the phase problem (collection of image intensity, not complex amplitude) conspire to complicate analysis of the coherent phase contrast image [1, 2]. However, it has recently been shown that, using either a different illumination or detection geometry, images can be formed that are essentially incoherent and are generally much more easy to interpret; the location of atomic columns being identifiable from a raw image. In particular, a high angle annular dark-field (HAADF) detector in the scanning transmission electron microscope (STEM) has been used to acquire images at a resolution given by the size of the STEM elec-

tron probe intensity distribution [3]. This can be up to the order of 1.6 times smaller than the equivalent point resolution for STEM phase contrast images. The HAADF images additionally show a large degree of sensitivity to the average atomic number, Z , of atoms in the columns at each point in the image. For this reason the experimental technique is usually referred to a Z-contrast imaging (see, for example [4-7]).

Z-contrast imaging is therefore well suited to the analysis of defects and interfaces where we desire more complete understanding of their role in determining the bulk properties of materials. Also, the information that can be obtained from a Z-contrast image, using a probe of atomic spacing dimensions, can be used to position the electron beam accurately on a structural site of interest for immediate spectroscopy via energy-dispersed X-ray (EDS) or electron energy-loss (EELS) methods. In particular, with current instrumentation EELS can be performed at atomic resolution and with sufficient energy resolution to determine changes in electronic structure via fine structure analysis of core loss ionization edges in the spectrum [8].

In this paper we demonstrate the performance of STEM experiments with a sub-0.2 nm probe. Z-contrast images of high temperature superconducting $\text{Bi}_2\text{Sr}_2\text{Ca}_2\text{Cu}_3\text{O}_{10}$ (BSCCO) tapes were formed and used to investigate the changes of phase that can occur at grain boundaries. Additionally, an ohmic metal contact layer of Au on GaAs was

imaged at a resolution of around 0.15 nm. The changes in atomic structure were observed at different areas of morphological features at the interface.

Experimental technique

High resolution STEM conditions were set up in a JEOL JEM-2010F field emission electron microscope, equipped with an "ultra-high resolution" (URP) objective lens. **Figure 1** shows schematically the arrangement of the probe-forming optics. To form a small probe with adequate current there are four pre-conditions: a low coefficient of spherical aberration for the objective lens pre-field; selection of the correct probe convergence angle with an aperture (the STEM objective aperture); selection of a large demagnification of the electron source to minimize incoherent broadening of the probe; and the minimization of electrical and mechanical instabilities that also give incoherent probe broadening. In particular, excitation of the C1 condenser lens to near its maximum value was necessary to achieve sufficient demagnification of the electron source. Using a stationary probe, the coherent convergent beam diffraction pattern (CBED) could be observed. When obtained with a very high convergence angle (over 100 mrad), coherent interference effects between the CBED disks occur to high angle and the resulting pattern contains a wealth of information on the specimen and instrumental parameters (**Fig. 2**). It is often referred to as an electron Ronchigram, shadow image or micro-

845 W Taylor St., Chicago, IL, 60607-7059,
USA
E-mail: edjames@uic.edu

iffraction pattern [9]. Either observed directly on the microscope phosphor screen, or by a TV rate CCD camera, the Ronchigram proved invaluable in aligning the instrument, accurately determining the pertinent spherical aberration coefficient, correcting for astigmatism and assuring that a suitable level of source demagnification had been set. In addition, a well defocused Ronchigram forms a shadow image of the specimen and can be used for accurate specimen positioning and tilting, prior to insertion of a convergence-limiting STEM objective aperture. This use of the electron Ronchigram has been described elsewhere [10].

The microscope used for this study has a probe-forming spherical aberration coefficient of $0.57 \text{ mm} (\sim 0.05 \text{ mm})$. At the normal operational acceleration voltage of 200 kV, the smallest probe intensity distribution should be in the vicinity of the Scherzer focus condition [1]. If the incoherent probe-broadening effects are negligible, the probe intensity full-width at half-maximum (FWHM) will be approximately 0.13 nm, given the correct convergence angle of 12 mrad and an underfocus setting 40 nm from the Gaussian focus. Previous work has shown Z-contrast images from this instrument showing dumbbell contrast in bulk silicon oriented with the $\langle 110 \rangle$ zone axis parallel to the beam direction [10]. The $\{004\}$ spatial frequency ($[0.136 \text{ nm}^{-1}]$) was present in the images: if they are indeed incoherent, these images suggest a probe FWHM of around 0.14 nm. Observation of a 0.111 nm lattice fringe in both bright field STEM and the electron Ronchigram was further evidence that incoherent broadening of the probe does not dominate for these optical con-

ditions and that the Spherical aberration limited FWHM of 0.13 nm can be approached [10].

Once the optimum probe-forming conditions have been established it is trivial to obtain a variety of larger probe sizes (greater probe current) by reducing excitation of the condenser lenses. The resultant, larger image of the source then becomes the dominant factor in determining the probe size (incoherent broadening) and larger currents are available at the expense of sacrificing spatial resolution. In this way, it is possible to store a number of lens configurations in the microscope computer memory and dial up probe sizes ranging from 0.14 nm to many nanometers (given prior insertion of the correct STEM objective aperture to set the optimum convergence angle). Probe currents are of the order of 15 pA for a 0.2 nm probe FWHM and 1 nA for a 1.0 nm FWHM. Once present in the memory, it is possible to switch from CTEM operation to high resolution STEM very quickly and obtain the first atomic resolution Z-contrast images within minutes. This capability has been used for characterization of CdTe films grown directly on As passivated Si $\langle 001 \rangle$ [11] and is expected to be useful whenever it would be desirable to correlate information from a wide range of imaging and analytical techniques, all from the same specimen.

Imaging performance

The first specimen examined by Z-contrast STEM imaging was a textured $(\text{Bi,Pb})_2\text{Sr}_2\text{Ca}_2\text{Cu}_3\text{O}_{10}(\text{Bi-2223})/\text{Ag}$ composite tape. Such BSCCO tapes are of interest because of their potential as high- T_C materials for electric

power applications. It is known that grain boundaries in this material strongly affect the current transport properties [12] and there is a desire to be able to understand this in terms of the atomic structure of, or change in chemistry at any given defect type. **Figure 3 a** shows an atomic resolution Z-contrast image of bulk Bi-2223 and the individual atomic columns are seen in the $[110]$ crystal projection. Sensitivity of the high-angle scattering signal to the mean atomic number within each column results in the Bi columns appearing the brightest, followed by Sr, Cu and Ca. The inner semi-angle of the detector was approximately 50 mrad for this and all imaging experiments. On this instrument, this corresponds to setting approximately a 10 cm camera length with the intermediate and projector lenses. For such a high inner angle, the intensity approximates to the mean square of the atomic number Z, in each column; however, quantitative interpretation becomes unwise in the vicinity of a defect or interface where modifications to the column intensities can take place.

In **Fig. 3 b, 3 c** and **3 d** (001) twist boundaries are imaged using the 0.2 nm probe with the beam oriented parallel to the $[110]$, $[010]$ and $[101]$ directions (upper image area) respectively. From the images it is seen that the boundary is atomically flat and occurs in the middle of the double layer of BiO columns. No amorphous layers are observed at the twist boundaries but local phase variations are seen. In **Fig. 3 b** half a unit cell of Bi-2212 is present on either side of the boundary. **Fig. 3 c** shows one unit cell of the phase on one side of the boundary, in the lower image section. Local

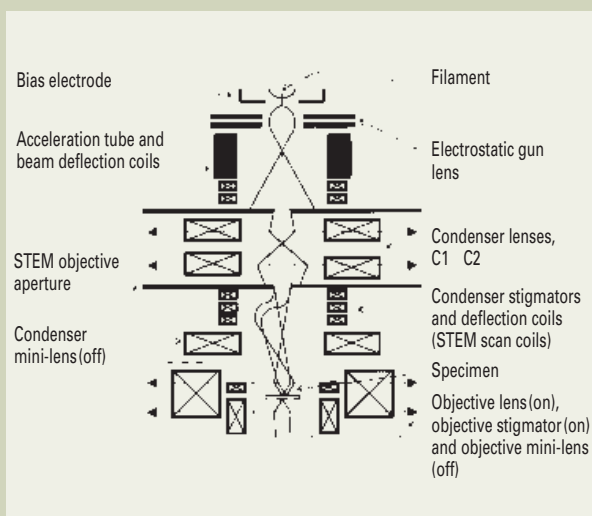


Fig.1. Schematic diagram showing the probe-forming electron optical arrangement of the JEOL JEM-2010F in STEM alignment. To form the optimum probe, C1 is run at high excitation, ensuring a large geometrical demagnification of the source. The objective lens pre-field forms the probe. Note: the CTEM condenser aperture is used as a STEM objective aperture.

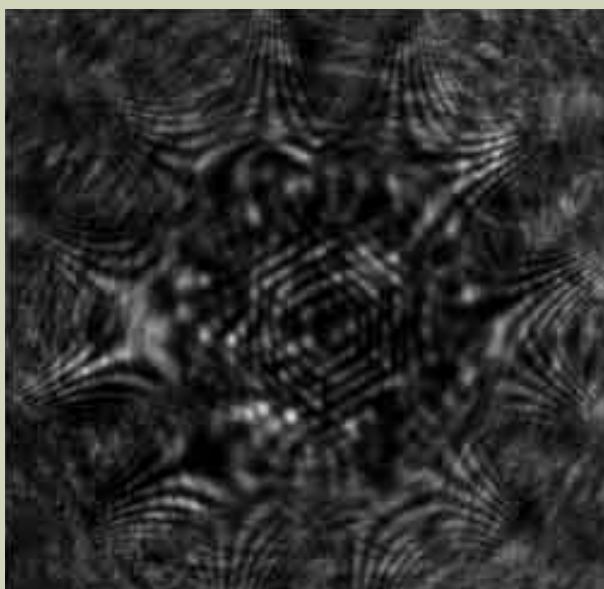


Fig.2. Electron Ronchigram of a thin silicon crystal in the $[111]$ projection. The probe is kept stationary, a large convergence angle selected and the pattern is observed on a post-specimen CCD camera. Lattice fringes are visible corresponding to 0.192 nm planar spacings. The distortions of the fringes out to high angle are due to spherical aberration of the objective lens pre-field.

superconducting properties may be affected by the presence of these layers of differing phase. Using the Z-contrast image they can be identified easily from the raw experimental image without simulation. In Fig. 3 d the twist boundary angle is 90° and the atomic column locations can be seen in both upper and lower parts of the image. Phase changes were also observed away from twist boundaries. This is shown in Fig. 4 with the crystal oriented with the [110] direction parallel to the beam. As before, the different phases can be readily identified and the positions of steps in the BiO planes located in the raw image. Correlating such features with the performance of given superconducting tapes is expected to help improve processing techniques and their commercial viability.

Z-contrast imaging was also used to investigate the atomistic arrangement at the interface of an ohmic contact of Au on n-type GaAs (001). This is an example of a contact with a relatively high specific contact resistance; hence it is generally not used commercially. It also exhibits other undesirable characteristics, including poor morphology and lack of stability at elevated temperatures. The sample investigated was grown by molecular beam epitaxy, followed by alloying at 690K for 15 s. In such a system, the formation of AuGa and subsequent sublimation of As occurs in a non-uniform manner along the interface [13]. These are cited as both the mechanism by which dopants can be correctly incorporated to yield ohmic behavior, and as the explanation of the poor morphology. In more complex metalization schemes used more often commercially for contacts to GaAs, the situation is more complicated and often not fully understood [14]. In combination with other microscopy techniques, the Z-contrast method may provide important new information because of its ease of interpretation and chemical sensitivity. One example would be the detection of an epitaxial layer between the semiconductor and metal that lowers the effective potential barrier height.

Figure 5 a shows the Z-contrast image of the relatively simple Au/GaAs ohmic contact. At this magnification atomic columns are not visible. As expected, spiking was prevalent in this sample and many protrusions of Au into GaAs were observed along the interface. One such protrusion is shown in Fig. 5 a. Different areas around the interface were then imaged at higher magnification to see the atomic structure. Figure 5 b shows a typical area away from a protrusion. The Au grains were seen to align with the plane approximately parallel to the interface, a configuration which results in a small lattice mismatch of about 2.5% with respect to GaAs (001). Without processing of the Z-contrast image it is possible to identify an atomic step in Fig. 5 b. Some reduction in the contrast of atomic columns is seen at the interface which may be due to preferential ion milling or to changes in morphology of the interface throughout the thickness of the sample in the direction parallel to the beam. The probe size used here was approximately 0.15 nm. Figures 5 c and 5 d show areas of the interface from different regions of the same Au protrusion into the GaAs. In Fig. 5 c the Au

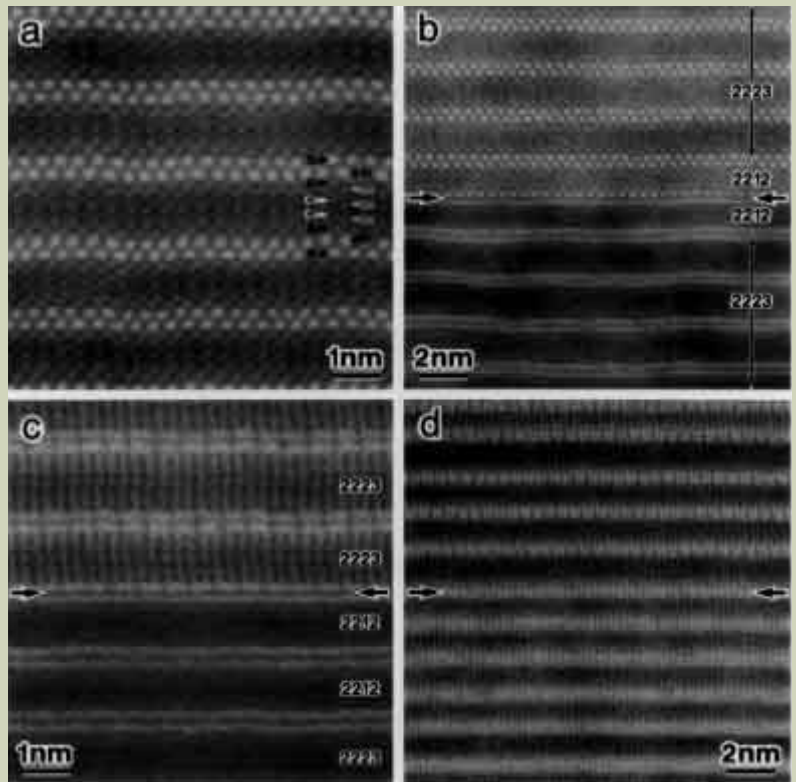


Fig.3. Z-contrast images of the BSCCO semiconductor: (a) the Bi-2223 phase in the [110] projection, (b, c) (001) twist boundaries at arbitrary misorientations and (d) a (001) twist boundary with a 90° twist angle. Positions of the grain boundaries are indicated by arrows.

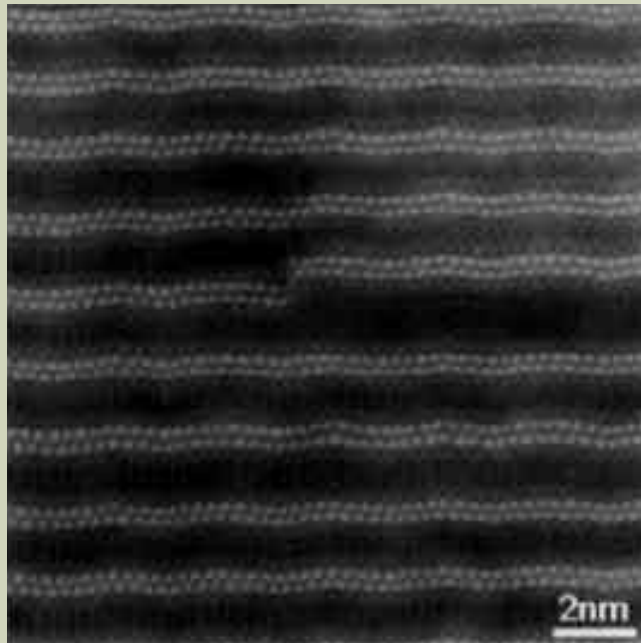


Fig.4. Z-contrast image of the BSCCO semiconductor in [110] projection. Departures from the Bi-2223 phase can be seen in the vicinity of the defect.

forms a (111) tilt boundary with GaAs (the angle is approximately 18°). A twin boundary is visible in the bulk Au. Dislocation cores can also be seen lying approximately every 0.5 nm along the interface. The electronic structure of the cores could, in principle, be understood by analysis of fine structure in a high spatial resolution EELS spectrum. They may play a significant part in the local Schottky barrier properties. Figure 5 d is from the underside of the spiking region. Here the Au interface is faceted along the close packed {111} planes with steps every one to two atomic columns. The regular occurrence of such protrusions along the interface mean that the overall electrical properties of the Au/GaAs ohmic contact are likely to depend on the individual characteristics of a wide range of interface types.

Conclusions

The use of the Z-contrast method to image defects and interfaces in crystalline specimens has been demonstrated. Such images are largely incoherent and can be qualitatively interpreted in terms of the atomic structure of the specimen: resolution of the images is given by

the probe size. The JEOL JEM-2010F with a URP pole-piece is capable of forming a STEM probe with a FWHM of 0.14 nm. Also, using the Z-contrast image as a map of the structure, the probe can be very accurately positioned for high spatial resolution EELS experiments.

Z-contrast STEM of BSCCO superconducting tapes has directly imaged twist boundaries located on the BiO double layers and local phase variations were often observed near the boundaries. Imaging of an ohmic metal contact (Au on GaAs) showed the atomistic structure of the atomically abrupt metal/semiconductor interface. Location of misfit dislocations, faceting at regions where spiking has occurred and the overall poor morphology of the interface are likely to be important factors determining its electrical properties.

Acknowledgements

The authors are grateful for the assistance of JEOL (USA) Inc.. The BSCCO samples were provided by M. Teplitsky of American Superconductor. The Au/GaAs sample was provided by J.L. Reno and A.G. Baca of Sandia National Laboratories. This research is

funded by NSF grants DMR-9601792, DMR-9803021 and DMR-9733895. KK acknowledges support from Research Fellowships of the Japan Society for the Promotion of Science for Young Scientists.

References

1. Reimer L.: *Transmission Electron Microscopy*, Springer Verlag, Berlin (1997).
2. Spence J. C. H.: *Experimental High Resolution Electron Microscopy 2nd Edition*, OUP, New York (1988).
3. Pennycook S. J., Jesson D. E., McGibbon A. J. and Nellist P. D.: High angle dark field STEM for advanced materials. *J. Electron Microsc.*, **45**, 36-43 (1997).
4. Hartel P., Rose H. and Dingel C.: Conditions and reasons for incoherent imaging in STEM, *Ultramicroscopy*, **63**, 93-114 (1996).
5. Jesson D. E. and Pennycook S. J.: Incoherent imaging of crystals using thermally scattered electrons. *Proc. R. Soc. (London) A*, **449**, 273-293 (1995).
6. Amali A. and Rez P.: Theory of lattice resolution in high angle annular dark-field images. *Microsc. Microanal.*, **3**, 28-46 (1997).
7. Hillyard S., Loane R. F. and Silcox J.: Annular dark-field imaging: resolution and thickness effects. *Ultramicroscopy*, **49**, 14-25 (1993).
8. Duscher, G., Browning, N. D. and Pennycook, S. J.: Atomic Column Resolved EELS. *Physica Status Solidi*, **166**, 327-342 (1998).
9. Cowley J. M.: Electron diffraction phenomena observed with a high resolution STEM instrument. *J. Elect. Microsc. Technique*, **3**, 25-44 (1986).
10. James E. M. and Browning N. D.: Practical aspects of atomic resolution imaging and analysis in STEM. *Ultramicroscopy* (in press, 1999).
11. Xin Y.: The effect of As Passivation on the MBE growth of high quality single domain CdTe(111)B on Si(111) substrates. submitted to *Appl. Phys. Lett.* (1999)
12. Umezawa A., Feng Y., Edelman H. S., Willis T. C., Parrell J. A., Larbaestier D. C., Riley G. N. and Carter W. L.: Further evidence that the critical-current density of (Bi,Pb)₂Sr₂Ca₂Cu₃O_x silver-sheathed tapes is controlled by residual layers of (Bi,Pb)₂Sr₂Ca₂Cu₃O_y at (001) twist boundaries. *Physica C*, **219**, 378-388 (1994)
13. Sands T.: Compound semiconductor metallurgy. *Mat. Sci. Eng. B*, **1**, 289-312 (1989).
14. Baca A. G., Ren F., Zolper J. C., Briggs R. D. and Pearton S. J.: A survey of ohmic contacts to III-V compound semiconductors. *Thin Solid Films*, **308-309**, 599-606 (1997).

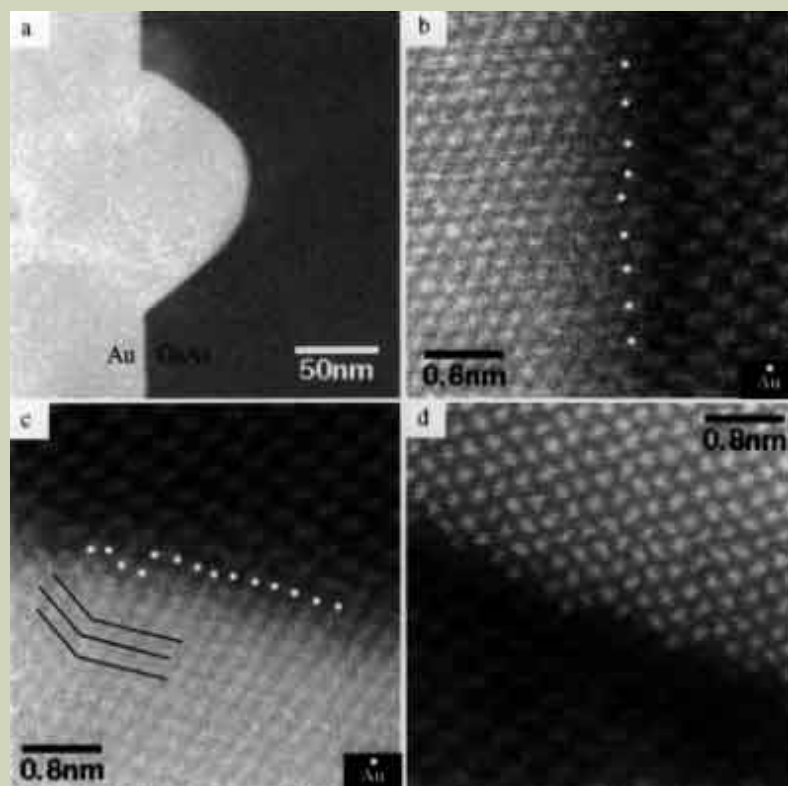
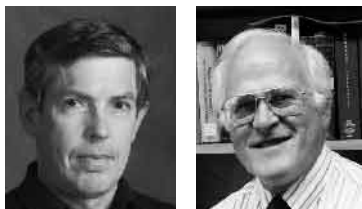


Fig.5. (a) Raw Z-contrast image at low magnification showing Au metal deposited on the GaAs substrate and the occurrence of spiking. (b) Raw Z-contrast image of the Au/GaAs interface at approx. 0.15 nm resolution (c) Raw atomic resolution Z-contrast image from the Au spike upper region. A (111) tilt boundary is formed with the GaAs with regularly spaced dislocation cores along the interface. (d) Raw Z-contrast image of the lower spike region. Here the Au interface is faceted along the close packed {111} planes.

The Growing Role of Electron Crystallography in Structural Biology



Kenneth H. Downing[†] and Robert M. Glaeser^{†,‡‡}

[†]Life Sciences Division, Lawrence Berkeley National Laboratory, University of California, Berkeley

^{‡‡}Department of Molecular and Cell Biology, University of California, Berkeley

The use of the electron microscope to determine the structure of complex biological macromolecules is now advancing at a rapid pace. When well-ordered, two-dimensional crystals are available, high resolution density maps can be obtained that are interpretable in atomic detail. The determination of the structure of tubulin provides a recent example of how electron crystallography has been used to solve a structure that could otherwise not be determined by x-ray crystallography or NMR spectroscopy. Even further advances in instrumentation and methodology are still to come, however, which promise the ability to merge data from thousands of images of individual, isolated molecules, in effect growing a virtual crystal in the computer, from which high resolution structures can be determined just as if the specimen had been a well-ordered, two-dimensional crystal.

Introduction

The use of electron microscopy in structural biology has recently begun to attract considerable attention. One key requirement for high-resolution studies is the use of frozen-hydrated specimens [1, 2] or equivalent methods [3] that preserve the native, hydrated state of biological macromolecules. The use of unstained biological materials, observed in a native-like environment, gives samples with the same degree of preservation enjoyed by those used for x-ray crystallography, and in this respect is much superior to the use of embedded, sectioned, and stained specimens, or negatively stained specimens.

Unstained, hydrated specimens are extremely sensitive to radiation damage, however, and data must be merged from many identical molecules in order to produce a statistically well-defined image without destroying the sample [4]. Merging data from identical molecules is most easily achieved if the molecules are in a thin, two-dimensional crystal. Thus it is not surprising that data-processing in high-resolution electron microscopy has much in common with the methods of x-ray crystallography, and that the field as a whole has come to be known as electron crystallography.

The application of high resolution electron

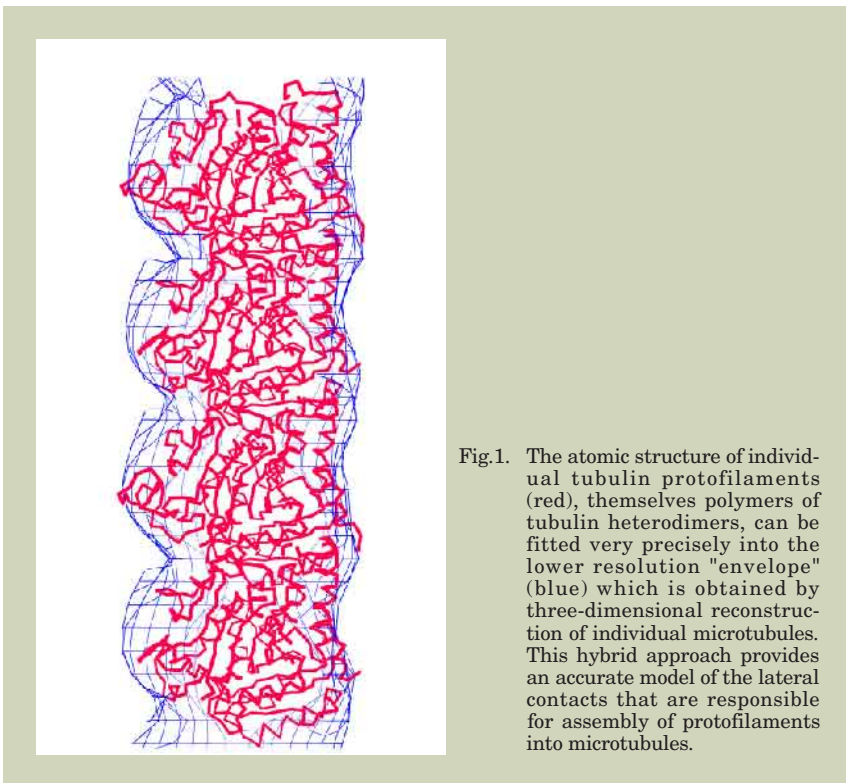


Fig.1. The atomic structure of individual tubulin protofilaments (red), themselves polymers of tubulin heterodimers, can be fitted very precisely into the lower resolution "envelope" (blue) which is obtained by three-dimensional reconstruction of individual microtubules. This hybrid approach provides an accurate model of the lateral contacts that are responsible for assembly of protofilaments into microtubules.

^{†,‡‡} CA 94720, USA

E-mail: khdowning@lbl.gov

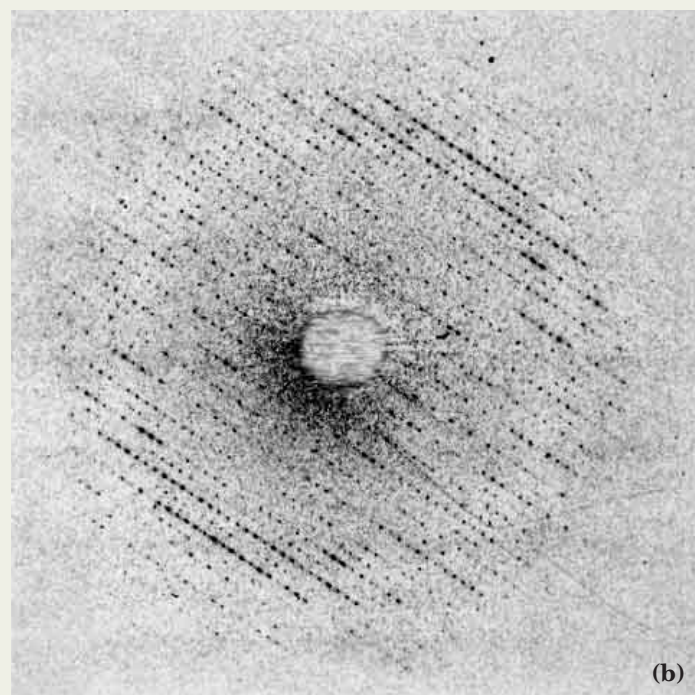
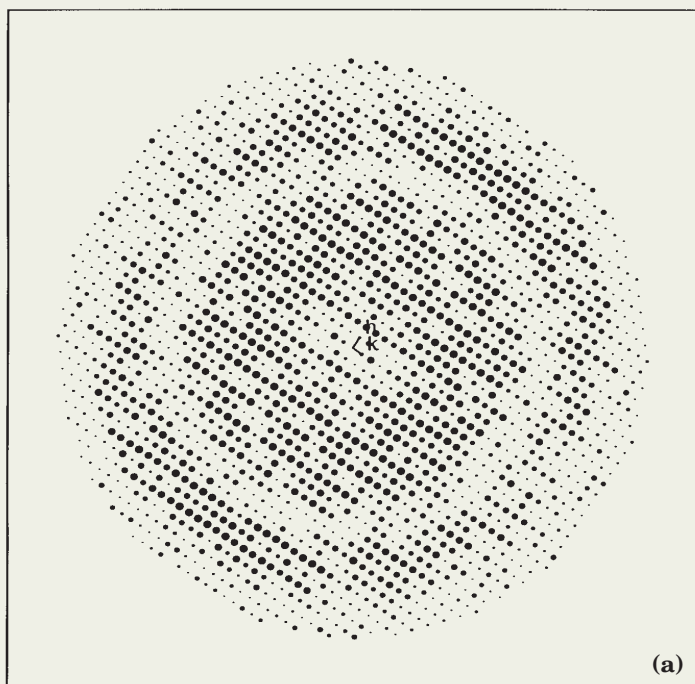


Fig.2. The computed Fourier transform of the low-dose image of a two-dimensional crystal resembles an electron diffraction pattern of the same type of specimen. (a) The computed Fourier transform is represented by spots whose size increases with increasingly large peak height relative to the background. (b) An actual electron diffraction pattern of a similar crystal is shown for comparison. In both cases the specimen was a two-dimensional crystal of tubulin, only one molecule thick.

microscopy is in no way limited to the use of thin (two-dimensional) crystals, however. Indeed, the birth of electron crystallography can be traced to a seminal paper on the helical tail of T4 bacteriophage [5]. Very exciting progress is currently being made with icosahedral viruses [6, 7], and even studies on the ribosome seem likely to soon break through the barrier of 1 nm-resolution [8]. What all such studies will always have in common with crystallography, however, is the requirement that data be merged from large numbers of identical molecules. Thus even the use of isolated molecules for high resolution electron microscopy can well be called "electron crystallography."

Some of the biologically most important applications of electron crystallography are, indeed, likely to be made with noncrystalline specimens. Large, multiprotein assemblies represent molecular machines that now are known to carry out some of the most sophisticated functions of the cell [9]. While these structures represent increasingly difficult challenges for x-ray crystallography, they are highly favorable specimens for single-particle electron cryo-microscopy (cryo-EM). When high resolution structures are known for some or all of the component protein molecules, those pieces can be fitted into cryo-EM density maps with remarkable precision, even at the relatively easily obtained resolution of only 2.5 nm. As an example, the atomic model of tubulin, itself determined by electron crystallography [10], has been used to obtain an atomic-resolution model of the fully assembled microtubule, shown in Fig. 1 [11]. Many similar examples of this form of hybrid crystallography could be cited. Among these, visualization of the way that myosin S1 ATPase attaches to actin filaments [12] stands as one of the best examples of how cryo-EM can advance our understanding of cell biology in ways that it is hard to imagine that x-ray crystallography alone could accomplish.

How Does Electron Crystallography Work?

The dream of seeing the structure of biological molecules at atomic resolution, just by looking at them with an electron microscope, is an impossible dream. This was already understood by interested physicists such as Dennis Gabor, as soon as the idea was first broached in 1928 [13]. Experiments showing the fading of electron diffraction patterns, together with an appreciation of the electron exposures that are needed to produce a statistically well-defined image, further drove the point home [4, 14].

Since it is only the statistical definition of the image that stands in the way of fulfilling this dream, however, and not the technical ability to focus electrons to atomic resolution, an alternative solution is easy to see. One need only record "invisible micrographs" [15] with safe exposure levels and then sum a sufficiently large number of images to generate the required signal-to-noise ratio.

When the sample is a two-dimensional crystal, the task of merging data from tens of thousands of noisy molecular images is a trivial one, because all of the molecules are already

aligned in precise translational and rotational register. In fact, all that is required is to compute the Fourier transform of the digitized low-dose image. The result looks like a diffraction pattern, **Fig. 2**, identical to that which would be recorded in a diffraction experiment, but better than a diffraction pattern because the crystallographic phases are also retained in the computed Fourier transform. When the sample is a helix (or fiber), an icosahedron or other particle with high point-group symmetry, and especially when it is a single asymmetric unit, the computational difficulty increases greatly. Nevertheless, even in the most challenging case of single particles, the process involved has become a routine one [16].

Continuing technological advances have been crucial to the success of electron crystallography in its current stage of development. Higher accelerating voltages, brighter electron

sources, and extremely stable cold stages represent some of the most important improvements in recent instrumentation [17]. Large-area CCD cameras have also proven their worth in recording electron diffraction patterns [18, 19], and further advances in direct electronic readout promise similar benefits for rapid image acquisition. Spot-scan imaging has decreased beam-induced specimen movement, thereby improving image quality and image yield [20, 21], while implementation of dynamic focusing with tilted specimens has simplified data processing and further improved contrast transfer from regions of the tilted specimen that would otherwise be highly out of focus [22]. Finally, unbending of lattice distortions has added powerfully to the improvement of high resolution signal in Fourier transforms of very large crystalline arrays [23].

The Power of Electron Crystallography in Structural Biology

The unique role that electron crystallography can play in solving structures of proteins that only crystallize as very thin, 2-D sheets is now widely appreciated. The initial application of electron crystallography to crystals of bacteriorhodopsin is described in detail by Fujiyoshi [17] in this issue of JEOL News. The second membrane protein whose structure was determined by electron crystallography was the photosynthetic light harvesting complex from chloroplast membranes [24]. Two-dimensional crystals of Taxol-stabilized tubulin represent another example of a structure that was highly sought after, but could not be solved by x-ray crystallography. As is illustrated in **Fig. 3**, the atomic-resolution structure shows the way in which Taxol, an important anti-cancer drug, binds to tubulin, and explains why the incorporation of tubulin heterodimers into protofilaments is needed in order to facilitate the hydrolysis of bound GTP. The structure thus explains (1) the molecular basis of dynamic instability of the assembled microtubule, so essential for remodeling of the tubulin network at different stages of the cell cycle, and (2) the way in which Taxol is able to halt the remodeling process, a step that is fatal to otherwise rapidly dividing cells.

The whole class of membrane proteins represents an area in which electron crystallography may have an increasingly important role. While many membrane proteins can be crystallized in a form suitable for x-ray diffraction studies, many other examples have so far been prepared only in forms that are suitable for electron crystallography. In some cases membrane proteins form 2-dimensional crystals, such as the water-channel protein in red blood cell membranes [25-27], gap junctions [28], rhodopsin [29] and the proton-pumping ATPase from neurospora [30]. In other cases, such as the nicotinic acetyl choline receptor [31] and the Ca-ATPase [32], the formation of tube-like membrane vesicles produces well-ordered helical arrays.

As remaining technological challenges, including specimen charging [33, 34], automation of data collection [35, 36], and teraflop-scale computation continue to be mastered, electron crystallography is likely to evolve in the direction of using ever smaller ordered arrays, and even single particles. The ability to use detergent-solubilized membrane proteins without reassembly into helices or two-dimensional arrays, as has been pioneered with the large Complex I from the mitochondrial electron transport chain [37], will provide access to one of the most difficult, remaining domains of structural biology. To fully achieve the potential of cryo-EM, remaining challenges in the perfection of image quality, the speed of direct image readout, and the mathematical tools of single-particle data processing must be mastered. Physics will allow atomic-resolution structures to be determined by merging data from single proteins, or single domains of proteins, as small as 20,000 dalton [38]. If this goal is realized, even if only for larger proteins or domains 4 or 5 times that size, structural

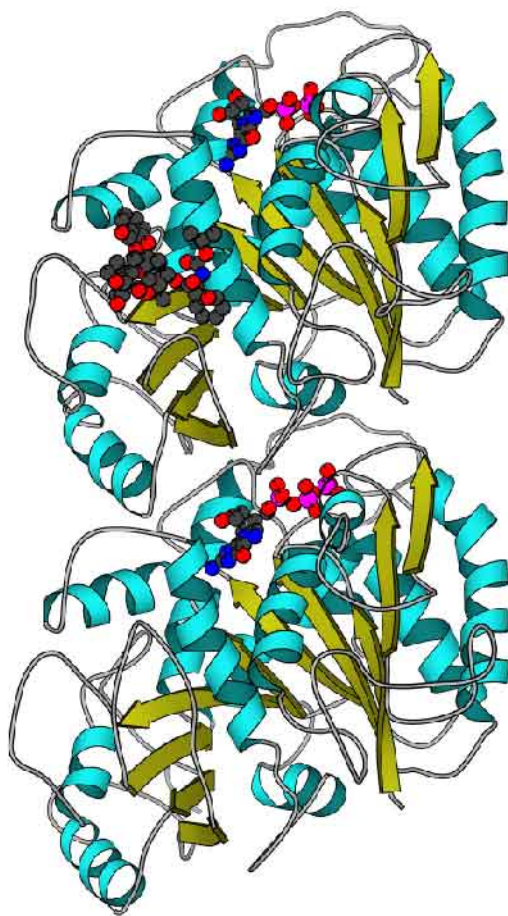


Fig.3. The atomic model of tubulin that was obtained from two-dimensional crystals is represented as a ribbon diagram in order to facilitate the recognition of regions of alpha helix and beta sheet. Explicit atomic models are used to represent a GTP molecule at the interface of the α -tubulin and β -tubulin monomers, where residues needed to form a catalytic site must be contributed by the interaction of the two subunits. The anti-cancer drug, Taxol, is also shown as an explicit atomic structure, bound at the lateral interface between individual tubulin protofilaments.

biology will never again be the same.

Acknowledgement

We are grateful to the colleagues with whom we have had enjoyable discussions on many of the topics reviewed here, and especially to Dr. Eva Nogales, who has participated in the published work on tubulin which we have used to illustrate key points. This work has been supported by NIH grants GM 51487 and GM 46033.

References

1. Taylor K. A. and Glaeser R. M.: Electron diffraction of frozen, hydrated protein crystals. *Science*, **186**, 1036-1037 (1974).
2. Dubochet J., Adrian M., Chang J. J., Homo J. -C., Lepault J., McDowell A. W. and Schultz P.: Cryo-electron microscopy of vitrified specimens. *Quart. Rev. Biophys.*, **21**, 129-228 (1988).
3. Unwin P. N. T. and Henderson R.: Molecular structure determination by electron microscopy of unstained crystalline specimens. *J. Mol. Biol.*, **94**, 425-440 (1975).
4. Glaeser R. M.: Limitations to significant information in biological electron microscopy as a result of radiation damage. *J. Ultrastruct. Res.*, **36**, 466-482 (1971).
5. DeRosier D. and Klug A.: Reconstruction of 3-dimensional structures from electron micrographs. *Nature*, **217**, 130-134 (1968).
6. Boettcher B., Wynne S. A. and Crowther R. A.: Determination of the fold of a core protein of hepatitis B virus by electron cryomicroscopy. *Nature*, **386**, 88-91 (1997).
7. Conway J. F., Cheng N., Zlotnick A., Wingfield P. T., Stahl S. J. and Steven A. C.: Visualization of a 4-helix bundle in the hepatitis B virus capsid by cryo-electron microscopy. *Nature*, **386**, 91-94 (1997).
8. Malhotra A., Penczek P., Agrawal R. K., Cabashvili I. S., Grassucci R. A., Junemann R., Burkhardt N., Nierhaus K. H. and Frank J.: *Escherichia coli* 70S ribosome at 15Å resolution by cryo-electron microscopy: localization of fmet-tRNA^{fMet} and fitting of L1 protein. *J. Mol. Biol.*, **280**, 103-116 (1998).
9. Alberts B.: The cell as a collection of protein machines: preparing the next generation of molecular biologists. *Cell*, **92**, 291-294 (1998).
10. Nogales E., Wolf S. G. and Downing K. H.: Structure of the tubulin dimer by electron crystallography. *Nature*, **391**, 199-203 (1998).
11. Nogales E., Whittaker M., Milligan R. A. and Downing K. H.: High resolution model of the microtubule. *Cell*, **96**, 79-88 (1999).
12. Rayment I., Holden H., Whittaker M., Yohn C., Lorenz M., Holmes K. and Milligan R.: Structure of the actin-myosin complex and its implications for muscle contraction. *Science*, **261**, 58-65 (1993).
13. Gabor D.: Preface to: Marton L. "Early History of the Electron Microscope.", San Francisco Press, San Francisco (1968).
14. Kobayashi K. and Sakaoku K.: Irradiation changes in organic polymers at various accelerating voltages. *Lab. Invest.*, **14**, 1097-1114 (1965).
15. Caspar D. L.: Distinct images from invisible micrographs. *Nature*, **257**, 9-10 (1975).
16. Frank J.: *Three-dimensional Electron Microscopy of Macromolecular Assemblies*. Academic Press (1996).
17. Fujiyoshi Y.: Observation of protein structures through an electron beam. *JEOL News*, **34E**, 29-34 (1999).
18. Downing K. H. and Hendrickson F.: Performance of a 2k CCD camera designed for electron crystallography. *Ultramicroscopy*, **75**, 215-233 (1999).
19. Faruqi A. R., Henderson R. and Subramaniam S.: Cooled CCD detector with tapered fibre optics for recording electron diffraction patterns. *Ultramicroscopy*, **75**, 235-250 (1999).
20. Downing K. H. and Glaeser R. M.: Improvement in high resolution image quality of radiation-sensitive specimens achieved with reduced spot size of the electron beam. *Ultramicroscopy*, **20**, 269-278 (1986).
21. Bullough P. and Henderson R.: Use of spot-scan procedure for recording low-dose micrographs of beam-sensitive specimens. *Ultramicroscopy*, **21**, 223-230 (1987).
22. Downing K. H.: Automatic focus correction for spot-scan imaging of tilted specimens. *Ultramicroscopy*, **46**, 199-206 (1992).
23. Henderson R., Baldwin J. M., Downing K. H., Lepault J. and Zemlin F.: Structure of purple membrane from *Halobacterium halobium*: recording, measurement and evaluation of electron micrographs at 3.5Å resolution. *Ultramicroscopy*, **19**, 147-178 (1986).
24. Kühlbrandt W., Wang D. N. and Fujiyoshi Y.: Atomic model of plant light-harvesting complex by electron crystallography. *Nature*, **367**, 614-621 (1994).
25. Li H., Lee S. and Jap B. K.: Molecular design of aquaporin-1 water channel as revealed by electron crystallography. *Nature Struct. Biol.*, **4**, 263-265 (1997).
26. Cheng A., van Hoek A. N., Yeager M., Verkman A. S. and Mitra A.: Three-dimensional organization of a human water channel. *Nature*, **387**, 627-630 (1997).
27. Walz T., Hirai T., Murata K., Heymann J. B., Mitsuoka K., Fujiyoshi Y., Smith B. L., Agre P. and Engel A.: The three-dimensional structure of aquaporin-1. *Nature*, **387**, 624-627 (1997).
28. Unger V. M., Kumar N. M., Gilula N. B. and Yeager M.: Three-dimensional structure of a recombinant gap junction membrane channel. *Science*, **283**, 1176-1180 (1999).
29. Krebs A., Villa C., Edwards P. C. and Schertler G. F.: Characterization of an improved two-dimensional p22121 crystal from bovine rhodopsin. *J. Mol. Biol.*, **282**, 991-1003 (1998).
30. Auer M., Scarborough G. A. and Kühlbrandt W.: Three-dimensional map of the plasma membrane H⁺-ATPase in the open conformation. *Nature*, **392**, 840-843 (1998).
31. Unwin N.: The nicotinic acetylcholine receptor of the Torpedo electric ray. *J. Struct. Biol.*, **121**, 181-190 (1998).
32. Zhang P., Toyoshima C., Yonekura K., Green N. M. and Stokes D. L.: Structure of the calcium pump from sarcoplasmic reticulum at 8Å resolution. *Nature*, **392**, 835-839 (1998).
33. Brink J., Gross H., Tittmann P., Sherman M. B. and Chiu W.: Reduction of charging in protein electron cryomicroscopy. *J. Microscopy*, **191**, 67-73 (1998).
34. Brink J., Sherman M. B., Berriman J. and Chiu W.: Evaluation of charging on macromolecules in electron cryomicroscopy. *Ultramicroscopy*, **72**, 41-52 (1998).
35. Ermantraut E., Wohlfart K. and Tichelaar W.: Perforated support foils with pre-determined hole size, shape and arrangement. *Ultramicroscopy*, **74**, 75-81 (1998).
36. Oostergetel G. T., Keegstra W. and Brisson A.: Automation of specimen selection and data acquisition for protein electron crystallography. *Ultramicroscopy*, **74**, 47-59 (1998).
37. Grigorieff N.: Three-dimensional structure of bovine NADH:ubiquinone oxidoreductase (complex I) at 22Å in ice. *J. Mol. Biol.*, **277**, 1033-1046 (1998).
38. Glaeser R. M.: Electron crystallography: present excitement, a nod to the past, anticipating the future. *J. Struct. Biol.*, (in press).

Factors Promoting Research and Development in Electron Microscopy in Japan*



Hiroshi Hirano

**President, Chairman of the Board of Directors, Japanese Society of Electron Microscopy
Professor of Anatomy, †Kyorin University School of Medicine**

The electron microscope is needless to say a fundamental and indispensable instrument to investigate and examine microstructures both in life and materials sciences and technologies, and is widely distributed to nearly all the research laboratories and factories concerned. In electron optics, Japan, in spite of its delay in getting started, has attained a worldwide success in becoming a leader and maintaining the leadership in the manufacturing and supplying of the instruments, and also in contributing to theoretics, basic research, and applications [1-4]. Japan has also developed a large population of researchers in this field as well [1].

Cradle Period

In the early 1930's, several papers on the transmission electron microscope (TEM) were reported by E. Ruska and M. Knoll [5], B. von Borries [6], and others; however, only a few Japanese scientists and engineers were interested in these papers. Micrographs taken by B. von Borries and E. Ruska [7] using their first Siemens TEM (1938) with an estimated resolving power of 100 Å [8] attracted the attention of Japanese scientists and engineers and stimulated them to start their enthusiastic studies on electron microscopy [1].

*This article was originally contributed as an invited lecture to the 1st Conference on Research and Practical Realization in Hungary held on May 23-25, 1991, in Debrecen, Hungary, then partly revised and supplemented on the occasion of the 50th anniversary of JEOL Ltd.

**JSPS was originally set up in 1932 with an Imperial Grant as a private foundation, and in 1967 it was reorganized to become a special juridical person under the auspices of the Ministry of Education, Science, Sports and Culture of Japan. Since its original establishment as a nonprofit foundation, JSPS has worked to promote scientific cooperation between industry and academia by creating university-industry cooperation research committees, where researchers from the two sectors can meet to discuss specific technical subjects. The operating expenses of these committees, comprising mostly travel and meeting costs, are covered by membership fees collected from the private companies participating in them. Over the years, 168 such committees have been organized. Many have completed their work, and thus been dissolved. There are currently 52 active committees [9].

In 1939, the 37th subcommittee affiliated with the Japan Society for the Promotion of Science (JSPS)** was established for interdisciplinary research on electron microscopy, and researchers concerned with it gathered from universities and industries as well [1,3,4]. Although in the same year World War II broke out and various difficulties arose, the subcommittee activities were continued without any interruption until 1947, i.e., two years after the end of the war. By then, the electron microscopes that had been constructed at three universities, one national laboratory, and four manufacturing companies including Hitachi Ltd., Tokyo Shibaura Electric Co., Ltd., (Toshiba Corporation), and Shimadzu Seisakusho Co., Ltd. attained a resolution of about 3 nm [1-4]. The subcommittee, chaired by S. Seto, a Tokyo University Professor, did not intend to import any microscope from overseas at all. Instead, they concentrated their efforts on the development of an electron microscope completely based on the Japanese domestic activities [1, 4]. Each member's laboratory was opened to all the other members, where the meetings were held, and the results were presented and discussed. Furthermore, the chairman always rejected pressures from outsiders, particularly from the military forces, who were at that time so powerful and who stressed the superemence of intensifying war-potentials [1]. In fact, the subcommittee gave birth to electron microscopy in Japan; its contribution was very large [1, 3, 4].

In 1945, Japan was defeated; it was completely destroyed, crushed, and occupied by the Allied Forces. The electron microscopes that had survived, i.e., had not been damaged in the war or had not been evacuated to the countryside, numbered

only four [1]. The entire society was extremely impoverished. Many Japanese scientists and engineers, who had been cast into difficulties, disturbances, and hunger in the devastated land, however, chose to pursue ways to make maximal use of their knowledge of and experience in science and engineering in order to recover Japan from its dire situation. Toward this goal, another group sought to contribute to the developmental research of the electron microscope and its applications [1, 10].

Spectacular Rise

Soon after the end of the war, newcomers joined the race to manufacture electron microscopes. That is, Japan Electron Optics Laboratory Co., Ltd. (JEOL Ltd.), established by a group of demobilized naval technical officers, completed its first model in 1949 [10], while Akashi Seisakusho, Ltd. (Topcon Corporation) produced its first microscope in 1953 with the close collaboration of a researcher from a national institution, the Electrotechnical Laboratory, one of the pioneers affiliated with the 37th subcommittee [1]. During the past decades, JEOL, Hitachi and Akashi (Topcon) among the Japanese makers, have grown rapidly, and have won a large share of the worldwide market for the electron microscope.

In general, Japanese manufacturing companies, investing with a vision, do their best to develop and offer products that are of high quality, easy to operate, and at an affordable price [11]. They are always facing severe competition for the market share. This is true in the electron microscope industry also. In addition, particularly until the 1970's, electron microscopy was one of the major topics of the Ministry of Education, Science,

Instrument	Researcher	Manufacturer
Ultrahigh vacuum TEM	K. Takayanagi (Tokyo Inst. Technol.) [12]	JEOL
Ultrahigh vacuum SEM	S. Ino (Tokyo Univ.) [13]	JEOL
High resolution cryo-EM	Y. Fujiyoshi (Kyoto Univ.) [14]	JEOL
Ultrahigh resolution TEM	M. Tanaka (Tohoku Univ.) [15]	JEOL
Ultrahigh resolution SEM	K. Tanaka (Tottori Univ.) [16]	Hitachi
STM-TEM	K. Takayanagi (Tokyo Inst. Technol.) [17]	JEOL
400-kV analytical TEM	H. Hashimoto (Osaka Univ.) [18]	JEOL
Light-electron microscope (LEM-2000)	Clin Pathol [1]	Akashi (Topcon)

Table.1. Cooperative Joint Developmental Research of EM in the 1980's to 90's.

†Mitaka, Tokyo 181-8611, Japan

Sports and Culture of Japan, which awarded a significant number of grants to many university and institutional laboratories doing research on electron microscopy.

In Japan, the electron microscope manufacturers themselves have been eager to communicate with the researchers using their instruments. For instance, they are willing to send their employees to academic meetings and events held by the Japanese Society of Electron Microscopy, which was established in 1949, and to contribute financial supplies as well as scientific papers to the Society. Normally they allow domestic researchers, and sometimes even users from overseas, to try out the latest models of their equipment kept in their factories. In this way, at the same time, they have acquired much information on the performance, structure, and maintenance of the electron microscope, and also have succeeded in increasing the number of their customers and the demand for electron microscopy [1, 10].

During the cradle period, both the universities and industry in Japan were standing in the same line in terms of the research and development in electron microscopy. Since then, the manufacturers have gradually accumulated experience that surpasses that of the universities and institutions, while the latter have tended to concentrate on basic and/or application research [1].

Recent Progress

Contrary to those in Europe and the United States, universities and institutions in Japan usually lack the workshop and/or the storehouse system where instruments and facilities are to be constructed and assembled for laboratory use. When Japanese researchers are not satisfied with the conventional or standard model for their own use, they may consult with the manufacturer. This is a case where the "software" side proposes and stimulates the innovation of the "hardware" side. If the interests and policies of both sides coincide, the makers may supply what the researchers wish to have. Nowadays Japanese manufacturers are much superior to ordinary university workshops in terms of supplying new or improved instruments and facilities for laboratory use. For the future development of the electron microscope, special grants may sometimes come from the Ministry of Education, Science, Sports and Culture of Japan. As a rule, the amount of grants offered by the government is less than half of that necessary, and the rest is supplied by manufacturers. The makers themselves gain their benefit in the accumulation of further experience in research and development. Several examples achieved in the 1980's to 90's are shown in the table above.

In addition to the above, the imaging plate for TEM recording [19], high-voltage atomic resolution microscope [20], field emission ultrahigh-resolution analytical electron microscope [21], omega mode imaging energy filters at 200 kV [22], etc., have been developed by JEOL in close collaboration with university researchers both in Japan and overseas.

Turning-Point

In Japan, the ratio of research expenses to GDP has been increasing year by year. However, the amount of increase over that of the previous year is extremely different among different fields. Nowadays, the amount of research expenses for industry is around three times that for universities [23]. Big industries usually possess their own laboratories and institutions for their own research and development. At present, it seems to be inevitable that university researchers will play a less important role than before in developing new instruments. In parallel, changes are taking place in the

electron microscope market. Universities used to be good customers, but recently many electron microscopes have been purchased by industry. A large number of scanning electron microscopes (SEM), in particular, have been installed and put into the in-line system in semiconductor manufacturing factories, almost as if they were a sort of household electric appliance [24]. As well as a research instrument in the laboratory, the conventional electron microscope itself has become an ordinary type of equipment commonly used and widely distributed in a variety of fields.

Besides conventional electron microscopes, different types of "new microscopes" have been recently introduced and extensively used in life and materials sciences and technologies. Particularly in the field of life science, confocal laser scanning microscopy, for instance, has proved a useful tool for three-dimensional imaging [25]. Scanning probe microscopes are also searching their own ways in biological specimens [26]. At present, joint use of these machines, conventional and newly-developed, is fairly common. It should be stressed here, however, that conventional electron microscopy is still indispensable and powerful, and plays an important and key role to clarify detailed and precise microstructures and topography. At the same time, progress in direct digitization is an unavoidable and urgent task in TEM image recording as well, to facilitate computed analysis. Since many years ago, new models have been expected to be available for common use which afford four-dimensional imaging with high resolution and easy operation.

Looking back briefly to the history of electron microscopy in Japan, it is fairly difficult to find many breakthroughs in the development and innovation of the electron microscope. However, Japanese researchers and engineers are very adept at making single and squeeze plays instead of trying to hit home runs [11]. Minor discoveries and innovations, even though each of them might seem trifling and negligible, do accumulate and, when well organized, can exert a big power in the hands of excellent management with free competition. This is true both in universities and in industry. Based on records and documents, the developmental research and realization in electron microscopy in Japan are regarded to be a good example of epoch-making cooperative achievement among the university, industry, and government.

Lastly, I would like to mention that this year coincidentally marks the 50th anniversary of the Japanese Society of Electron Microscopy and of JEOL Ltd. as well. I hereby very much look forward to the limitless growth of both in the future.

References

- Fujita H. (Editor in Chief): *History of Electron Microscopes --- In Commemoration of the 11th Int. Congr. on Electron Microscopy.*, Kyoto, 1986, Business Center for Academic Societies Japan, Tokyo (1986).
- Sugata E. (Editor in Chief): *Electron Microscopes of Japan 1936-1965 --- A Historical Survey*, Maruzen, Tokyo (1968).
- Kanaya K.: Reminiscences of the development of electron optics and electron microscope instrumentation in Japan. In: *The Beginnings of Electron Microscopy --- Advances in Electronic and Electron Physics*, Suppl. 16, [Hawkes P. W. (ed.)], Academic Press, pp. 317-386 (1985).
- Asakura K. and Adachi K.: *Pioneers in Electron Microscopy in Japan* (In Japanese). Medical Publication Center, Inc., Tokyo (1989).
- Ruska E. and Knoll M.: Die magnetische Sammelspule für schnelle Elektronenstrahlen. *Z. Techn. Phys.*, **12**, 389-399 (1931).
- von Borries B. und Ruska E.: Die Abbildung durch-

- strahler Folien im Elektronenmikroskop. *Z. Phys.*, **83**, 187-193 (1933).
- von Borries B. und Ruska E.: Ein Übermikroskop für Forschungsinstitute. *Naturwiss.*, **27**, 575-582 (1939).
- von Borries B. und Ruska E.: *Wiss. Veroff. aus Siemens*, **17**, 99 (1938).
- von Borries B., Ruska E. und Ruska H.: *ibid.* **17**, 107 (1938). Cited from Ref.#1.
- Japan Society for the Promotion of Science (GAKUSHIN)*, Japan Society for the Promotion of Science, Tokyo, pp. 1-35 (1999).
- JEOL history book commemorating its 35th year* (In Japanese), JEOL Ltd., Tokyo (1986).
- Karatsu H.: Global leadership in semiconductors. *Nature*, **346**, 101-102 (1990).
- Takayanagi K., Tanishiro Y., Kobayashi K., Akiyama K. and Yagi K.: Surface structures observed by high-resolution UHV electron microscopy at atomic level. *Jpn. J. Appl. Phys.*, **26**, L957-L960 (1987).
- Kondo Y., Ohi K., Ishibashi Y., Hirano H., Harada Y., Takayanagi K., Tanishiro Y., Kobayashi K. and Yagi K.: Design and development of an ultrahigh vacuum high-resolution transmission electron microscope. *Ultramicroscopy*, **35**, 111-118 (1991).
- Harada Y., Tomita T., Kokubo Y., Daimon H. and Ino S.: Development of an ultrahigh vacuum high resolution scanning transmission electron microscope. *J. Electron Microscopy*, **42**, 294-304 (1993).
- Yamagishi H., Fujiyoshi Y., Aoki Y. and Harada Y.: High Resolution Cryo-Electron Microscope. *Electron Microscopy* (In Japanese), **22**, 153-162 (1988).
- Tsuno K., Ohya J., Kato M., Kimura J., Kai M., Nakanishi K., Terauchi T. and Tanaka M.: A Wien filter electron energy loss spectrometer for transmission electron microscopy. *Proc. 12th Int. Congr. Electron Microscopy. Seattle Vol. 2*, San Francisco Press, San Francisco, pp. 32-33 (1990).
- Tanaka K.: High-resolution scanning electron microscopy in biology. *Proc. 12th Int. Congr. Electron Microscopy. Seattle Vol. 3*, San Francisco Press, San Francisco, pp. 14-15 (1990).
- Ohnishi H., Kondo Y. and Takayanagi K.: Quantized conductance through individual rows of suspended gold atoms. *Nature*, **395**, 780-783 (1998).
- Hashimoto H., Endoh H., Tomita M., Ajika N., Kuwabara M., Hata Y., Tsubokawa Y., Honda T., Harada Y., Sakurai S., Etoh T. and Yokota Y.: Construction and application of a 400kV analytical atom resolution electron microscope. *J. Electron Microscopy Technique*, **3**, 5-24 (1986).
- Mori N., Oikawa T., Katoh T., Miyahara J. and Harada Y.: Application of the "imaging plate" to TEM image recording. *Ultramicroscopy*, **25**, 195-202 (1988).
- Phillipp F., Höschen R., Osaki M., Möbus G. and Rühle M.: New high-voltage atomic resolution microscope approaching 1 Å point resolution installed in Stuttgart. *Ultramicroscopy*, **56**, 1-10 (1994).
- Honda T., Tomita T., Kaneyama T. and Ishida Y.: Field emission ultrahigh-resolution analytical electron microscope. *Ultramicroscopy*, **54**, 132-144 (1994).
- Tsuno K., Kaneyama T., Honda T., Tsuda K., Terauchi M. and Tanaka M.: Design and testing of Omega mode imaging energy filters at 200 kV. *J. Electron Microscopy*, **46**, 357-368 (1997).
- Tsuno K., Kaneyama T., Honda T. and Ishida Y.: Non-isochromaticity of an omega filter in a 200 kV transmission electron microscope. *J. Electron Microscopy*, **47**, 611-619 (1998).
- Statistics Bureau, Management and Coordination Agency, Japan: *Report on the Survey of Research and Development* (1998) (In Japanese), Tokyo, pp. 536-537 (1998).
- JEOL Overseas and Domestic Sales Divisions: Personal communication.
- Handbook of Biological Confocal Microscopy. 2nd edition.* [Pawley J. B. (ed.)], Plenum Press, New York (1995).
- Ushiki T.: Biological applications of SPM. *Electron Microscopy* (In Japanese), **34** (Suppl. 1), 32 (1999).

The Development and Assessment of a High Performance Field-Emission-Gun Analytical HREM for Materials Science Applications



John L. Hutchison[†], Ron C. Doole[†], Rafal E. Dunin-Borkowski[†], Jeremy Sloan^{††} and Malcolm L. H. Green^{††}

[†]Department of Materials, University of Oxford

^{††}Inorganic Chemistry Laboratory, University of Oxford

A new 300 kilovolt field-emission-gun analytical electron microscope has recently been installed in the Department of Materials at Oxford University. In this communication we first outline the materials developments for which we required a very high performance in all operating modes of the microscope. We then present the main features of this instrument, a JEM-3000F equipped with comprehensive analytical facilities, which is the first to be constructed in this particular configuration. Finally we show preliminary experimental results which confirm its performance, and also give examples of its applications to some novel nanostructured materials.

Development of novel nanostructured materials

An important area of materials research at Oxford concerns the fabrication and characterisation of advanced materials based on nanostructures. Our nanostructure development programme includes fullerenes and carbon nanotubes, novel nanocomposites, optoelectronic materials and information storage media. In order to understand and control the fabrication of these materials, it is essential that they be characterised at very close to the atomic scale. For this it became evident that our existing HREM facilities, based on JEM-4000EX(II) and JEM-2010 instruments, while routinely capable of atomic scale spatial imaging, could not provide a sufficiently high-current, sub-nanometre sized probe for both the high spatial resolution *and* chemical characterisation which was also required. The development of the new generation of high-resolution field-emission-gun (FEG) HREM instruments has provided such a tool, and when funding was made available for this project by the U.K.'s

Engineering and Physical Sciences Research Council, we started working with JEOL (UK) and JEOL Ltd. to achieve an optimum instrument for our particular needs.

Performance criteria for the success of this project

In setting up this Advanced Microanalytical HREM Facility, it was necessary to take account of a number of factors which ultimately affected our choice of instrument. These included the following:

1. Good spatial resolution, better than 0.2 nm. This is essential for structure imaging of metallic particles.
2. Good specimen tilt capability, at least 20°, with the possibility of accommodating heating or cooling, double-tilt specimen holders.
3. A small probe capability, with a round probe smaller than 0.5 nm in diameter, with high beam current.
4. A high sensitivity EDX system, with good capability for light element analysis, and very low background X-ray counts.
5. A high performance digital image acquisition and analysis system.
6. PEELS analysis and energy filtered imaging.
7. As this would be a multi-user facility, ease

of use and reliability were both additional, but important factors to consider.

The instrument

The installation is based around the JEM-3000F instrument, a 300 kilovolt microscope equipped with a thermally assisted, Schottky emitter type field emission electron source. The instrument is in the ultra-high resolution configuration, with a low-aberration objective lens. The additional analytical facilities are: an Oxford Instruments ISIS 300™ EDX system with an ultra-thin-window Si(Li) detector, a Gatan (1k 1k) CCD camera, and a Gatan GIF 2000™ PEELS and imaging filter, with a (2k 2k) CCD detector. An electron Biprism is also fitted for holographic studies. An overview of the facility is shown in **Figure 1**.

Assessing the performance

The specification included a newly designed objective lens polepiece which combines a C_s value of 0.6 mm with >20° double tilt capability. At the operating voltage of 300 kV, this C_s indicated a Scherzer (point) resolution better than 0.17 nm. The point resolution was initially measured on a thin film of amorphous germanium, as shown in **Fig. 2**. Fourier transforms were obtained using Gatan's Digital Micrograph™

[†]Parks Road, Oxford OX1 3PH, UK.

^{††}South Parks Road, Oxford OX1 3QR, UK
E-mail: john.hutchison@materials.ox.ac.uk

software. Fig. 2 shows an FFT (rotationally averaged to reduce noise) obtained from an image of amorphous Ge, together with a line profile of its intensity distribution. The image was obtained at a defocus of -42 nm, the Scherzer focus of this instrument. The position of the “first zero” in the plot is clearly seen, corresponding to a resolution of 0.16 nm. Additional contrast rings are visible, out to 0.12 nm, indicating an extremely good chromatic damping envelope effect on the contrast transfer function.

As a further test of resolution, a thin $\langle 110 \rangle$ foil of natural diamond was investigated. The unit cell of diamond is small, with $a_0 = 0.356$ nm. Thus in a $\langle 110 \rangle$ lattice image the largest spac-

ings (d_{111}) are 0.206 nm, with smaller spacings also present. A typical $\langle 110 \rangle$ image of diamond is presented in Fig. 3. A much more stringent test using the same diamond specimen is to rotate the specimen around the 220 -axis, to produce a systematic row of 220 -type reflections, corresponding to a lattice spacing of $d_{220} = 0.126$ nm. Since these reflections *cannot* arise from multiple diffraction effects, they cannot be regarded as “half-spacings”; they represent “real” resolution. Fig. 4 illustrates such an image; the 220 fringes with spacing 0.126 nm, are seen clearly, and verified in the accompanying FFT.

Progressing beyond this, we can then tilt the diamond into a 311 - systematic orientation. In

this case *only* 311 -type reflections could contribute to the image contrast, with a spacing of $d_{311} = 0.107$ nm. Again, this is clearly shown in Fig. 5, with verification in the accompanying FFT.

Performance of the electron optical system

Since we are concerned with assessing the overall performance of the instrument, it is also necessary to quantify other electron optical parameters such as ultimate probe size, probe current, etc. This was done in the following tests.

The smallest probe size was recorded and measured by the CCD camera, measuring the



Fig.1. JEM-3000F analytical microscope at Oxford.

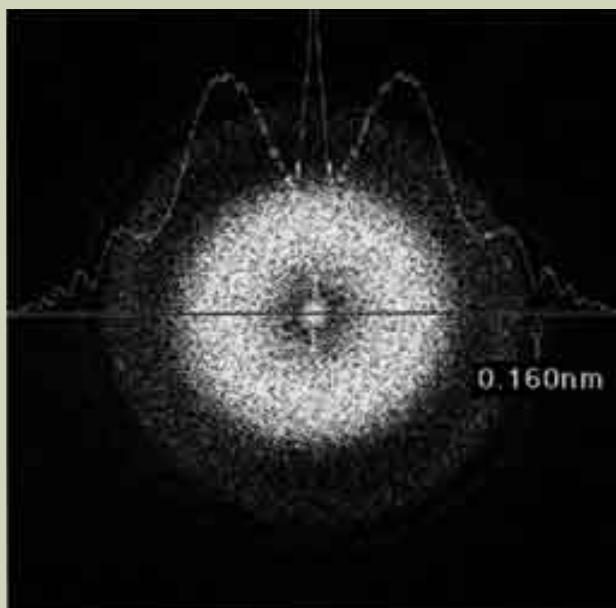


Fig.2. Fourier Transform from amorphous Ge film, at -42 nm defocus indicating point resolution of 0.16 nm. Primary magnification of image: $6000,000$.

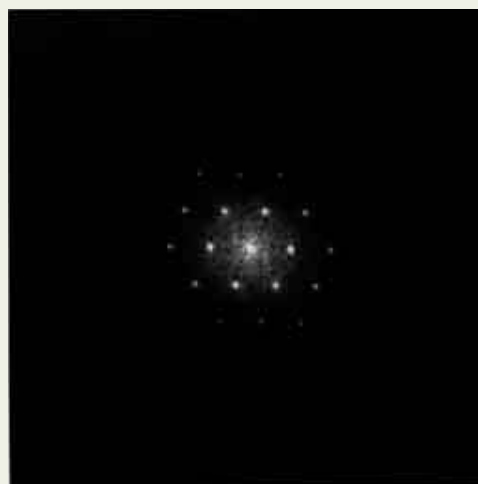
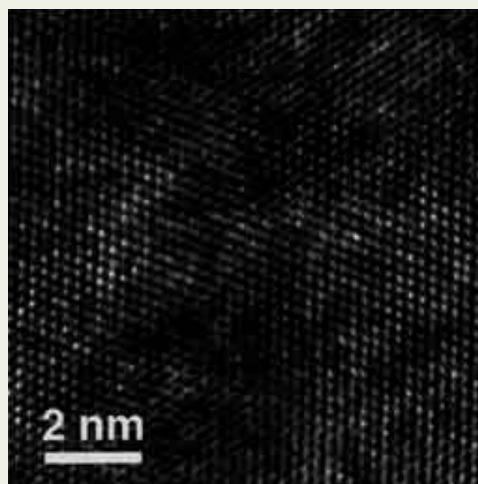


Fig.3. Lattice image of $\langle 110 \rangle$ diamond foil, with corresponding FFT, showing contrast transfer to <0.1 nm.

FWHM at various settings. **Fig. 6** shows the probe at the settings selected to produce the smallest nominal probe diameter of 0.4 nm.

The diameter was measured at FWHM from an intensity profile, and confirmed to be better than 0.4 nm. A probe with a nominal diameter, measured by the same method, of 0.8 nm, produced a probe current of 550 pA.

Probe drift was estimated by comparing a series of images of the focussed small probe (1 nm diameter), over a ten minute period. The combined images are shown in **Fig. 7 a**. This was measured as 0.15 nm/min⁻¹, indicating an extremely stable illumination system. **Fig. 7 b** illustrates our analysis of the probe drift, with movement plotted as a function of time. From this it can be seen that most of the drift occurs within the first few minutes of switching to nano-beam conditions, after which the probe position remains essentially stable.

Energy spread in the electron beam was measured using the PEELS system. This is presented as a zero-loss EELS spectrum, shown in **Fig. 8**, and corresponds to a ΔE of 0.65 eV.

Accuracy of the objective lens alignment was estimated from a beam tilt tableau, where the electron beam incident on a thin amorphous carbon film was progressively tilted by up to 30 mrad around the coma-free axis. This is shown in **Fig. 9**, and again indicates an excellent alignment of the objective lens system.

Initial applications to new materials

Since their discovery almost ten years ago [1] carbon nanotubes have been widely studied by electron microscopy; in particular, the special case of "single wall tubes" (SWTs) have excited much interest on account of their unique structures and properties. The challenge for the materials scientist has been to devise methods of opening their capped ends and filling them with guest materials. At Oxford many systems have successfully been inserted into opened multi-wall carbon nanotubes [2, 3]. More recently attention has been focussed on SWTs, and one of the key projects that will exploit the full capabilities of the new microscope involves complete characterisation of filled SWTs. Methods have been successfully developed at Oxford [4] to fill SWTs with a range of materials; we provide some preliminary examples here. **Fig. 10 a** shows a SWT, of diameter 1.5 nm, which has been filled along its length with CdI₂. The guest material here is effectively a one-dimensional crystal, being completely constrained in its morphology by the enclosing carbon walls. The single atoms in this material are clearly visible. An EDX spectrum obtained from such a nanotube is also shown (**Fig. 10 b**). This confirms the chemical composition as being cadmium iodide.

A second example is a SWT filled with cadmium chloride, shown in **Fig. 11**. In this case the CdCl₂ appears as a double chain, which appears to be helically twisted at certain points along its length (arrows). Again, the composition is verified by EDX, obtained from the single SWT.

Finally, ThCl₄ is also shown inside a SWT - **Fig. 12 a**. In this structure the thorium chlo-

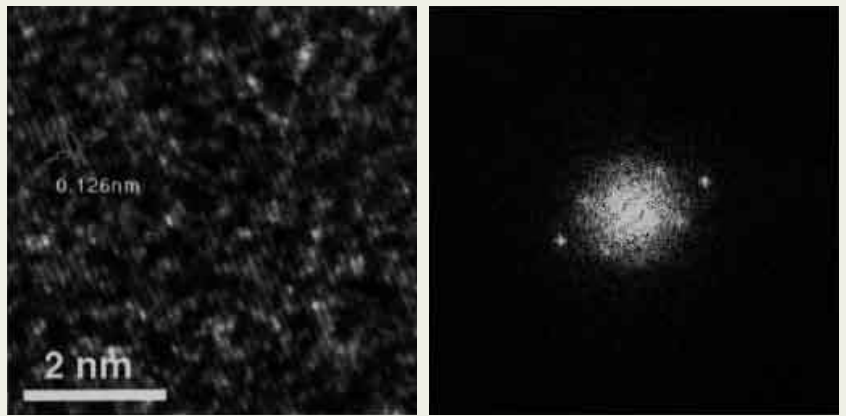


Fig.4. 220 lattice fringe image of diamond, with FFT showing 0.126 nm resolution.

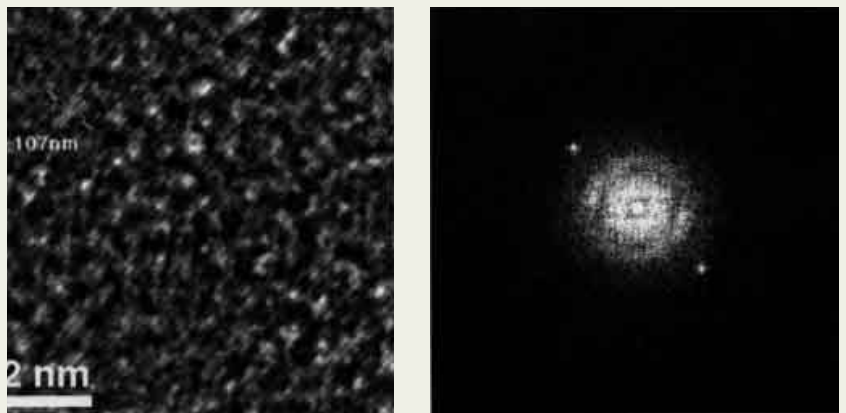


Fig.5. 311 lattice fringe image of diamond, with FFT showing 0.107 nm resolution.

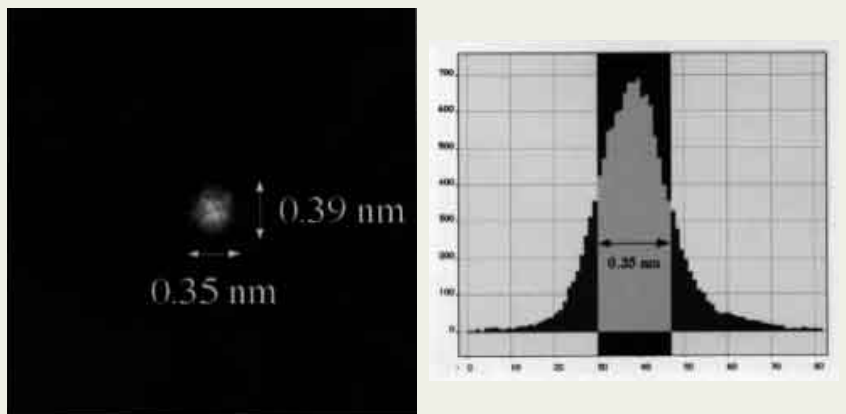


Fig.6. Image of focussed probe, with nominal diameter 0.4 nm.

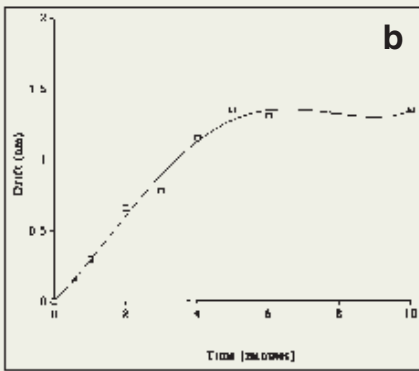
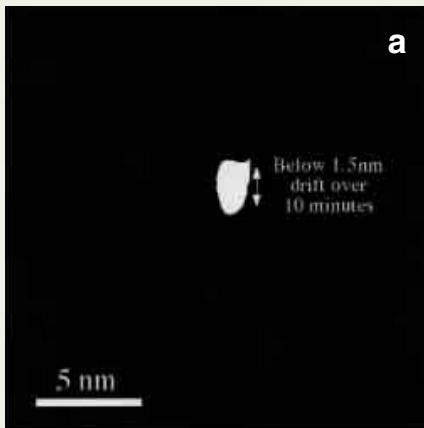


Fig.7. a). Composite image of 0.5 nm probe acquired over 10 mins.
 b). Plot of probe movement versus time.

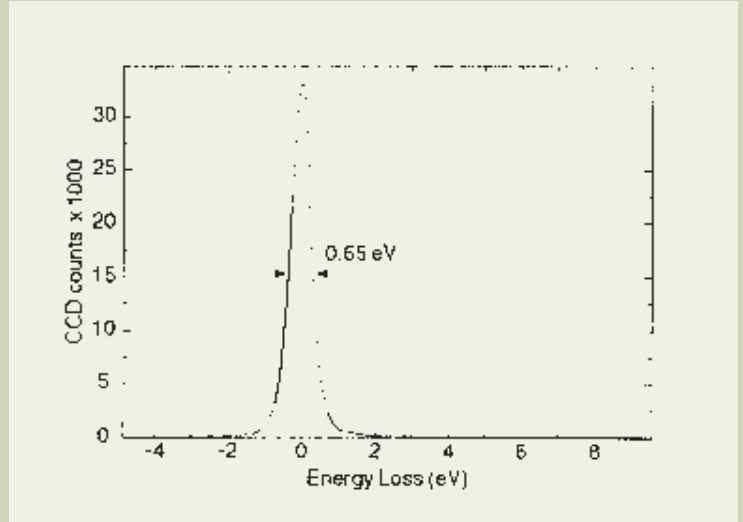


Fig.8. Zero-loss EELS spectrum, showing 0.65 eV energy spread.
 Conditions: 0.05 eV/channel dispersion, 0.6 mm entrance aperture, 0.1 s acquisition time.

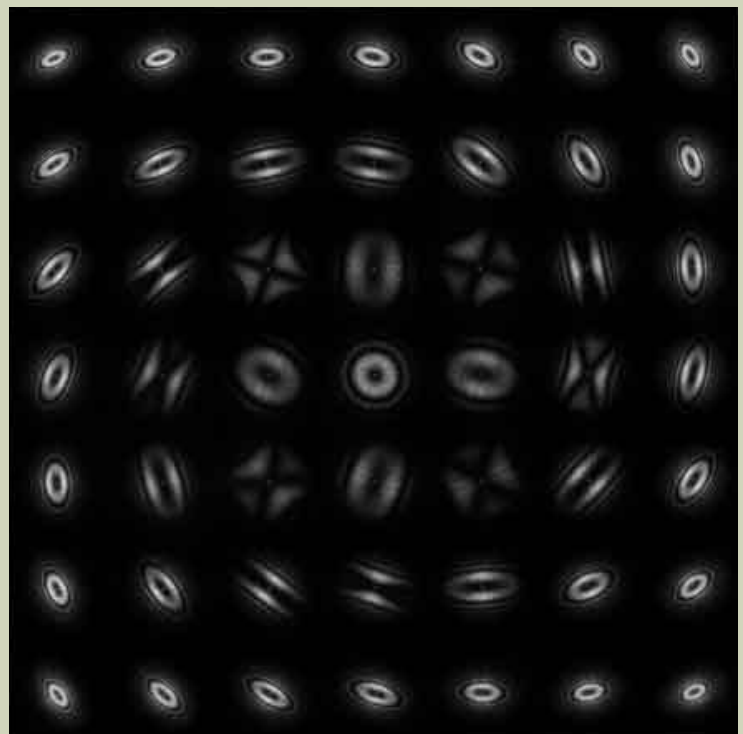
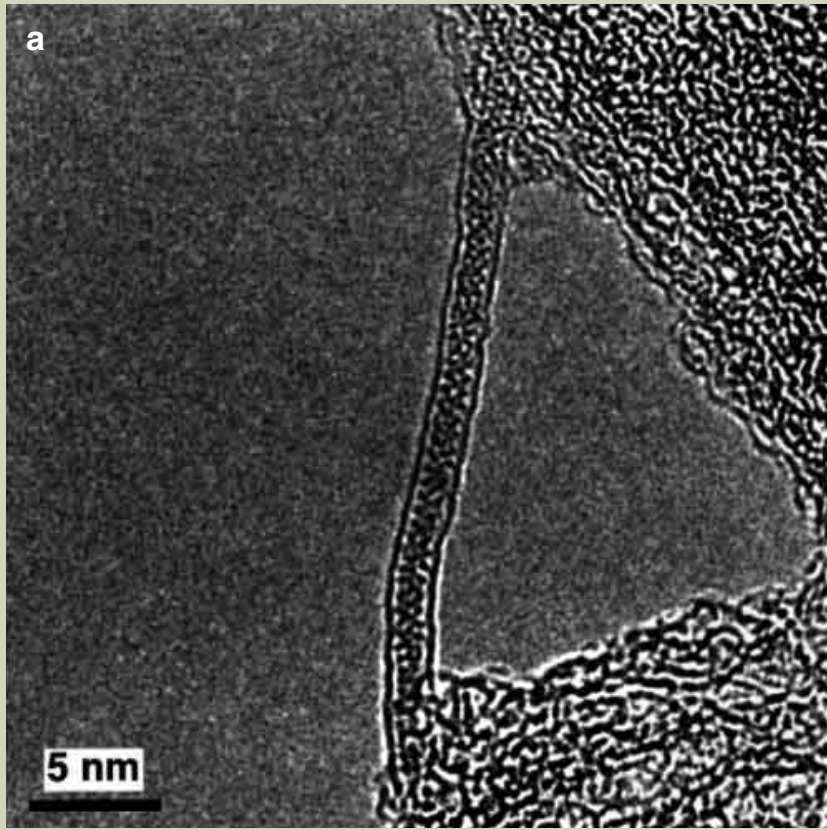


Fig.9. Beam tilt tableau, with up to / 30 mrad tilt in steps of 10 mrad.
 Defocus: -210 nm.



b

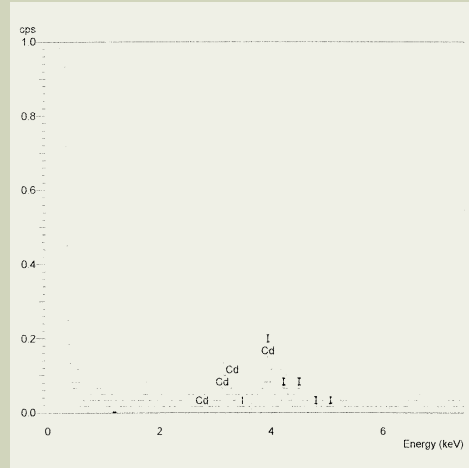


Fig.10.a) Single walled carbon nanotube filled with crystalline CdI_2 .
 b) EDX spectrum from sub-nm area of tube.

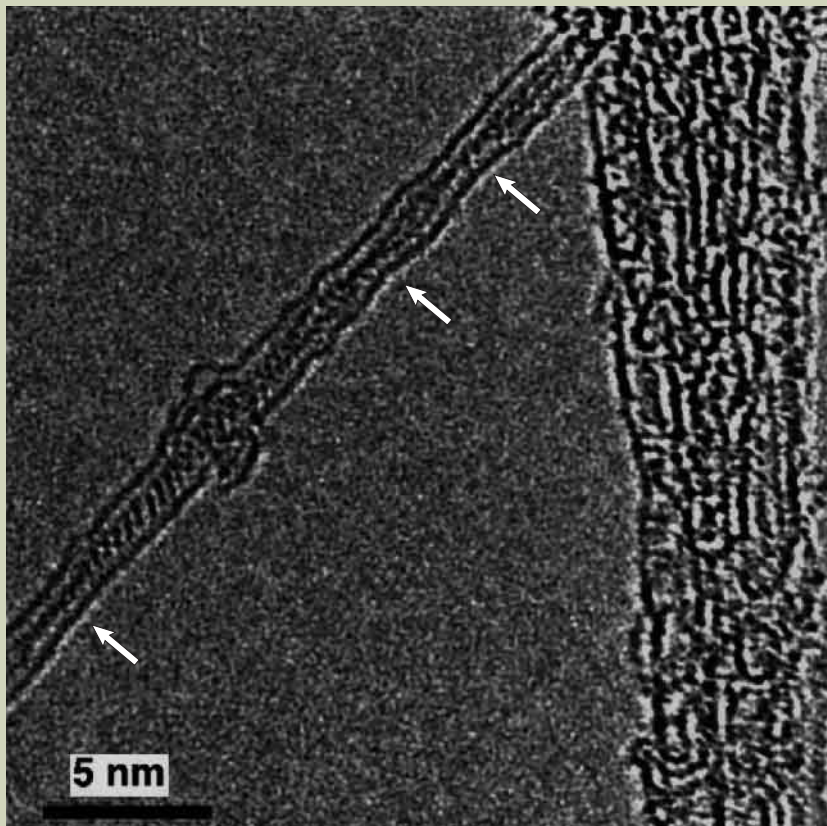


Fig.11. Single walled carbon nanotube filled with crystalline CdCl_2 .

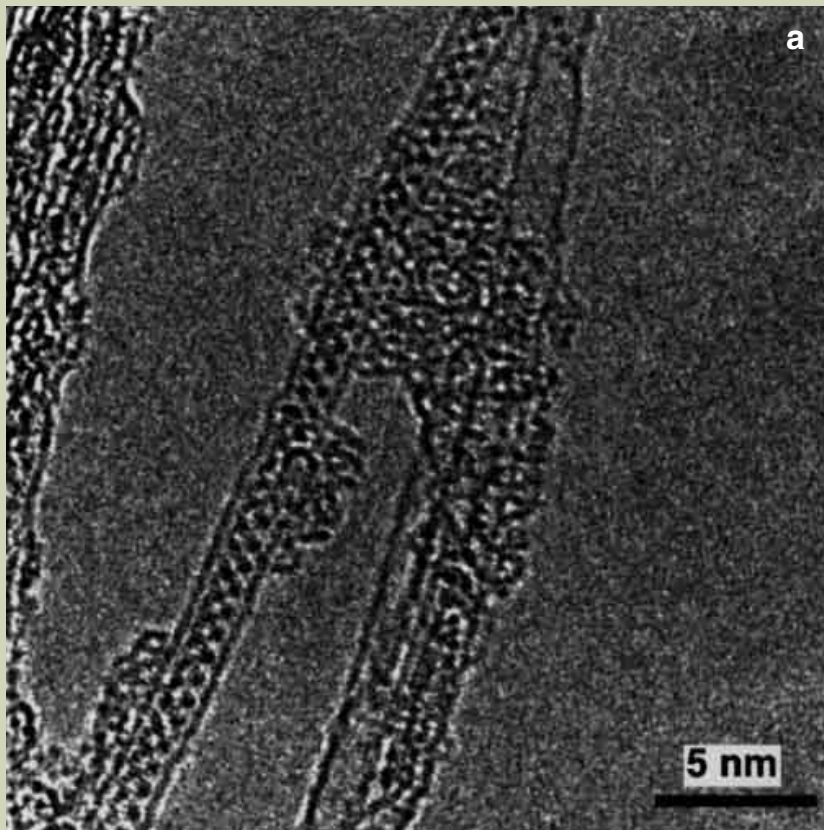


Fig.12. a) Single walled carbon nanotube filled with ordered chains of ThCl_4 .
 b) EDX spectrum from sub-nm area of tube.



ride is present as a linked chain of edge-sharing ThCl_8 units, in a zigzag configuration. This is clearly shown in the image; with confirmation of the composition obtained in the accompanying EDX spectrum (Fig. 12 b).

Conclusion

We have estimated the experimental performance of a JEM-3000F analytical electron microscope, showing that its point resolution to be 0.16 nm, with a capability of producing a small, stable probe down to less than 0.4 nm diameter. The energy spread of the electron beam was measured at 0.65 eV under appropriate conditions. Our initial applications of this instrument have exploited both its high spatial resolution for obtaining atomic images of filled carbon nanotubes, and its high sensitivity EDX capability for analyzing individual nanotubes.

Acknowledgements

This work is supported by the Engineering & Physical Science Research Council. We are also grateful to JEOL Ltd. for its ongoing support. We would also like to thank the following members of the Inorganic Chemistry Laboratory at Oxford for their assistance in the filled SWT synthesis: Kari Coleman, Andrew York, Sam Bailey, Gareth Brown, Cagang Xu and David Wright.

References

1. Iijima S.: *Nature*, **354**, 56 (1991).
2. Cook J., Sloan J., Chu A., Heeson R., Green M. L. H., Hutchison J. L. and Kawasaki M.: *JEOL News*, **32E**, 2-5 (1996).
3. Sloan J., Cook J., Chu A., Zweifka-Sibley M., Green M. L. H. and Hutchison J. L.: *J. Solid State Chemistry*, **140**, 83-90 (1998).
4. Sloan J., Wright D. M., Woo H.-G., Bailey S., Brown G., York A. P. E., Coleman K. S., Hutchison J. L. and Green M. L. H.: *Chem. Comm.* **1999**, 699-700(1999).

Immunogold-labelling in Scanning Electron Microscopy

— Detection of Adhesins at the Surface of Pathogenic *Escherichia Coli* Strains —



Pierre Gounon and Chantal le Bouguéec

(PG) Station Centrale de Microscopie Electronique, (CB) Pathogénie Bactérienne des Muqueuses, Institut Pasteur, Paris, France

Taking advantages of a recent scanning electron microscope equipped with a field emission gun and highly sensitive detectors (semi "in-lens" detector for secondary electron imaging, YAG detector for backscattered electron imaging), we developed a fast and simple protocol enabling double immunogold staining using 10 and 15 nm gold particles. We applied this approach to analyse the afimbrial adhesive sheath produced by pathogenic *Escherichia coli* interacting with the surface of epithelial cells. We demonstrated that AfaE adhesion and AfaD invasion are exposed at the bacterial surface during the interaction process. This method can be easily and largely extended to study early invasion process of many bacterial and viral pathogens by immunocytochemical probing and high-resolution scanning electron microscopy.

Introduction

Since immunogold labelling was introduced by Faulk and Taylor [1], it has become one of the most important tool in electron microscopy. Many valuable contributions have been provided by TEM immunogold procedures either on plastic [2] or on cryosections [3,4]. However thin sections do not allow for the easy localisation of surface antigens (i.e.

receptors), generally present in a few copies only at the cell surface. These antigens can easily be missed and, the sparse immunostaining obtained is hardly convincing. To overcome these difficulties immuno replica techniques represent fine structural alternatives. Despite several successful and very delicate applications, the preparation of such immuno replica need careful manipulations requiring skilled experience.

Alternatively, SEM offers three-dimensional analysis of the cell surface, does not necessitate delicate manipulations and with the SEM objectives field depth the observation of highly structured surfaces is comfortable. Moreover large areas can easily be observed.

SEM immunocytochemistry was introduced by Horisberger and co-workers [5-8] and De Harven [9,10]. They used large colloidal gold particles detected with secondary electron mode. Despite the large size of colloidal gold particles originally used (> 30 nm), the immunogold labelling method has rapidly become a powerful technique for surface labelling in electron microscopy.

The recent introduction of field emission scanning electron microscopy with enhanced brightness at high magnifications has enabled the detection of small gold particles (5 nm or

less), thus increasing the overall quality of immunocytochemical probing [11]. However direct examination of small colloidal gold particles by secondary electron mode remains thoroughly difficult to discern through small details or artefacts of the labelled surface. It seemed thus much easier to use the backscattered electron mode in order to unambiguously localise gold particles scattered on the surface. Highly sensitive BSE detectors are essential for the detection of the signal produced by small colloidal gold particles. Single crystal scintillators of the YAG type (Ce³⁺ doped Yttrium Aluminium garnet) have proven to be very adapted for this purpose [12].

Field emission scanning electron microscopes provide small beam diameters at low accelerating voltages. It is therefore possible to use secondary electron images to observe surface structures with enough details at high resolution even in the absence of surface coating such as gold, gold-palladium or chromium [13] while keeping the same working parameters that yield a BSE image evidencing colloidal gold particles with high contrast.

However use of small particles (5 nm) may not be the optimal approach since it requires high working magnification that decreases the field of view. Particles of 10 to 15 nm have

Abbreviations

BSA ;	Bovine Serum Albumin
NGS ;	Normal Goat Serum
PBS ;	Phosphate Buffered Saline
HMDS ;	Hexamethyldisilazane
BSEI ;	Backscattered Electron Imaging
HR-SEM ;	High Resolution Scanning Electron Microscopy

proven to represent a good compromise allowing observation of large surface areas with good immunocytochemical sensitivity and labelling precision.

We have applied these approaches to analyse by High Resolution Scanning Electron Microscopy (HR-SEM) the afimbrial adhesive sheath produced by pathogenic *Escherichia coli* interacting with the surface of epithelial cells.

Expression of adhesins is a major virulence factor of pathogenic *Escherichia coli* strains. In most cases adhesins are associated with bacterial cell surface structure called fimbriae [for review see Ref.14]. However, in some cases, adhesins have been reported not to be associat-

ed with fimbriae [15]. We demonstrated that the afimbrial adhesive sheath encoded by the *afa-3* gene cluster is composed of two adhesins respectively called AfaE-III and AfaD [16]. Moreover we have shown adhesion of *afa*-expressing *E. coli* strains associated with intestinal or urinary tract infections are mediated by AfaE protein [17] that recognises the decay-accelerating factor as receptor [18]. Moreover AfaD protein was demonstrated to be involved in invasion of HeLa cells [17]. With conventional TEM, bacteria expressing these Afa proteins were seen embedded in microvillar extensions of HeLa cells.

In order to analyse the interaction of *afa*-expressing strains with epithelial cells, we

have examined by HR-SEM immunocytochemistry the localisation of AfaE and AfaD proteins at the bacteria-HeLa cells binding sites after three hours of interaction.

Materials and Methods

Preparation of infected cells

HeLa cells were grown on 12 mm round coverslips. At semi confluence they were infected with *E. coli* HB101 carrying a plasmid encoding for an afimbrial adhesive sheath composed of AfaD and AfaE-III [16]. After 3 hours incubation, non adherent bacteria were washed with culture medium. The cells were then fixed with 1% glutaraldehyde in 0.1M phosphate buffer pH 7.4 for 30 min at 4 °C.

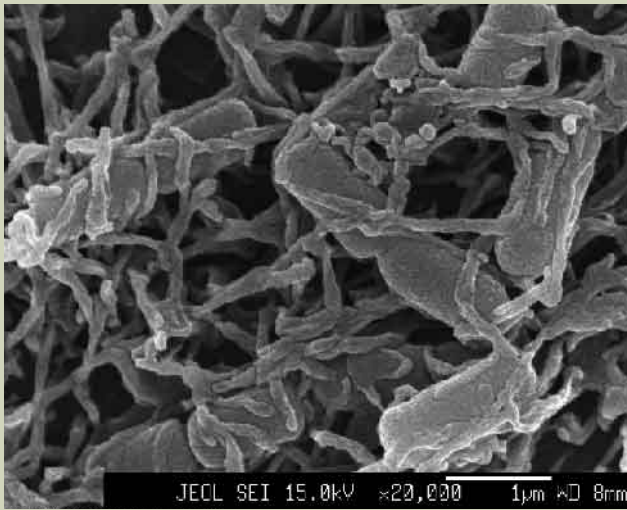


Fig.1. Secondary electron imaging of HB101 (pILL 1101) strain adhering to the surface of HeLa cell. Bacteria are highly enwrapped in microvillar extensions of the cell surface. Preparation was only coated with a thin layer of carbon (see Materials and methods) .

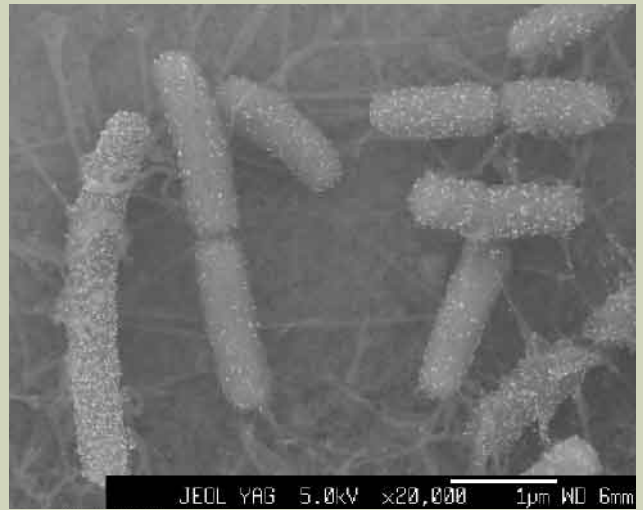


Fig.2. Backscattered electron imaging of immunogold staining of AfaE adhesin of pathogenic *Escherichia coli*. AfaE protein has been probed with 15 nm gold conjugate, thus allowing easy observation of relatively large area.

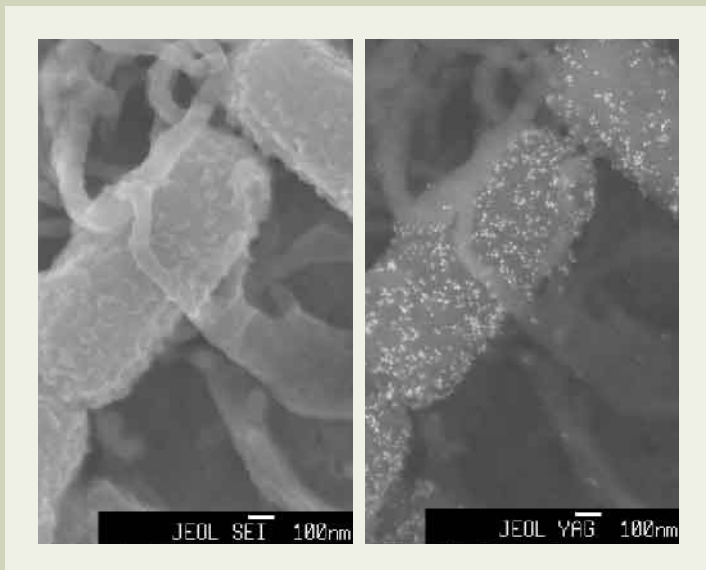


Fig.3. Immunogold staining of AfaE adhesin produced by pathogenic *Escherichia coli* strain. AfaE was probed with 15 nm gold conjugate. Left panel: secondary electron imaging. Right panel: backscattered electron imaging.

After fixation they were carefully washed with PBS and processed for immunocytochemistry.

Immunocytochemistry

Each coverslip was deposited face down on top of a small drop (10 μ L) of the following solutions : PBS 50mM NH₄Cl (10 min) ; PBS 1% BSA 1% NGS (5 min) ; anti AfaE-III or anti AfaD diluted in PBS 1% BSA 1% NGS antiserum raised either in rabbit or in mouse (30 min) [16] ; PBS 0.1% BSA (two washes, 5 min) ; colloidal gold conjugated anti-rabbit or anti-mouse IgG antibodies (10 or 15 nm) (British Biocell International, Cardiff, UK) diluted 1/20 in PBS, 0.01% fish skin gelatine (30 min) ; PBS (2 min) ; distilled water (2 min).

Preparation for scanning electron microscopy

Coverslips with cells attached on their surface were dehydrated in an increasing ethanol series then treated with Hexamethyldisilazane (Polysciences, EppelHeim, Germany) as described by Bray *et al.* [19] for 10 min. Excess of HMDS was evaporated under the air flux of a chemical hood. The coverslips were then coated with a 3 nm thick carbon layer.

Preparations were observed with a JSM-6340F SEM (JEOL Ltd., Tokyo, Japan) operating at 5-7 kV and equipped with "semi-in lens" detector for secondary electron imaging and YAG detector for backscattered electron

imaging.

The resolution of the microscope is currently 1.5 nm in the range 5 - 7 kV for the secondary electron imaging mode, the maximal resolution being 1.2 nm at higher accelerating voltage.

Images were stored as electronic files with 1280 \times 1024, 8 bits per pixels in bitmap format..

Observations

Cells with bacteria attached on their surface were observed in secondary electron imaging mode (**Fig. 1**) at medium voltage (15 kV). The adherent bacteria intimately interacted with elongated microvilli of the surface of HeLa

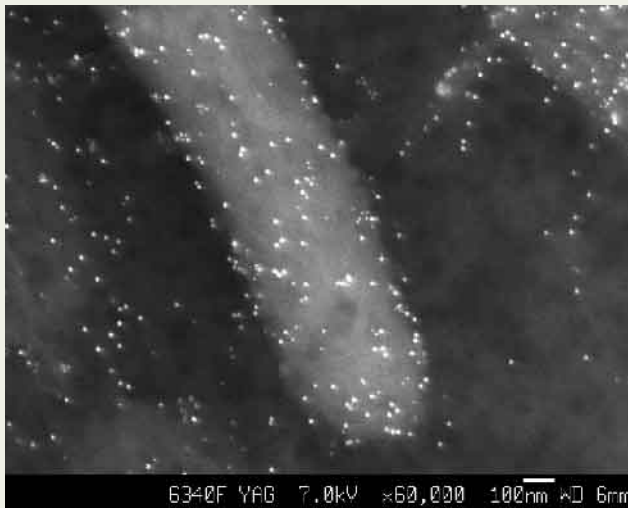


Fig.4. Backscattered electron imaging (BSEI) of double immunogold staining of two surface adhesins produced by pathogenic *Escherichia coli* strains. AfaE adhesin has been probed with 10 nm gold particles, AfaD adhesin with 15 nm gold particles. With BSEI, the surface relief is relatively poor; however, one can easily observe bright dots due to backscattered electrons produced by colloidal gold particles. At this intermediate magnification it is readily possible to discriminate 10 and 15 nm gold particles.

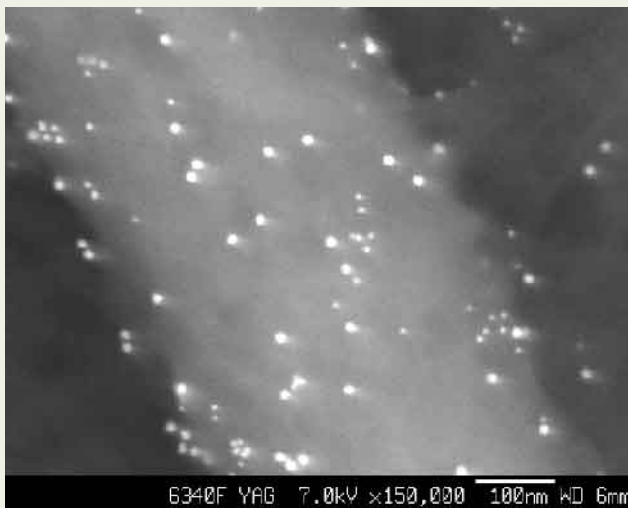


Fig.5. Backscattered electron imaging (BSEI) of double immunogold staining of two surface adhesins produced by pathogenic *Escherichia coli* strains. At high magnification both gold particles (10 and 15 nm) can be unequivocally distinguished.

cell. At this acceleration voltage, the image closely resembles the standard SEI observations reference despite the absence of any surface coating with heavy metals (i.e. gold or chromium). Decreasing the acceleration voltage to 5 kV did not reduce the sharpness of the image (Fig. 2). Switching to the backscattered electron detector allows to clearly see colloidal gold particles (10 nm) even at this relatively low magnification (Fig. 2).

AfaE adhesin remained strictly localised to the bacterial surface and did not spread over the entire surface of the host cell (Fig. 3). We extended these observations to double immunostaining of AfaE and AfaD adhesins (Fig. 4). The bacteria were similarly labelled with the two antisera. AfaD was previously shown necessary for internalization of bacteria but able to detach from the bacterial surface during cultures of pathogenic strain leading to the question of how AfaD could promote bacterial entry [17].

Conclusion

With the introduction of SEM equipped with a field emission gun working at a reduced primary beam voltage without compromising the resolution, associated to highly sensitive detectors (SEI or BSEI) placed in a new position defined by a new design of the column and the objective, it was possible to easily detect colloidal gold immunostaining on cell surface. Moreover these enhanced characteristics of modern SEM allow the introduction of double immunostaining using two sizes of gold particles (i.e., 10 and 15 nm, Fig. 4 and Fig. 5). We have introduced a very simple protocol for the preparation of cells and bacteria based on an optimised immunocytochemical method associating very low background, high sensitivity and fast protocol coupled to a simplified method of drying using HMDS [19] which has been shown to be well adapted to soft and highly hydrated specimens.

Moreover, it was not necessary to realise a surface coating with heavy metals (gold, palladium, platinum, chromium) as previously recommended by many authors [20].

A thin layer of carbon (3nm) seemed sufficient to insure good conductivity when the accelerating voltage was maintained low (5-7 kV or lower) and perhaps not necessary. However this possibility was not really examined. With the described conditions it is definitely possible to use smaller size of colloidal gold particles (i.e., 5 nm), however this demands higher magnifications, thus both reducing the field of observation and requiring a more precise focusing of the objective. In this case rapid search over large field of view becomes relatively time-consuming. With this method we have been able to prove the presence of both AfaE and AfaD proteins produced by uropathogenic and diarrhoea associated *Escherichia coli* strains at the surface of bacteria

This method can be greatly helpful in the characterisation of physiopathological process of infections provoked by uropathogenic and diarrhoea associated *Escherichia coli* strains. It is now possible to develop correlative immunogold microscopy between transmission electron microscopy and scanning elec-

tron microscopy using the same gold probes. This method could easily be extended to localise relatively scarce antigens as cellular receptors using the capacity of SEM to observe large areas.

Acknowledgements

We thank Pascale Courcoux for her technical assistance. We warmly thank JEOL (EUROPE) S.A (Croissy sur Seine, France) for the use of their scanning electron microscope facilities.

References

1. Faulk W. P. and Taylor G. M.: An immunocolloid method for the electron microscope. *Immunochemistry*, **8**, 1081-1083 (1971).
2. Bhandari M.: Colloidal gold post-embedding immunocytochemistry. *Prog. Histochem. Cytochem.*, **29**, 1-163 (1995).
3. Griffiths G.: *Fine structure Immunocytochemistry*, Springer Verlag, Berlin (1993).
4. Liou W., Geuze H. J. and Slot J. W.: Improving structural integrity of cryosections for immunogold labeling. *Histochem. Cell Biol.*, **106**, 41-58 (1996).
5. Horisberger M. and Rosset J.: Colloidal gold, a useful marker for transmission and scanning electron microscopy. *J. Histochem. Cytochem.*, **25**, 295-305 (1977).
6. Horisberger M. and Rosset J.: Localization of alpha-Galactomannan on the surface of *Schizosaccharomyces pombe* cells by scanning electron microscopy. *Arch. Microbiol.*, **112**, 123-126 (1977).
7. Horisberger M., Rosset J. and Bauer H.: Colloidal gold granules as markers for cell surface receptors in the scanning electron microscope. *Experientia*, **31**, 1147-1149 (1975).
8. Horisberger M., Rosset J. and Bauer H.: Localization of mannan at the surface of yeast protoplasts by scanning electron microscopy. *Arch. Microbiol.*, **109**, 9-14 (1976).
9. De Harven E., Leung R. and Christensen H.: A novel approach for scanning electron microscopy of colloidal gold-labeled cell surfaces. *J. Cell Biol.*, **99**, 53-57 (1984).
10. Albrecht R. A. and Hodges G. M.: *Biotechnology and bioapplications of colloidal gold*, Scanning Microscopy International, Chicago (1988).
11. Hermann R., Walther P. and Muller M.: Immunogold labeling in scanning electron microscopy. *Histochem. Cell Biol.*, **106**, 31-39 (1996).
12. Walther P., Aufrata R., Chen Y. and Pawley J. B.: Backscattered electron imaging for high resolution surface scanning electron microscopy with a new type YAG-detector. *Scanning Microscopy*, **5**, 301-310 (1991).
13. Peters K. R.: Metal deposition by high-energy sputtering for high magnification electron microscopy. In *Advanced techniques in biological electron microscopy*. Vol. 3: Koehler J. K. editor. Springer-

Verlag, Berlin. 101-106 (1986).

14. Finlay B.B., Cossart P. Exploitation of mammalian host cell functions by bacterial pathogens. *Science*, **276**, 718-725 (1997).
15. Le Bouguéne C., Garcia M. I., Ouin V., Desperrier J. M., Gounon P. and Labigne A.: Characterization of plasmid-borne *afa-3* gene clusters encoding afimbrial adhesins expressed by *Escherichia coli* strains associated with intestinal or urinary tract infections. *Infect. Immun.*, **61**, 5106-5114 (1993).
16. Garcia M. I., Gounon P., Courcoux P., Labigne A. and Le Bouguéne C.: The afimbrial adhesive sheath encoded by the *afa-3* gene cluster of pathogenic *Escherichia coli* is composed of two adhesins. *Molec. Microbiol.*, **19**, 683-693 (1996).
17. Jouve M., Garcia M. I., Courcoux P., Labigne A., Gounon P. and Le Bouguéne C.: Adhesion to and invasion of HeLa cells by pathogenic *Escherichia coli* carrying the *afa-3* gene cluster are mediated by the AfaE and AfaD proteins, respectively. *Infect. Immun.*, **65**, 4082-4089 (1997).
18. Nowicki B., Labigne A., Moseley S., Hull R., Hull S. and Moulds J.: The Dr hemagglutinin, afimbrial adhesin AFA-I and AFA-III, and F1845 fimbriae of uropathogenic and diarrhea-associated *Escherichia coli* belong to a family of hemagglutinins with Dr recognition. *Infect. Immun.*, **58**, 279-281 (1990).
19. Bray D. F., Bagu J. and Koepler P.: Comparison of Hexamethyldisilazane (HMDS), Peldri II and critical-point drying methods for scanning electron microscopy of biological specimens. *Microsc. Res. Techn.*, **26**, 489-495 (1993).
20. Albrecht R. M., Prudent J., Simmons S. R., Pawley J. and Choate J. J.: Observations of colloidal gold labelled platelet microtubules: high voltage electron microscopy and low voltage-high resolution scanning electron microscopy. *Scanning Microscopy*, **3**, 273-278 (1989).

Measurement of Contact Potential Difference using an Ultrahigh Vacuum Noncontact Atomic Force Microscope



Shin'ichi Kitamura, Katsuyuki Suzuki and Masashi Iwatsuki

Electron Optics Division, JEOL Ltd.

An ultrahigh vacuum scanning Kelvin probe force microscope (UHV SKPM) based on the electrostatic force gradient has been developed utilizing the technique of a UHV noncontact atomic force microscope (NC-AFM) having atomic resolution. It can be used for simultaneous observation of a contact potential difference (CPD) between the cantilever tip and sample surface and topographic images due to NC-AFM. In the CPD images on the Au deposited Si(111) surface after annealing, the potential difference between the 7×7 and 5×2 structures was clearly resolved. On the Ag deposited Si(111) 7×7 surface a potential resolution of less than 10 meV was demonstrated with an atomic level resolution in the UHV SKPM. The change of surface potential corresponding to the charges on the insulated surface of polypropylene has been observed with the molecular resolution. We also demonstrated a reliable method to obtain the CPD from the bias voltage dependence curves of the frequency shift in all of the scanning areas. In this method it is consistent with comparing the barrier height images by STM in that the work functions of adatoms are greater than that of corner holes.

Introduction

The scanning Kelvin probe force microscope (SKPM) belongs to the scanning probe microscope (SPM) family, and was derived from the noncontact atomic force microscope (NC-AFM) technique. Using the SKPM, the contact potential difference (CPD) originating from the work function difference between the tip and sample surfaces can be measured. The work function of the sample surface is obtained by measuring the CPD using a tip of known work function. The lateral difference of work function on the sample surface, which is caused by the difference of elements and orientation of crystal, can also be observed as the CPD mapping. The surface potential difference corresponding to some charges on the surfaces of insulators can be observed as well. Most of the CPD images in the SKPM are acquired in the atmosphere [1-4]. However, the work function is sensitive for the surface oxidation and absorption. Thus, in order to accurately obtain the work function of a clean surface as well as the changes in the work function due to surface treatment, the imaging in an ultrahigh vacuum (UHV) condition is desired. This is also effective to prevent the

electrical discharge on the insulator surfaces.

UHV NC-AFM is a powerful enough microscope to verify atomic resolution [5-7]. High resolution imaging in a typical UHV NC-AFM uses a cantilever whose spring constant is relatively high ($>$ a few N/m). The use of such a cantilever makes efficient and accurate the measurement of the interaction between the tip and sample by detecting a resonance frequency shift of the cantilever as a force gradient, and this is superior to the direct measurement from the cantilever deflection [8]. While the conventional SKPM, designed to detect the electrostatic force between the tip and sample by the deflection of cantilever, is unable to achieve atomic resolution of topographic images, SKPM using the force gradient in the same fashion as the UHV NC-AFM has achieved an atomic resolution in topographic images and a higher resolution in CPD images [9, 10].

When there is a potential difference U between the tip and sample, the electrostatic force between them is expressed as

$$F = (1/2) U^2 C / Z, \quad (1)$$

where C is the effective capacitance between the tip and sample, and Z the distance between the tip and sample. The force gradient is given

by

$$F / Z = (1/2) U^2 C / Z^2. \quad (2)$$

Since the force gradient is proportional to the square of the potential difference U , the force gradient can be used to measure U instead of the force. Thus, in SKPM, we used the force gradient method in NC-AFM, and simultaneously observed CPD and topographic images.

We have obtained the CPD images of clearly resolved 7×7 and 5×2 phases on Au/Si(111) surface, atomic level lateral resolution as well as topography images on Ag clusters deposited Si(111) 7×7 structure. Also, the change of the surface potential on polypropylene film due to distortion of polypropylene chains has been observed in UHV SKPM. Furthermore, we demonstrated a reliable method without SKPM function to obtain the CPD from the bias voltage dependence curves of the frequency shift in all of the scanning area.

Experimental

The variation of electrical potential with voltage applied between the tip and sample is shown schematically in **Fig. 1**. If the work function of the sample surface is larger than that of the tip ($\phi_s > \phi_t$), then the electrostatic

force corresponding to the work function difference (ϕ is CPD) generates as the Fermi levels (E_F) of the tip and sample becomes the same level under no applied voltage (Fig. 1 b), but no electrostatic force generates when the voltage $V_{DC} = \phi/q$ is applied between the tip and sample (Fig. 1 a). The tip voltage (V_{Tip}) dependence on the force gradient between the tip and sample for the grounded sample is shown in Fig. 2. When we oscillate the tip voltage (V_{Tip}) as $V_{DC} + V_{AC} \sin(\omega t)$, the gradient of electrostatic force (F_E/Z) is modulated as shown in this figure. If V_{DC} is equal to ϕ/q , the signal of the force gradient has the period of 2π (the point A), but for the other values of V_{DC} the ω component appears to cause a modulation (the point B). This scheme can be used to detect the amplitude of the ω component by using a lock-in amplifier, where the output of the lock-in amplifier becomes zero for $V_{DC} = \phi/q$. When V_{DC} coincides with the zero of output in the lock-in amplifier, it gives the CPD between the sample surface and tip. CPD images are obtained from a feedback loop that maintains the lock-in output at zero. The gradient of electrostatic force is detected as the shift of cantilever resonance frequency. The relative CPD images can be also obtained without this feedback loop by directly measuring the lock-in output under the assumption of its linear change against the tip voltage.

Figure 3 shows a block diagram of the system used in our experiment. The dotted line in the figure indicates the portion of the UHV NC-AFM for topographical imaging [8], and the solid line indicates the portion added for CPD measurement as SKPM.

In the NC-AFM, the force gradient between the tip and the sample is detected as a shift of the resonance frequency of the cantilever. As shown in Fig. 3, the cantilever is oscillating with resonance frequency under the application of positive feedback from the optical deflection detection system to the piezo through the preamplifier with band pass filter, phase shifter, waveform converter and attenuator. The frequency of the oscillating cantilever is detected by an FM demodulator (FMD) shown in Fig. 3. The phase-locked loop (PLL) was used as the FMD. Feedback is applied to the Z piezo to keep the constant shift of resonance frequency. The shift of the resonance frequency is determined by the reference voltage (Ref. V) of the error amplifier (Error AMP1).

The resonance frequency of the cantilever will also be changed due to the change of the electrostatic force gradient between the tip and sample caused by a voltage [$V_{DC} + V_{AC} \sin(\omega t)$] applied to the tip from the oscillator (Osc.) and the error amplifier (Error AMP2). This change will appear as a change of an output of FMD, and a value corresponding to the 1st derivative of U in the formula (2) is detected by the lock-in amplifier. When this output is zero, the effect of the electrostatic force gradient becomes minimum. The DC voltage (V_{DC}) is fed back to the cantilever tip by the Error AMP2 to minimize the electrostatic force gradient. V_{DC} equals CPD between the tip and sample, so that the distribution of CPD for the tip is obtained simultaneously with the topog-

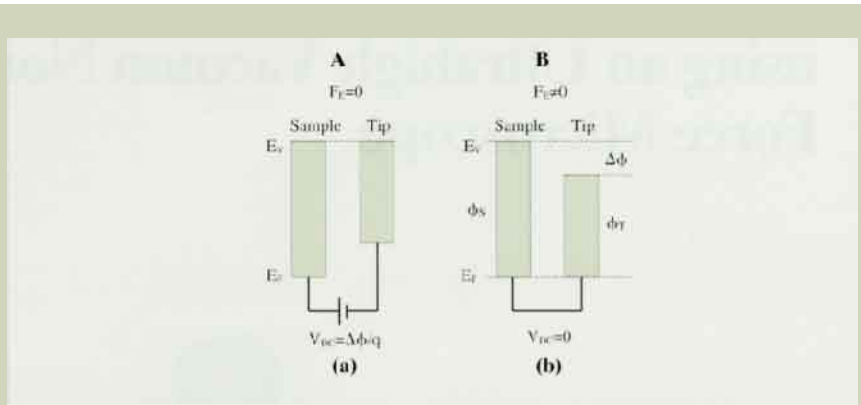


Fig.1. Schematic of electrical potential variation with voltage applied between the tip and sample. (a) No electrostatic force occurs when $V_{DC} = \phi/q$. (b) The electrostatic force corresponding to the ϕ/q component appears when $V_{DC} = 0$.

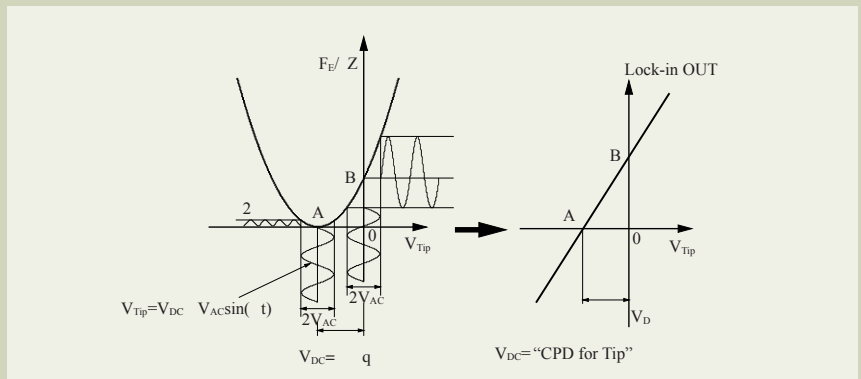


Fig.2. Schematic illustration of the tip voltage dependence of the frequency shift for a grounded sample. The tip voltage oscillation is $V_{Tip} = V_{DC} + V_{AC} \sin(\omega t)$. When $V_{DC} = \phi/q$ the signal of force gradient has a period of 2π , and when $V_{DC} \neq \phi/q$ component appears because of modulation. When the amplitude of ω component is detected by the lock-in amplifier, the output will become zero when $V_{DC} = \phi/q$.

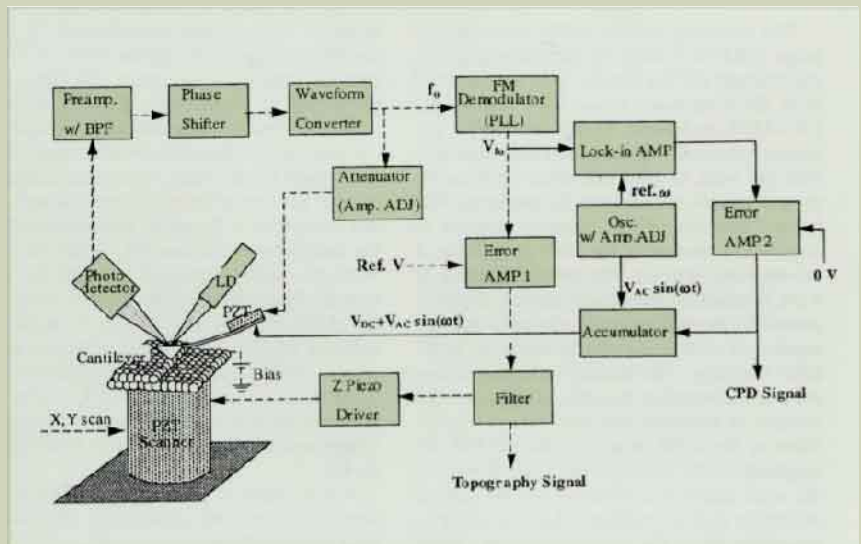


Fig.3. Block diagram of the NC-AFM system and CPD measurement system.

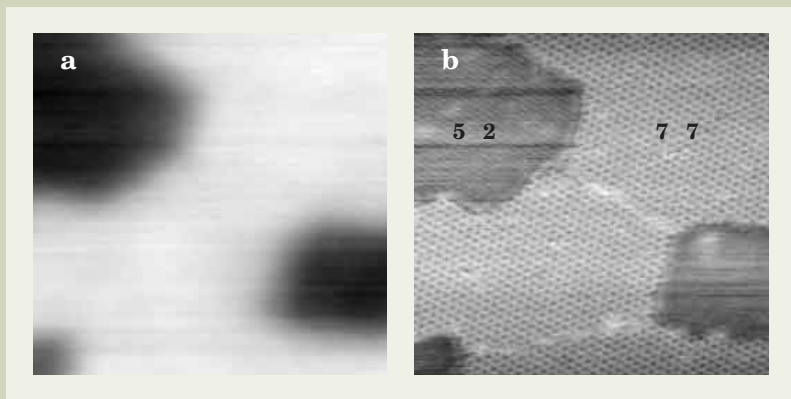


Fig.4. Relative CPD and NC-AFM images of an Au/Si (111) surface with 7×7 and 5×2 phases in an area of $100 \times 100 \text{ nm}^2$ [9]. No feedback of V_{DC} voltage for the tip was used.

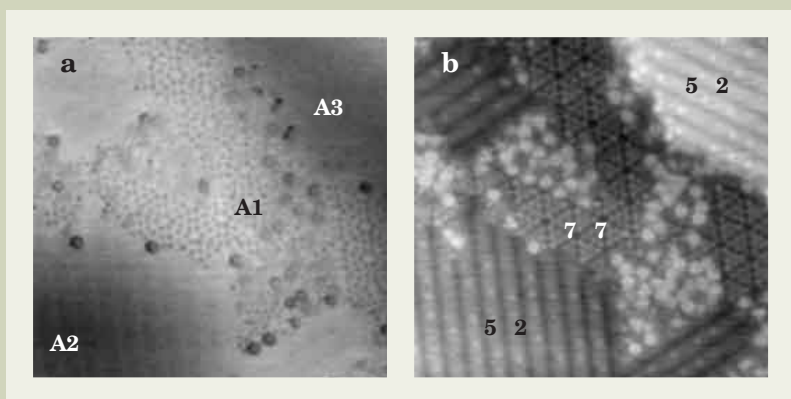


Fig.5. Relative CPD and NC-AFM images of an Au/Si (111) surface with 7×7 and 5×2 structures in an area of $30 \times 30 \text{ nm}^2$. Average potential difference in the CPD image is about 70 meV between A1 and A2 and about 50 meV between A1 and A3.

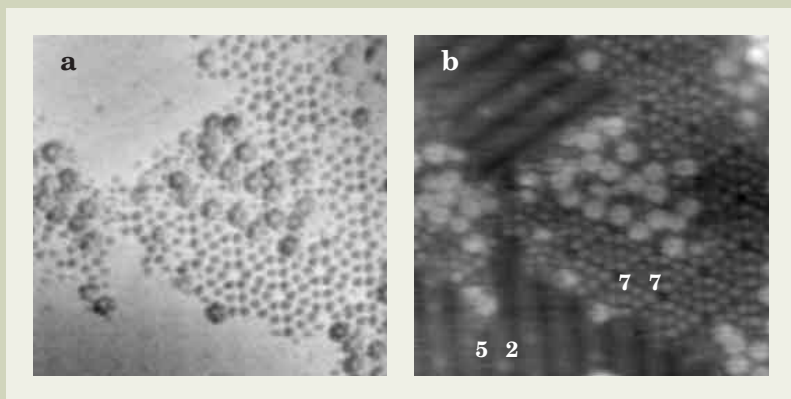


Fig.6. Magnified images of the relative CPD and NC-AFM of an area of $20 \times 20 \text{ nm}^2$. Obtained after several scans of Fig.5 observation.

raphy image of NC-AFM. During the relative CPD image observation, the system uses a lock-in amplifier and an oscillator.

We also carried out another method for the CPD measurement as a current imaging tunneling spectroscopy (CITS) for scanning tunneling microscopy (STM). In this method, the sample bias voltage dependence curves of the frequency shift is measured on each pixel of the topography image. The scan range of bias voltage is $\pm 1 \text{ V}$ in 128 points.

The NC-AFM system used is a JEOL JAFM-4500XT [8] (it is now called JSPM-4500A). A commercial conductive Si cantilever is sputter-coated with approximately 50 nm of Au. Typically, the cantilever has a resonance frequency of about 250 kHz and a spring constant of about 30 N/m. The vacuum pressure during imaging is less than 10^{-8} Pa . CPD and NC-AFM images are simultaneously observed. The scan speed during the simultaneous observation is 1.7s/line. The oscillation frequency and amplitude of the voltage applied to the tip is 1 or 2 kHz and 1 or 3 V_{P-P} for Si samples and 5 V_{P-P} for the polypropylene film. In the sample preparations, the Au and Ag deposits on Si (111) 7×7 surface were carried out on the AFM stage and the polypropylene film was not treated.

Results and Discussion

Relative CPD imaging (without feedback of V_{DC})

Figure 4 (a) and 4 (b) show the relative CPD and NC-AFM (topography) images of an Au/Si (111) surface with 7×7 and 5×2 phases in an area of $100 \times 100 \text{ nm}^2$ [9]. An AC voltage with amplitude of 3 V_{P-P} and frequency of 1kHz was applied to the tip, and no feedback voltage of V_{DC} shown in Fig. 3 was used. The polarity was set so that CPD images would be darkened when the sample bias voltage was negative. The 7×7 structure in NC-AFM image of Fig. 4 (b) has been observed as a mesh of the 7×7 unit cell. So, the bright and dark regions in CPD images correspond to 7×7 and 5×2 phases, respectively.

The potential difference between 7×7 and 5×2 phases in the CPD image was about 0.45 eV_{P-P} , which was calculated by the change of the output voltage from the lock-in amp when the sample bias voltage was changed. The CPD image demonstrates the potential difference between the different phases. As a result, the 5×2 -Au structure on Si(111) surface has a higher work function than the 7×7 structure of Si (111), showing a good agreement with the reported data [11] of Au and Si.

Figure 5 (a) and 5 (b) also show the relative CPD and NC-AFM images of an Au/Si (111) surface with 7×7 and 5×2 structures in an area of $30 \times 30 \text{ nm}^2$. An AC voltage with amplitude of 1 V_{P-P} and frequency of 2 kHz was applied to the sample and the tip was virtually grounded. So, it is similar to Fig. 4. The NC-AFM image was not only observed with the high resolution but the CPD image. The average of potential difference between 7×7 and 5×2 surfaces (the areas is marked by A1 and A2 in the CPD image), was about 70 meV. Also the potential difference between the area of A1 and of A3 was about 50 meV. Although the relationship of difference is consistent with

that of Fig. 4, these values are smaller than that. This is probably due to the fact that the CPD depends on the area size and the long range interaction of electrostatic force. As the 7×7 structure has been confirmed in the CPD image, however, it is considered that the lateral resolution has reached the atomic level.

Although the particles like impurities have been observed in the NC-AFM image, all the particles in the NC-AFM image were not observed as dark spots in the CPD image. **Figure 6 (a) and (b)** show magnified images of the relative CPD and NC-AFM of in an area of $20 \times 20 \text{ nm}^2$, which were obtained after observation of Fig. 5 and then several scanning. Most of the particles observed in the NC-AFM image appeared as dark spots in the CPD image. While the 7×7 structure in the NC-AFM image of Fig. 6 has been observed like an empty state image of STM, that of Fig. 5 has been observed like a filled state image of STM. This is probably due to the fact that the tip apex of the cantilever atomically changes because of touching the surface during the scanning. Regarding the CPD images, Fig. 6 is

more correctly observed than Fig. 5, because the corresponding particles in both the CPD and NC-AFM images have been observed in Fig. 6.

CPD imaging (with feedback of V_{DC})

Figures 7 and 8 show two $20 \times 20 \text{ nm}^2$ scans of the simultaneously acquired CPD (a) and NC-AFM images (b) for Si (111) 7×7 surfaces after Ag evaporation [9]. The Ag coverage in Fig. 7 is larger than that in Fig. 8, and the NC-AFM image demonstrates that most of the area is covered by Ag clusters with a hexagonal island. For these images, a voltage feedback loop was applied to the tip potential to show the direct CPD values for the tip. The contrast in Fig. 7 (a) is considered to be due to the difference in work function between the Ag island and Ag clusters. The work function of the island is observed to be higher than that of the clusters by about 20 meV. The mesh shown at the bottom in Fig. 8 corresponds to a 7×7 unit cell. In the CPD image, most of the

bright regions correspond to Ag clusters marked by the arrows. Thus, the CPD image was observed with atomic level resolution, discriminating the Ag clusters deposited on the faulted half of Si (111) 7×7 unit cells. The contrast in Fig. 8 (a) is considered to be due to the difference in work function between the 7×7 structure and Ag clusters. The work function of the 7×7 structure is observed to be higher than that of the cluster by about 10 meV. The results indicate $\text{island} > 7 \times 7 > \text{cluster}$. This relationship of the work functions is in a good agreement with previous data [11] when the Ag cluster is regarded as a Ag polycrystal and the Ag island as a Ag (111) surface.

Figure 9 (a) and (b) show the potential and NC-AFM images of the polypropylene film and the polypropylene chains are clearly resolved on the (110) crystal facet in the NC-AFM image [10]. These images were simultaneously observed in an area of $10 \times 10 \text{ nm}^2$. In the boundary of the facets (shown by the arrows), the potential is lower by roughly 0.6 eV. **Figure 10 (a) and (b)** also show the potential and NC-AFM images of the polypropylene film in an area of $10 \times 10 \text{ nm}^2$. In these images, the frequency shift corresponding to force gradient was decreased in the middle of the scan. In the NC-AFM image, the polypropylene chain was distorted at the upper side corresponding to larger frequency shift. It is considered that the potential difference was caused by the piezoelectric effect. The distortion observed in the image is believed to be caused by a repulsive force between the tip and sample making a larger frequency shifts. However, no discharges took place during the observation, suggesting that noncontact imaging conditions exist in spite of the location of the tip and sample causing a net repulsive force between the tip and sample.

CPD measurement from bias voltage dependence curves

Figure 11 shows the frequency shift of bias voltage dependence curves on the 7×7 and 5×2 structure on the Au/Si (111) surface. The superimposed topography image in an area of $50 \times 50 \text{ nm}^2$ has the bias voltage dependence curves of the frequency shift in each pixel of the image, so these curves were obtained by selecting area after imaging by using the CITS function in our software. The work function differences are about 0.1 eV between 7×7 and 5×2 . These results were obtained by a second-order polynomial fit of the voltage dependence curves. The results show the work function of 5×2 structure was larger than that of 7×7 structure. We confirmed this relationship in the first paragraph on the results. Although the value is remarkably different from that of Fig. 4, it is close to Fig. 5. Because the width of 5×2 region in this image is smaller than that of Fig. 4 and almost the same as the width of 7×7 region in Fig. 5. It is considered that the determinable area of threshold for the work function exists and in that narrow area of a few scores nm^2 the work function is dependent on the area size.

Figure 12 also shows the frequency shift of bias voltage dependence curves of average on about 0.13 nm^2 areas of the center adatoms, corner adatoms and corner holes respectively

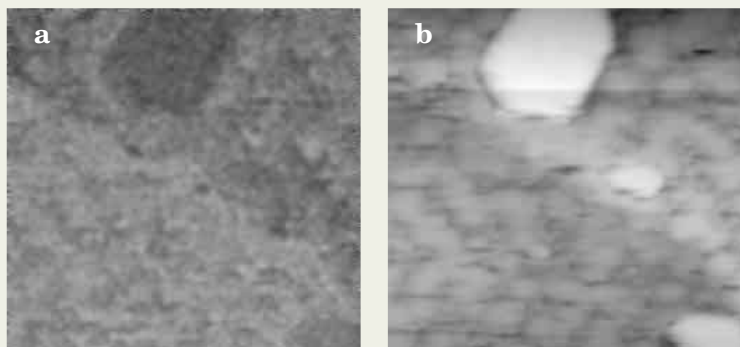


Fig. 7. Simultaneously acquired CPD (a) and NC-AFM (b) images of the Si (111) 7×7 surface with Ag deposits. The scan size was $20 \times 20 \text{ nm}^2$. The work function of the Ag island was approximately 20 meV higher than that of Ag clusters.

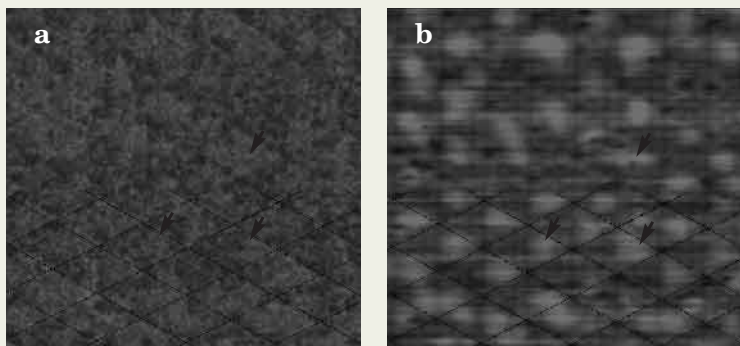


Fig. 8. Simultaneously acquired CPD (a) and NC-AFM (b) images of the Si (111) 7×7 surface with Ag deposits. The Ag coverage was less than Fig. 7. The scan size was $20 \times 20 \text{ nm}^2$. The work function of 7×7 was approximately 10 meV higher than that of Ag cluster.

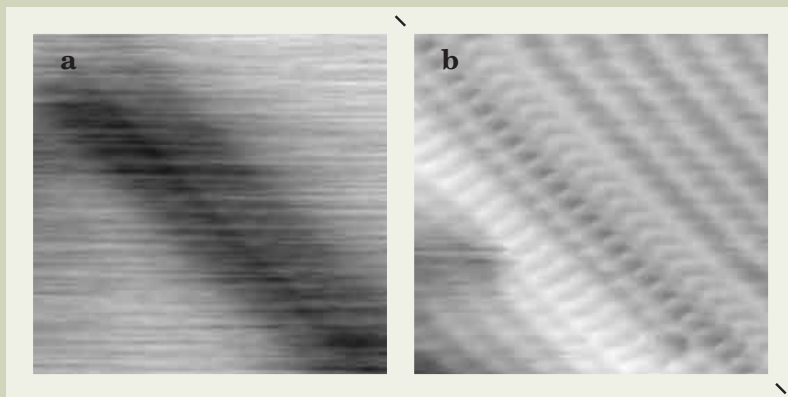


Fig.9. Simultaneously acquired potential (a) and NC-AFM (b) images of the polypropylene film. The scan size is $10 \times 10 \text{ nm}^2$. The polypropylene chains are clearly resolved on the (110) crystal facet in the NC-AFM image. At the edge of the facet, the potential is lower by roughly 0.6 eV.

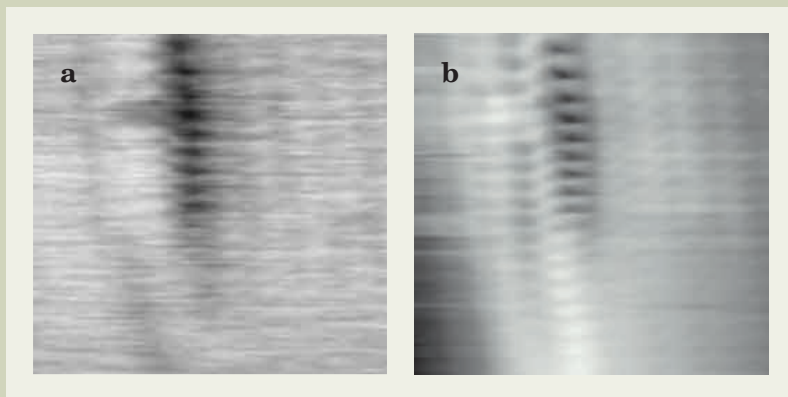


Fig.10. Simultaneously acquired potential (a) and NC-AFM (b) images of the polypropylene film in which the frequency shift was decreased during the middle of scan. In the NC-AFM image, the polypropylene chain was distorted in the larger frequency shift. And the changes of potential appear in the potential image.

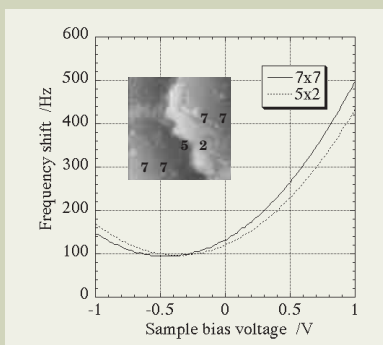


Fig.11. The frequency shift of bias voltage dependence curves on the 7×7 and 5×2 structure on the Au/Si(111) surface. The superimposed topography image in an area of $50 \times 50 \text{ nm}^2$ has the bias voltage dependence curves of the frequency shift in each pixel of the image. These curves were obtained by selecting area after imaging. The work function differences are about 0.1 eV between 7×7 and 5×2 .

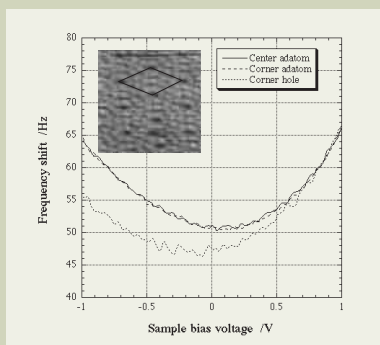


Fig.12. The frequency shift of bias voltage dependence curves of several average areas of about 0.13 nm^2 on the center adatoms, corner adatoms and corner holes respectively of Si(111) 7×7 in an area of $10 \times 10 \text{ nm}^2$. The average of work function on an adatom is higher than that on a corner hole by about 0.17 eV.

in a unit of 7×7 structure shown in figure. The average of work function on an adatom is higher than that on a corner hole by about 0.17 eV. These results were obtained by a second-order polynomial fit of the voltage dependence curves. The value is different from the previous calculation [10], because the curves on the adatoms vary depending on the position and size of the area without obvious position dependence. However, the result of $\phi_{\text{adatom}} > \phi_{\text{hole}}$ in the work function coincides with the previous one. It is also consistent with the CPD image in Figs. 5 and 6 and the barrier height images by STM on Si(111) 7×7 surface [12, 13].

Conclusions

We have described the methods to measure the CPD between the tip and sample, using the UHV NC-AFM. The CPD images both with and without the tip voltage feedback demonstrating atomic level resolution with a surface potential resolution of less than 10 meV could be obtained in the SKPM based on the force gradient with the UHV NC-AFM. The change of potential corresponding to charges on the insulating surface of polypropylene has also been observed with UHV SKPM. We have also demonstrated a reliable method to obtain the CPD from the bias voltage dependence curves giving the frequency shift in the whole scanning area. In this method, the results are consistent with those obtained by SKPM.

References

- Weaver J. M. R. and Abraham D. W.: *J. Vac. Sci. Technol.*, **B9**, 1559 (1991).
- Nonnenmacher M., O'Boyle M. P. and Wickramasinghe H. K.: *Appl. Phys. Lett.*, **58**, 2921 (1991).
- Henning A. K., Hochwitz T., Slinkman J., Never J., Hoffmann S., Kaszuba P. and Daghlia C.: *J. Appl. Phys.*, **77**, 1888 (1995).
- Hochwitz T., Henning A. K., Levey C., Daghlia C., Slinkman J., Never J., Kaszuba P., Gluck R., Wells R., Pekarik J. and Finch R.: *J. Vac. Sci. Technol.*, **B14**, 440 (1996).
- Giessibl F. J.: *Science*, **267**, 68 (1995).
- Kitamura S. and Iwatsuki M.: *Jpn. J. Appl. Phys.*, **34**, L145 (1995).
- Ueyama H., Ohta M., Sugawara Y. and Morita S.: *Jpn. J. Appl. Phys.*, **34**, L1086 (1995).
- Kitamura S., Suzuki K. and Iwatsuki M.: *JEOL News*, **32E**, 42 (1995).
- Kitamura S. and Iwatsuki M.: *Appl. Phys. Lett.*, **72**, 3154 (1998).
- Kitamura S., Suzuki K. and Iwatsuki M.: *Appl. Surf. Sci.*, **140**, 265 (1999).
- CRC Handbook of Chemistry and Physics. 65th. ed., CRC Press, Florida, p. E-76 (1984).
- Kurokawa S., Yuasa M., Sakai A. and Hasegawa Y.: *Jpn. J. Appl. Phys.*, **36**, 3860 (1995).
- Horiguchi N., Yonei K. and Miyao M.: *Jpn. J. Appl. Phys.*, **36**, 3864 (1995).

Microscopic Chemical State Analysis by FE-SAM with Hemispherical Energy Analyzer



Yuji Sakai, Masato Kudo, Takahisa Yamada, Nobuyuki Ikee and Yuji Nagasawa

Electron Optics Division, JEOL Ltd.

Scanning Auger microprobe (SAM) equipped with a field emission (FE) gun and a hemispherical energy analyzer (HSA) has been developed for Auger analysis of micro-area with a high energy resolution. A FE-gun with a small source size and a high brightness is used for micro-area analysis. HSA has a property of high energy resolution and the energy resolution is controlled electrically. In this paper, the technical improvements on the new FE type electron optical column and the HSA with a multi-channel detector system are presented with the typical applications of Auger micro-area analyses.

Introduction

Auger electron microprobe has been used as an analytical tool for elemental distribution of thin or multi-layer materials and structures of micro-devices. These analyses need the enhanced spatial resolution for micro-area analysis and high energy resolution spectra for analysis of chemical bonding states. For requirement to improve the performance of Auger microprobe, FE-SAM (JAMP-7830F) was equipped with a newly designed optical system with a ZrO/W Schottky field emission (FE) gun, a new objective lens and an image drift compensation system. An advantage feature of the new electron optical system is ability to analyze micro-areas. Furthermore, the hemispherical energy analyzer (HSA) was installed as Auger detector in the ultrahigh vacuum scanning electron microscope. The new Auger system provides high image resolution and high beam stability. In general, HSA or concentric hemispherical analyzer (CHA) is usually used in X-ray photoelectron spectroscopy (XPS), because XPS for chemical state analysis needs high energy resolution spectra. By combination of HSA with the scanning electron microscope with FE gun, Auger chemical state analysis was possible in micro-area. In this paper, the technical improvements on the new FE type electron optical column and HSA with the multi-channel detector system are presented with applications of Auger micro-area analysis.

1. Features of FE type electron optical system

1) High spatial resolution

According to the trend of semiconductor

devices towards down sizing less than several ten nm by the device rule, the performance of SAM is required to have a spatial resolution of 10nm for micro-area analysis. JAMP-7830F equipped with a FE-gun shown in **Fig. 1** provides the capability of micro area analysis with 10 nm resolution. By using a Schottky field emitter, the source size is smaller than 10nm diameter. It is about 1/100 of the LaB₆ source size and the current stability is several % per hour as with a LaB₆ cathode. Furthermore, a position compensation system for specimen drift during analysis is attached to a controller system of the electron optical column and is very useful for high magnification analysis [1].

2) Largest beam current

The electron optical system of SAM needs a largest beam current with smaller beam size for Auger analysis, especially, the FE-gun is effective when the probe current exceeds several ten nA for Auger analysis. The demagnification by the electron optical system for the field emitter is within one order of magnitude, so the aberration term of the first condenser lens is no more ignored. One of methods to reduce the aberration coefficients is to shorten the working distance between the emitter and the first condenser lens. The first condenser lens is newly designed to reduce the aberrations. The polepiece of the first condenser lens is located beneath the anode, the resulting principal focal plane of the first condenser lens is between the anode and the extractor as shown in Fig. 1. In the arrangement shown in Fig. 1, the magnetic field (B) of the condenser lens is highest between the anode and the extractor, and the condenser lens is located within the

acceleration field (E) of the electron beam. The design of the first condenser lens lead to reduction of lens aberrations and beam spread for FE gun. These electron optical systems provide a beam size of several nm and a probe current of several hundred nA.

2. Features of electron energy analyzer

1) High energy resolution and sensitivity

For the use of the HSA in Auger electron spectroscopy (AES) [2], a new HSA detection system was developed. This system consists of three functions, i.e., the input lens system, the HSA and the multi-channel detection system. The sensitivity of the Auger detection system depends on the design of the input lens system and the multi-channel detection system installed with the HSA. The input lens system is designed to effectively detect the signal from a point source on the specimen. The design of input lens system has been carried out by computer simulation. The aberration of the input lens system affects the beam shape inside the HSA, and lowers the detection efficiency for the HSA. The spherical aberration coefficient of new input lens was decreased to 1/3 of that of the previous one. This makes the increase of the sensitivity [3].

HSA is an energy dispersive spectrometer and the electrons passed through between electrostatic deflectors focus at the output plane of HSA by separating the electron energy. The multi-channel detectors placed at the dispersion position on the output plane detect all available signals of a spectrum. The sensitivity increases proportionally to the number of detectors introduced. The constant retarding

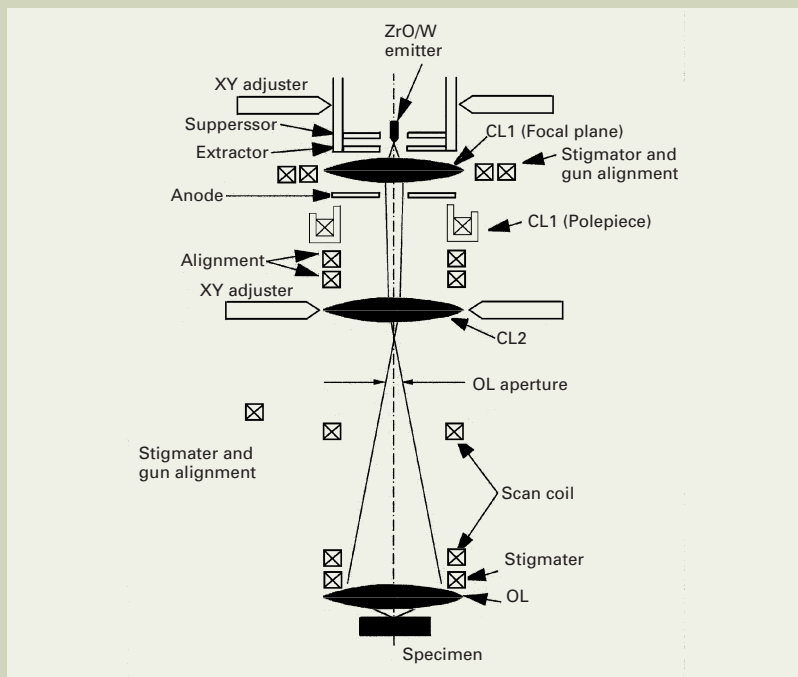


Fig.1. Auger microprobe with FE electron optical system.

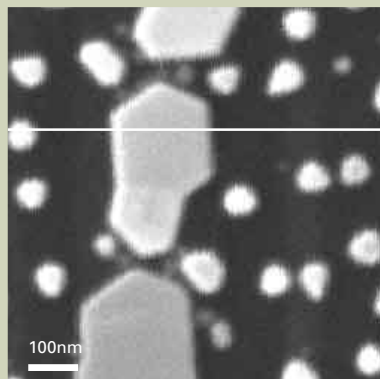


Fig.2. SEM image of Au on the graphite is measured at 25 kV primary electron beam energy and 2 nA beam current.

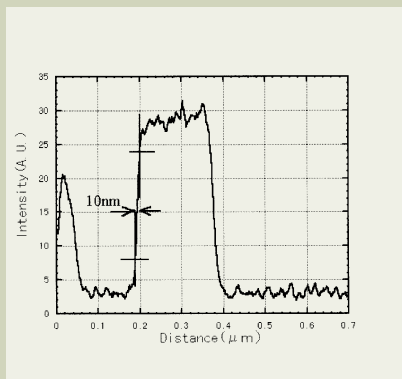


Fig.3. Au Auger line profile at showing Auger line analysis position in Fig.2. P is the intensity of Au-NOO at 66eV and B is the background at 80 eV.

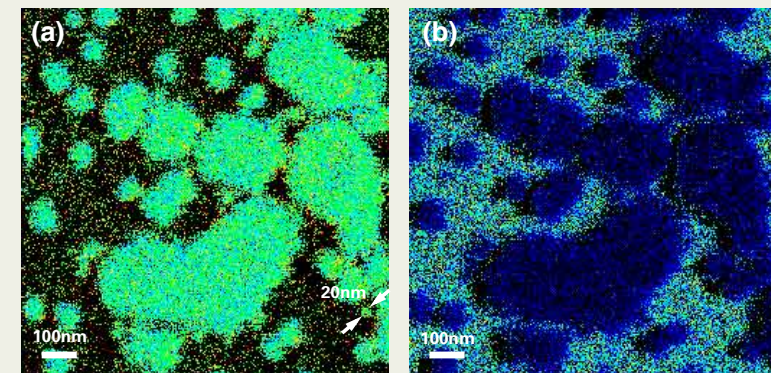


Fig.4. Au (a) and C (b) Auger images are measured at the same beam condition of the line analysis and the different position on the same specimen.

ratio (CRR) or the constant relative resolution mode is used for AES analyses. In this mode, the retarding ratio is decided as the ratio of pass energy divided by the retarding energy. The analyzing energy of spectrometer are scanned by changing the retarding potential while keeping the retarding ratio. The energy of electrons are decelerated by a constant ratio from their initial kinetic energies and analyzed by the potential difference between deflectors of HSA. The relative resolution (E/E_0) of the measured spectra is kept at constant.

The multi-channel detectors consisting of the channeltrons detect dispersed electrons with different energies. The new detection system consisting of several channeltrons detects the dispersed electrons at the dispersion plane and corrects the energy dispersion. Data acquired from each channeltron by sweeping the retarding potential are consolidated into a single spectrum. The energy dispersion correction method for the data acquisition allows the HSA in the use of AES.

2) Reliability for HSA

The measurement of the spectra in a low energy range from 0 to 100eV is very difficult and requires the reliability of HSA and the less magnetic flux of the objective lens or the stray field. The special magnetic shield case is equipped inside the analyzing chamber to reduce the magnetic flux. Still more, the unique objective lens is designed to prevent the spreading of magnetic flux on the specimen. This magnetic shield technique is capable of the measurement of the low energy electron spectra with sufficient reliability. A typical example of the low energy electron spectra is the measurement of the true secondary electron spectra. The work function is obtained by the onset energies of the secondary electron spectra [4]. These capabilities will provide new applications of the work function for micro-areas.

3. Applications

1) High spatial resolution analysis

To check the Auger spatial resolution, the Auger line profile was analyzed for a gold particle evaporated on a graphite substrate. A primary electron beam with an energy of 25kV and 2nA measured by a Faraday cage built in the electron optical column was used to take a scanning electron image shown in Fig. 2. The line scan was performed across the gold particle along a line on the scanning electron image shown in Fig. 2. The line scan of the Au-NOO Auger signal is shown in Fig. 3. The spatial resolution is about 10 nm estimated by a distance corresponding to the change of the Au intensity at the sharp edge from 20% to 80% of the value. The Auger images of Au and C taken by the same condition of the primary beam and the same area of specimen are shown in Fig. 4 (a) and (b). The image drifts of these images were compensated by the probe tracking software. The Au Auger image of the Au particle with a 20 nm diameter (arrows) is clearly observed in Auger image.

2) High energy resolution spectra

The energy resolution of HSA is changed by controlling the retarding ratio electrically. The

relative energy resolution (E/E_0) changes from 0.03 to 0.8%. **Fig. 5** shows the Si-KLL Auger spectra of Si and SiO₂ mixture sample measured at different energy resolutions of 0.5%, 0.35% and 0.15%. The Auger peaks for Si and SiO₂ can be separated clearly with the energy resolution of 0.15% but not separated with the energy resolution of 0.5%. These results show the energy resolution for Auger chemical analysis needs a lower value than 0.15%.

3) Auger chemical depth analysis

The Auger spectra of Si-KLL for Si, SiO₂ and Si₃N₄, and the chemical state mapping for each chemical state were shown in the paper [3]. In this experiment, the chemical depth analysis for multilayers of SiO₂ and SiON_x on Si substrate were measured. **Fig. 6.** shows the Auger spectra as a function of depth which is used to analyze the change of spectrum shape. The number of each spectrum shows the depth level from the surface to the substrate. No.1 spectrum corresponds to the top surface. The spectra of number 9 and 23 depth levels were taken out from the depth profile data. The number 9 spectrum shows the interface including two states of SiO₂ and SiON_x and the number

23 spectrum including two states of SiON_x and Si. These spectra were analyzed by the curve fitting method using the synthesized spectra of Gaussian-Lorentzian function. **Fig. 7** and **Table 1** show the analyzed data for spectra of number 9 and 23. Each Si-KLL spectrum is separated into 4 peaks of SiO₂ and SiON_x, and 5 peaks of SiON_x, Si and Si-loss. The calculation were carried out by using the most rapid of the non-linear least means square techniques to obtain the best fitting between measured spectra and synthesized spectra. An Auger line shape consists of asymmetric peaks and includes a large background. Therefore the best ways is to use the measured standard spectra instead of the Gaussian-Lorentzian functions. The curve fitting by using the measured standard spectra will be expected to provide more exact analytical values for mixtures of different chemical state.

4. Summary

FE-SAM with the new FE optical system was designed to get the minimum probe size and the largest beam current. The HSA is applied in Auger electron spectroscopy in order to decrease the input lens aberrations

and improve the detection sensitivity. By this technique, the FE-SAM with HSA allows Auger chemical state analysis in a nanometer dimension. The applications of depth analysis show the capability of Auger chemical analysis in the depth direction as well as XPS. Moreover, by improving the reliability of HSA, the work functions are measured from the onset energy of the secondary electron spectrum and the measurement of barrier height of the p-n junction is possible.

References

1. Yamada T., Kudo M., Ando Y., Sekine T. and Sakai Y.: *Applied Surface Science*, **100/101**, 287-291 (1996).
2. Sekine T., Ikeo N. and Nagasawa Y.: *Applied Surface Science*, **100/101**, 30-35 (1996).
3. Sakai Y., Kudo M., Yamada T., Ikeo N. and Nagasawa Y.: *Journal of Surf. Analysis*, **5**, 173-176 (1999).
4. Sakai Y., Yamada T., Suzuki T., Ito H. and Ichinokawa T.: *Appl. Phys. Lett.*, **73**, 611 (1998).

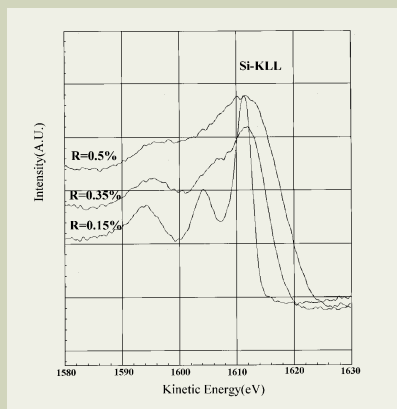


Fig.5. Si-KLL Auger spectra with 0.15%, 0.35% and 0.5% of energy resolution.

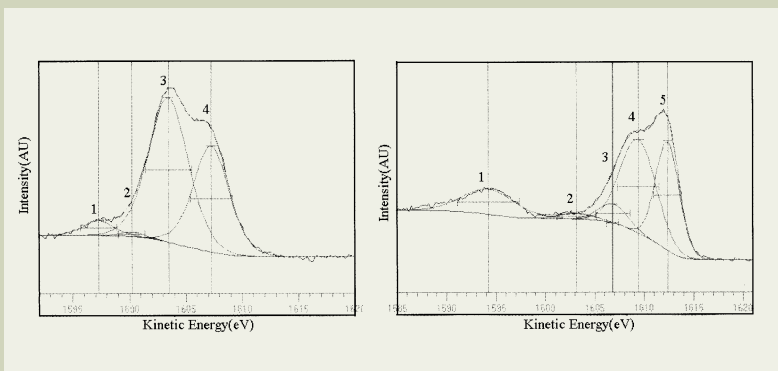


Fig.7 (a). Chemical analysis for the spectra of number 9 depth level. Fig.7 (b). Chemical analysis for the spectra of number 23 depth level.

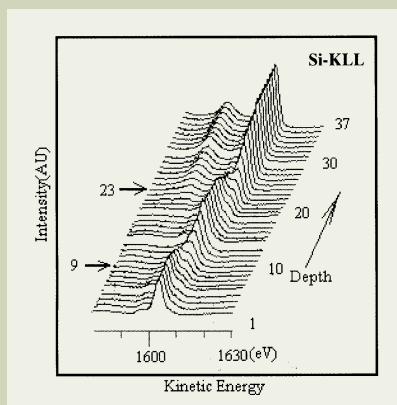


Fig.6. Depth analysis for SiO₂ and SiON_x on the Si substrate.

Table 1: Chemical analysis by the curve fitting method for SiO₂, SiON_x and Si interface.

	Peak No	Peak position (eV)	Peak Intensity (arbitrary)	Half width HWHM (eV)	S-KLL peak assignment
The spectra of number 9 depth level.	1	1597.3	0.054	1.588	SiO ₂
	2	1600.2	0.017	1.179	SiON _x
	3	1603.5	0.556	2.053	SiO ₂
	4	1607.3	0.393	1.859	SiON _x
The spectra of number 23 depth level.	1	1594.3	0.100	3.158	Si-loss-peak
	2	1603.2	0.022	1.984	SiON _x
	3	1606.9	0.074	1.738	Si
	4	1609.4	0.372	2.133	SiON _x
	5	1612.4	0.432	1.408	Si

Miniaturized STM Working Simultaneously in UHV Electron Microscope

— Conductance quantization of suspended gold nanowires —



Kunio Takayanagi, Yukihito Kondo, and Hideaki Ohnishi

ERATO, Japan Science and Technology Corporation (JST)

We have developed a miniaturized scanning tunneling microscope (STM) installed in a newly developed ultrahigh vacuum electron microscope with a field emission electron source. A strand of gold atoms is formed between two gold electrodes of the STM. The gold strands showed quantized conductance in the unit of $2e^2/h$ or multiple of that, as if a individual gold atom strand carries the unit conductance. We also demonstrate structures of gold nanowires, which are 2 nm in thickness, below 1 nm and single atom chain.

Introduction

Since the ultrahigh vacuum (UHV) transmission electron microscope (TEM) was developed in 1969 by Poppa and Heinemann [1], a great deal of efforts have been made by Valdre [2], Venables [3], Stowell [4], Honjo's group [5], Gibson [6], and Yagi [7]. After these efforts, commercial UHV electron microscopes such as JEM-2000FXV [8,9], H2000 [10], and Philips & Gatan [11] have been used for studies of surfaces, interfaces, MBE growth, and catalysis. After appearance of scanning tunneling microscopy (STM) in 1983 [12] and other probe microcopies, several groups [13, 14, 15] have installed STM mechanism into their UHV electron microscope to allow simultaneous TEM-STM and/or REM-STM studies. These works have not given rich results, however.

We re-visited TEM-STM development, since the STM probe can be used as a tool for nano-fabrication and for a nano-probing. In-situ fabrication of nanoscale materials is highly important for the nanotechnology in the 21st century that we are facing. Here, we report the concept of our UHV electron microscope, which enables us to do STM and nano-fabrication under simultaneous TEM observation. As an example of such future amenities, we present here simultaneous measurement of electronic

conductance and structure of a gold nanowire. The nanowires were formed by STM tip or by electron beam fabrication in-situ in an UHV transmission electron microscope developed newly after original design.

Electronic conductance of nanowires is of particular interest because of quantum effect, which appears when length scale of the nanowires is so small as their Fermi wavelengths. Experimental [16, 17] and theoretical studies [18] for the conductance quantization have been done extensively, mostly for gold. The experimental results showed step change of the nanowire conductance with a quantized unit step height of $2e^2/h$ ($= 1/(12.9 \text{ kilohm})$) or the unit step heights, where e is the electron charge and h the Planck constant. Conductance quantization has been reported by several experimental set-ups; STM configuration [19], three-point breaking configuration [20], pinplate configuration [21], and switching electrode [22]. The unit conductance has been detected before rupture of the point contact.

UHV TEM-STM

Figure 1 shows a view of our UHV electron microscope (JEOL JEM-2000VF) equipped with a field emission gun. A preparation chamber at the left-hand side of the microscope column is commercially made, and used for specimen transfer. A chamber at the right-hand side is used for transfer of a home made STM. The specimen and STM join at the goniometer stage.

As shown in a scheme of **Fig. 2**, a mechani-

cally sharpened gold tip was positioned closely to one of gold islands deposited on a thin copper wire. The gold tip can be translated in three dimensions with a shear type piezo-electric-transducer (PZT), as in conventional STM. The gold tip was dipped into the gold island and was pulled slowly. Initially, several structural changes of the contact were observed. Finally, the formation and rupture of an atomic bridge occurred in the receding processes. We observed the processes by high-resolution transmission electron microscope images. The images were recorded on a VTR at every 33 ms by a TV camera. We measured the current passing through the contact, or conductance of the atomic bridge, and recorded it on each frame of the VTR simultaneously with the microscope image. Thus, we knew one-to-one correspondence between the structure and conductance of the nanowire.

We used mostly V_b (bias voltage between the Tip and substrate)=13 mV and measured I_t (current)=1 100 A. The imaging electron current, which crosses the contact area, is of order of picoampere. Therefore, imaging electrons can take only part a few percents of the conduction current, although they might affect a little through plasmon excitation or core electron excitation.

Quantized conductance of gold wire

Experiments run over 300 times showed that gold wires have uniform thicknesses and the number of gold atom rows (or atom sheet)

3-1-2 Musashino, Akishima, Tokyo 196-8558, Japan
E-mail: takayang@materia.titech.ac.jp

decreases one-by-one. Following the one-by-one decrease of the wire thickness, the conductance changed stepwise in the unit of $2e^2/h$, or multiple of that. **Figures 3 and 4** show TEM images and conductance changes of a receding process, respectively. As the number of atomic rows, which are imaged as dark lines in each TEM image, decreases to 6, 5, 4, 3, 1 and 0, the conductance decreases stepwise to 28, 21, 13, 9, 4, and 0. Thus, we have measured many cases. In the result reported previously [23], the wire appeared a single atomic row in TEM images with twice of unit conductance. The bridge was thought to have two atomic rows, which are superposed in the direction of the imaging electron beam. After detailed analysis for the series of images, a single row wire was shown to have the unit conductance, and a double row wire had twice of the unit conductance [23].

A single strand and strands of gold atoms

Here, questions arise about structures of gold nanowires. Because the nanowires we see in Fig. 3 have high surface to volume ratio, and their structure can not always be the same as the bulk structure. In nanometer scale regime, carbon nanotubes [24] are well known examples that present metallic or non-metallic properties depending on their chirality. To study atomic structures of nanowires such as seen in Fig. 3. We performed another experiment to make nanowires by electron beam bombardment on a thin gold film (3 nm thick) as described else-

where [25]. After the electron beam bombardment of $100A/cm^2$ for a prolonged time, the gold film had bored at several positions. Between the neighboring bores, a gold bridge remained. The bridge was thinned further by bombardment to be a nanowire. An electron microscope image in **Fig. 5** shows a 2 nm thick wire (2 nm in width). The wire presents a hexagonal lattice at the central part, while a square lattice at both sides of the wire. Since the hexagonal lattice turned into the square lattice when the wire was imaged at another focus condition, the wire should have both hexagonal and square lattices. The structure model that we finally concluded after nanoprobe diffraction experiments is shown in **Fig. 6**. The wire has cubic lattices (face centered cubic) at its core area and hexagonal lattices over its surface. As we have reported [26], the model nanowire has 30 atomic rows in its cross section: 14 rows at core and 16 rows at the surface. The reason for the hexagonal lattice is the surface energy minimization. The hexagonal surface layer has to accommodate with the cubic layer at the two lateral faces (of the six lateral faces). Detailed analysis of the lattice spacing proved that the hexagonal layer accommodates with the cubic lattices similar to the $\sqrt{3}$ reconstruction of the (001) gold surface. Thus, the hexagonal layer reduces its surface energy and the interface energy to stabilize the wire.

The model wire has [110] atomic rows along the wire axis. Since the [110] axis is the close packed direction in the gold crystal, a single

[110] atomic rows is looked like strands of pearls.

When the wire was thinned further, we often see a four atomic row nanowire [26] as seen in **Fig. 7 (a)**. When a gold wire was in the [100] direction, a single strand of gold atoms was formed, before it broke. **Fig. 7 (b)** shows the [100] strand of gold atoms. This is the longest strand that we have ever made [21]. We can see individual gold atoms in the wire. The spacings between gold atoms, which are measured directly from TEM images, are around 0.4 nm. Such long spacing is a mystery that any theories have ever succeeded to prove.

Summary

In summary, we have demonstrated a strand of gold atoms which was formed free in vacuum and suspended between two electrodes. The gold wires showed quantized conductance in the unit of $2e^2/h$ or multiple of that, as if individual gold atom strand carries the unit conductance. The results presented here come from the development of a new UHV electron microscope which allows us to build an STM at the specimen stage. The UHVTEM-STM has capability of other probe microscopes such as AFM, friction microscope and SNOM. Future development in these directions will contribute much toward the nanoscale science and technology in the 21st century.

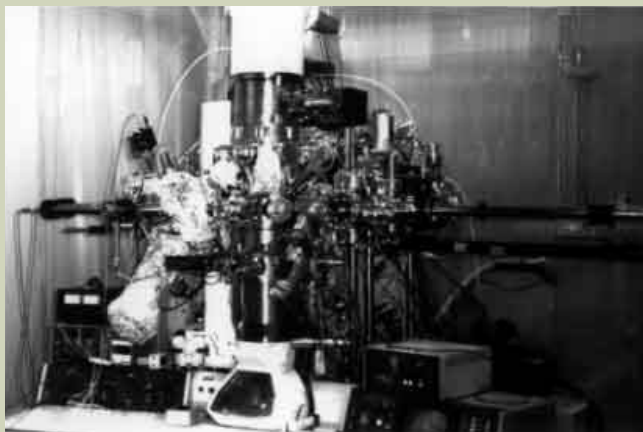


Fig.1. UHV electron microscope for TEM-STM study.

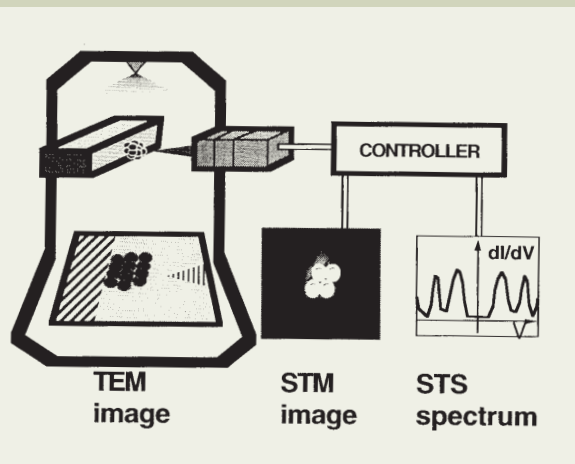


Fig.2. Scheme of TEM-STM operation.

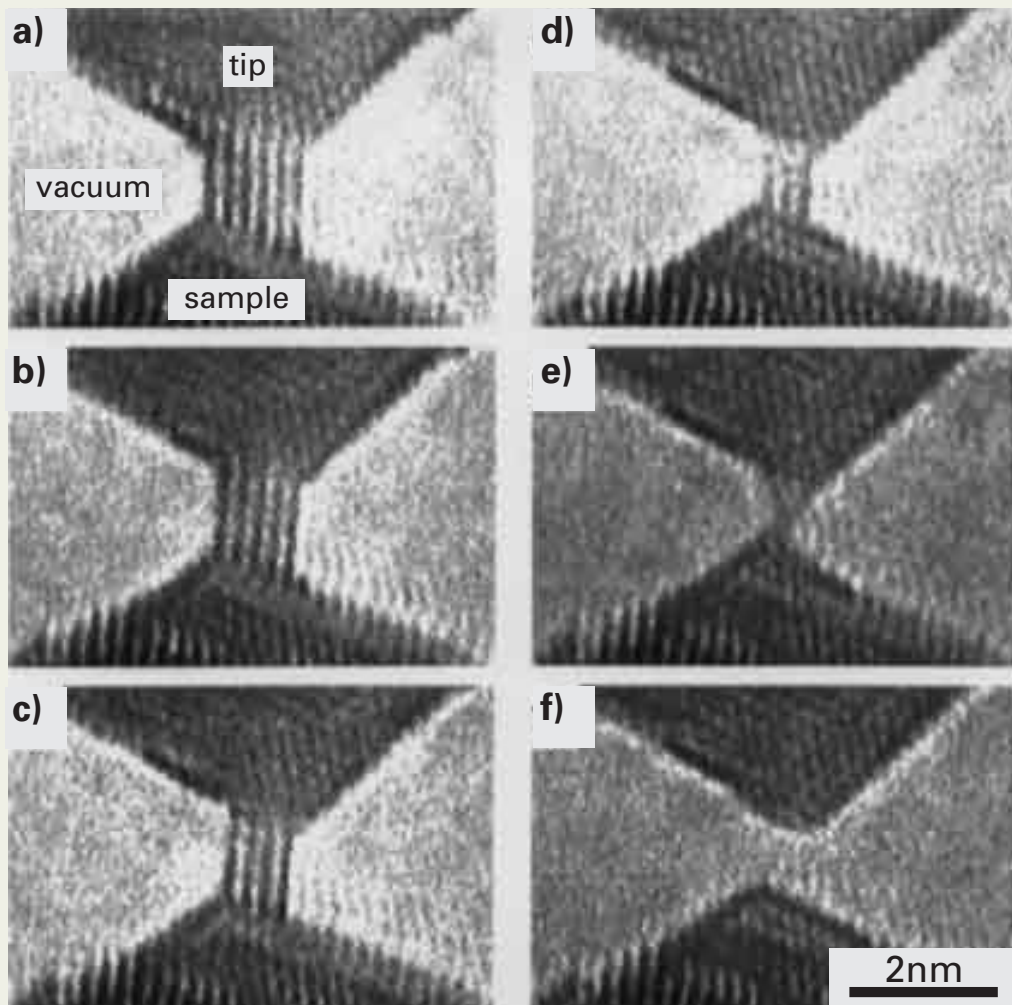


Fig.3. TEM images of gold nanowire which formed between STM tip and substrate. The electrodes are oriented in the [100] direction. Dark lines are the (200) lattice fringes of gold. During in-situ observation of the receding process of the tip from the substrate, the dark lines disappear one-by-one. Note that stepwise change of the conductance in Fig. 4 corresponds to every decrease of the dark lines in Fig. 3.

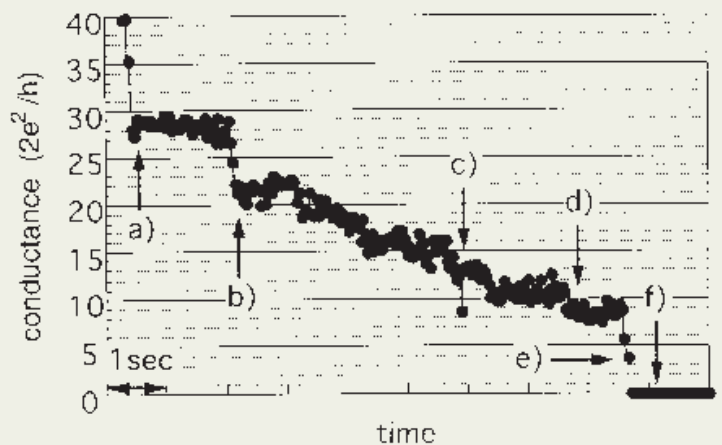


Fig.4. Conductance changes of the nanowires shown in Fig.3. The bias voltage between the electrodes is 13 mV. The current passing the nanowire is given by $13 G A$, where G is measured in the unit of $(k)^{-1}$.

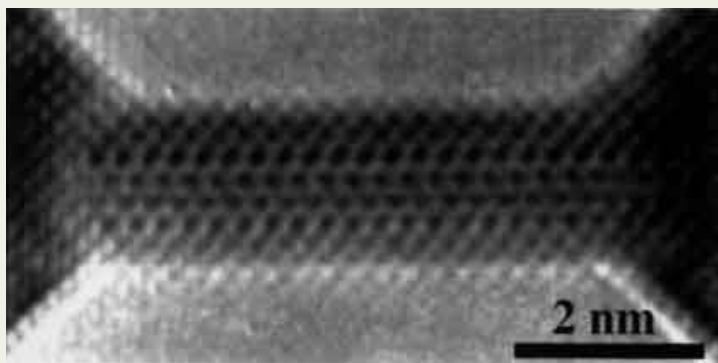


Fig.5. TEM image of gold nanowire 2 nm in width. Note the hexagonal lattice at the center of the wire.

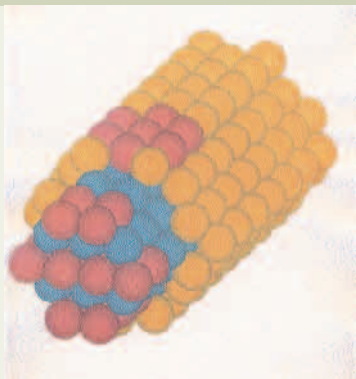


Fig.6. Model structure of the gold nanowire in Fig.5.

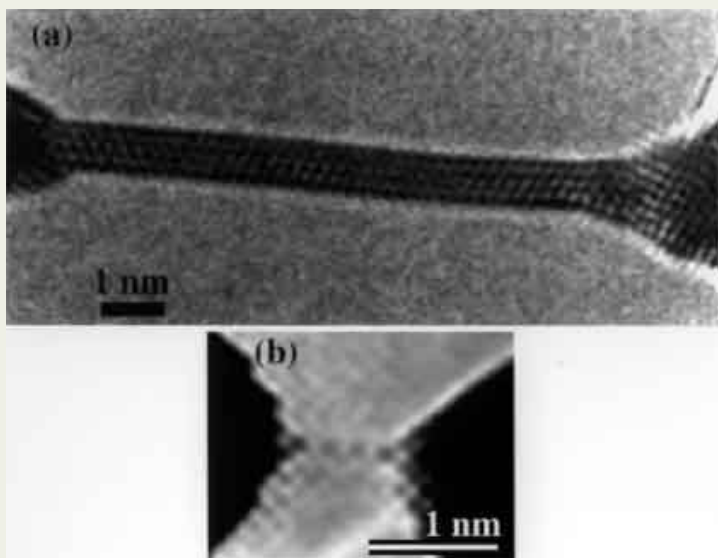


Fig.7. (a) TEM image of gold nanowire. Note that 4 strands of gold atoms are seen as dark dotted lines within its diameter. (b) TEM image of a single strand of gold atoms. Note that 4 dark dots (gold atoms) make the bridge. The four atoms are suspended in vacuum.

References

1. Poppa H.: *J. Vac. Sci. Technol.*, **2**, 42 (1965).
2. Valdre U., Robinson E. A., Pashley D. W., Stowell M. J. and Law T. J.: *J. Phys. E*, **3**, 501 (1970).
3. Venables J. A.: *Ultramicroscopy*, **7**, 81 (1981).
4. Stowell M. J.: *Thin Solid Film*, **12**, 341 (1972).
5. Takayanagi K., Yagi K., Kobayashi K. and Honjo G.: *J. Phys. E*, **11**, 441 (1978).
6. Gibson J. M., McDonald M. L. and Unterwald F. C.: *Phys. Rev.*, **55**, 1765 (1985).
7. Yagi K.: *Surface Science Reports*, **17**, 305 (1993).
8. Takayanagi K., Tanishiro Y., Kobayashi K., Akiyama K. and Yagi K.: *Jpn. J. Appl. Phys.*, **26**, L957 (1987).
9. Kondo Y., Ohi K., Ishibashi Y., Hirano H., Harada Y., Takayanagi K., Tanishiro Y., Kobayashi K. and Yagi K.: *Ultramicroscopy*, **35**, 111 (1991).
10. Xu P., Dunn D., Zhang J. P., and Marks L. D.: *Surf. Sci. Lett.*, **285**, L479 (1993).
11. Swann P. R., Jones J. S., Krivanek O. L., Smith D. J., Venables J. A. and Cowley J. M.: *Proc. 45th Ann. Meeting of EMSA*, p136 (1987).
12. Binnig G., Rohrer H., Gerber C. and Weibel E.: *Phys. Rev. Lett.*, **49**, 57 (1982).
13. Lutwyche M. I. and Wada Y.: *Appl. Phys. Lett.*, **66**, 2807 (1994).
14. Spence J. C. H.: *Ultramicroscopy*, **25**, 165 (1988).
15. Iwatsuki M., Murooka K., Kitamura S., Takayanagi K. and Harada Y.: *J. Electron Microsc.*, **40**, 48 (1991).
16. Costa-Kramer J. L., Garcia N., Garcia-Mochales P., Serena P. A., Marques M. I. and Correia A.: *Phys. Rev. B*, **55**, 5416 (1997).
17. Olesen L., Laegsgaard E., Stensgaard I. and Besenbacher F.: *Phys. Rev. Lett.*, **72**, 2251 (1994).
18. Sorensen M. R., Brandbyge M. and Jacobsen K. W.: *Phys. Rev. B*, **57**, 3283 (1998).
19. Agrait N., Rodrigo J. G. and Vieira S.: *Phys. Rev. B*, **47**, 12345 (1993).
20. Muller C. J., Krans J. M., Todorov T. N. and Reed M. A.: *Phys. Rev. B*, **53**, 1022(1996).
21. Landman U., Luedtke W. D., Salisbury B. E. and Whetten R. L.: *Phys. Rev. Lett.*, **77**, 1362 (1996).
22. Costa-Kramer J. L., Garcia N., Garcia-Mochales P. and Serena P. A.: *Surf. Sci.*, **342**, L1144 (1995).
23. Ohnishi H., Kondo Y. and Takayanagi K.: *Nature*, **395**, 780 (1998).
24. Iijima S.: *Nature*, **354**, 56 (1991)
25. Niwase K., Siegle W., Phillipp F. and Seeger A.: *Philos. Mag. Lett.*, **74**, 167 (1996).
26. Kondo Y. and Takayanagi K.: *Phys. Rev. Lett.*, **79**, 3455 (1997).

High-Resolution Electron-Beam Lithography and Its Application to MOS Devices



Yukinori Ochiai

Silicon Systems Research Laboratories, NEC Corporation

A point electron-beam lithography system using a thermal field emitter (TFE) allows us to use a nanometer-level fine electron beam to investigate nano-fabrication techniques and minute devices. We developed an organic negative resist, called calixarene, which has low molecular weight of 972 and almost monodispersity. This resist shows a high resolution of about 10 nm when it is exposed to an electron-beam system of 50 kV using TFE. The newly developed resist has been applied in order to fabricate an EJ-MOSFET (electrically variable shallow junction metal-oxide-semiconductor field effect transistor). A 14-nm-gate-length EJ-MOSFET was fabricated by using a calixarene resist and an electron-beam exposure system, and showed MOS device performance.

1. Introduction

For the past 30 years, the packing density of LSIs (Large Scale Integration) has been increasing and by using optical lithography such as i-line and KrF excimer laser stepper, a minimum feature size of 0.18 μm is under production. The performance of devices such as clock speed and consumption power can be improved by reducing its feature size. Regarding the future MOS LSIs, devices with a minimum feature size of less than 0.1 μm will be investigated because the feasibility and performance of such MOS devices with small gate lengths are unclear [1]. Yet at moment, a lithography system for mass production is not available for sub-0.1 μm . Therefore, Gaussian or point electron-beam lithography system is the only tool used for the deep sub 0.1 μm region [2-4]. The resolution of a lithographic pattern is not only governed by the resolution of the lithographic tool itself but also by the resolution of the resist. In this report, the development of a high-resolution resist for nanolithography and its application of minute MOS device fabrication is presented.

2. High-resolution resist; calixarene

PMMA is a well-known high-resolution positive resist that has been used for nanofabrication and for testing the feasibility of electron beam lithography machines [5]. When using electron beam lithography to reduce an exposed area so that a high throughput is obtained, a negative tone resist is useful, especially for the gate patterning in MOS devices.

We have investigated a mechanism for resist resolution and have developed a new type of resist, called calixarene [6]. We found that the resolution of an organic negative resist depends on the molecular size of its composed material of resist by using polystyrene resist [7]. The average molecular weight of a negative tone resist ranges from several thousands to several ten thousands and its molecular size or diameter ranges from a few nanometers to several tens nanometers. These resists show a resolution of only a few tens nm [8]. It is important to obtain low molecular weight resin of about 1000 or less for the high resolution. The roughness of the resist pattern is affected not only by the molecular size of the resist but also by dispersion [9]. Calixarene used in this experiment has a low molecular weight of about 1000 and almost monodispersity. The

diameter of the molecule is about 1 nm.

Calixarene[10], which is a general term for specific cyclic phenol resins, is a cyclic oligomer. The calixarene resists used in this experiment consist of 6-phenol and have a molecular diameter of 1nm [11]. The molecule shown in **Fig.1 (a)** is a calixarene derivative, hexaacetate *p*-methylcalix[6]arene (MC6AOAc) that has a molecular weight of 972, while the molecule shown in **Fig. 1 (b)** is a calixarene derivative, hexa-chloromethoxyhexa-methoxycalix[6]arene (CMC6AOMe) that has a molecular weight of 996. Most calixarene derivatives have poor solubility in organic solvents, but these calixarene molecules are soluble in organic solvents such as *o*-dichlorobenzene and they have a high heat resistivity up to 590 K [12].

Therefore, films of calixarene are made easily by using a spin coating method similar to that used in conventional resist processes. We found that these calixarene films work well as negative electron-beam resists and that they show ultrahigh resolution and high durability under halide plasma etching.

The electron beam exposure characteristics of these calixarene films are shown in **Fig. 2**. The electron beam lithography system used is JBX-5FE/6000FS which are produced by JEOL Ltd [13]. By using a thermal field emit-

ter (TFE), the beam diameter is 5 nm at an acceleration voltage of 50 kV. We spin coated 1weight % of a calixarene solution on a Si wafer at 3000 rpm for 30 s to prepare a 30-nm-thick film. For MC6AOAc, the threshold sensitivity was about 0.8 mC/cm² and the practical sensitivity was about 7 mC/cm², which is almost 20 times higher than that for PMMA and almost 100 times higher than that for a SAL601 chemically amplified negative resist. The sensitivity of the chloromethylated calixarene CMC6AOMe is about ten times higher than that of MC6AOAc. Substituting Cl atoms in the methyl groups generally improves the sensitivity because the Cl bonds easily decom-

pose when the C-Cl bonding energy is low. Activated Cl can affect Cl bonds at other sites and it can reduce their bonding energy. Their Cl bonds can then be broken by a low energy deposition. The resist contrast is about 1.6 for each calixarene resist.

Line and dot patterns using a calixarene resist are shown in Fig. 3 and Fig. 4. The resist line pattern was made on a thin Ge film deposited on a silicon wafer. The resist dot pattern was made on a silicon wafer. Both line width and dot diameter are 15 nm. By using SAL601 which is a chemically amplified negative resist, we achieved a minimum line width of 30 nm. Therefore, calixarene resist provides

us with very fine line and dot patterns.

3. Fabrication of 14-nm EJ-MOS devices

To fabricate a small gate length MOSFET, such as sub-0.1 μm , suppression of short-channel effects is important. To avoid any problems, it is necessary to make a shallow junction for the source and drain region. In this experiment, we propose an electrically variable shallow junction metal oxide semiconductor field effect transistor (EJ-MOSFET) [14, 15]. Figure 5 is a schematic cross section of an EJ-MOSFET. Shallow junctions are usually made by thermal doping or ion implantation, but

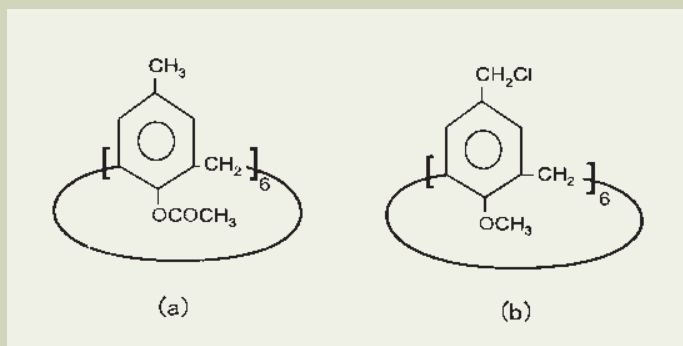


Fig.1. Chemical structure of calixarene: (a) MC6AOAc, (b) CMC6AOMe. The molecular weights are (a) 972 and (b) 996, respectively. The molecular size is about 1 nm.

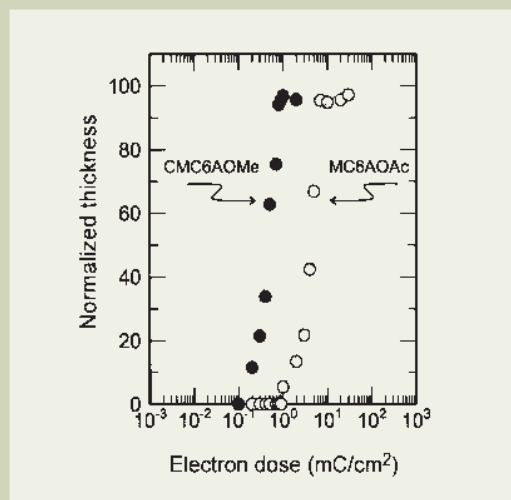


Fig.2. The exposure characteristics of calixarenes. The electron beam used is 50 kV and the diameter of the point beam is 5 nm.

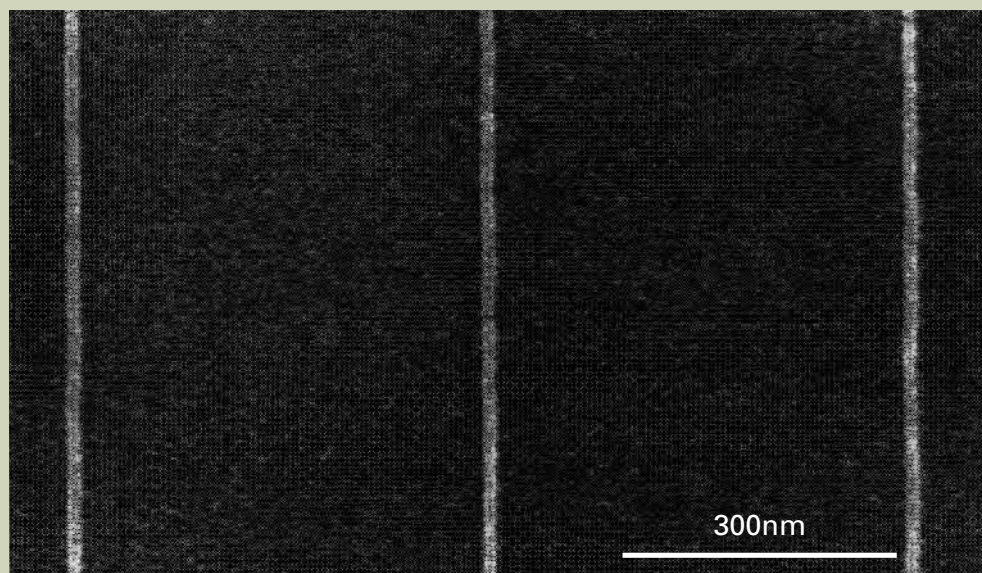


Fig.3. Line pattern made by calixarene, MC6AOAc, on a Ge film deposited on a silicon wafer. The electron doses is 60 nC/cm.

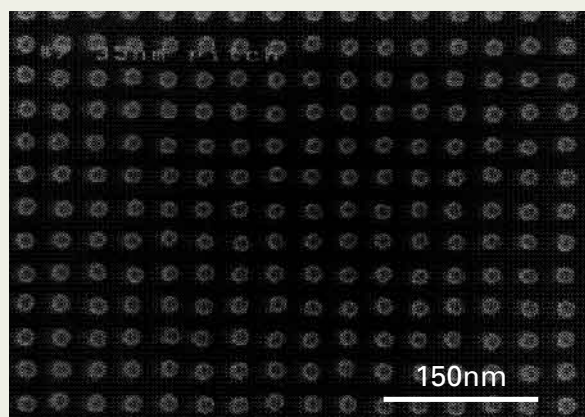
with regard to the EJ-MOSFET, the shallow junction is made by using an electrically induced inversion layer. The gate oxide thickness is 5 nm which is grown through thermal oxidation. The 40-nm-thick poly-Si lower gate (this is an ordinary gate) is defined by EB-direct writing onto a calixarene resist and by dry etching with CF₄ gas. The other part is defined by optical lithography. The poly-Si gate is covered by a 20-nm thick intergate oxide made by chemical vapor deposition (CVD) and the Al/Au upper gate is deposited by thermal evaporation. This upper gate induced an inversion layer which acts as a shallow junction. The junction depth is about

4.5 nm. **Figure 6** shows a cross sectional transmission electron microscope (TEM) image of a fabricated EJ-MOSFET, which has a poly-Si gate length of 14-nm embedded in the gate oxide and intergate oxide [16]. **Figure 7** shows the drain current versus the drain voltage as a function of the gate voltage for EJ-MOSFET at 300 K. The gate width is 10 μm. A short channel effect gradually occurs under a gate length of 30 nm and there is no saturation characteristics of drain current in the 14-nm gate EJ-MOSFET. However, the drain current is modulated by changing the gate voltage, which means that MOSFET with a short gate length, such as 14-nm, could per-

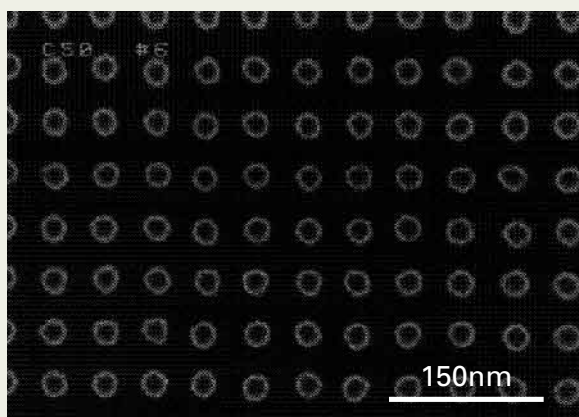
form if the short channel effect is suppressed using, for example, a thin gate oxide, a highly doped substrate, and a shallow junction.

4. Newly developed 100-kV electron beam system

The size of silicon wafers increases with increasing chip size and device density so that high productivity is obtained and production cost is reduced. Currently, 8-inch wafers are used in both R&D and mass production, but in the near future, 12-inch wafers will be introduced to the semiconductor industry. As we have already mentioned, research in sub-0.1 μm device continues intensively. In order to obtain



(a) MC6AOAc d = 15nm, period = 35nm, t = 40nm



(b) CMC6AOMe d = 25nm, period = 50nm, t = 40nm

Fig.4. Dot pattern made by calixarene. The electron dose is 1 × 10⁵ electrons/dot.

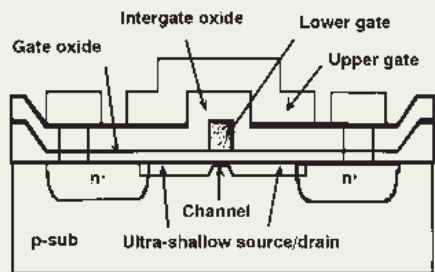


Fig.5. Cross sectional device structure of an EJ-MOSFET. The calixarene resist is used to delineate a polysilicon gate.

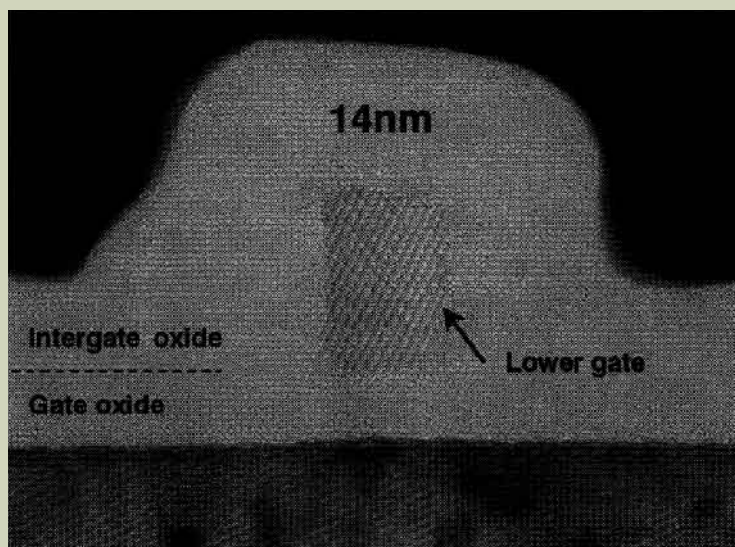


Fig.6. Cross sectional TEM image of an EJ-MOSFET. The 14-nm-polysilicon gate is well defined by using calixarene and dry etching.

high throughput, chemically amplified resists are commonly used in both optical and electron beam lithography. Therefore, a high-resolution electron-beam lithography system requires a chemically amplified resist and large wafers for next generation process. Recently, a new point electron-beam system, known as JBX-9300FS, has been developed (Fig. 8) [17]. This system has an acceleration voltage of 100 kV which allows high resolution and high aspect ratio lithography for a large deflection field. The minimum beam diameter of less than 4 nm is obtained at 500 m field, at a beam current of 100pA, and an acceleration voltage of 100 kV. The maximum

deflection clock is over 25 MHz. An 8-inch wafer is available for full exposure and a 12-inch wafer is loadable. The system has an automatic wafer cassette loader which can be used with an automatic coater and developer. This system is useful for the research of high-performance Si-MOS devices and LSIs.

5. Summary

High-resolution nanolithography using a newly developed electron-beam resist, called calixarene, and its application to device fabrication have been shown. We found that a calixarene negative resist has a high-resolution of 10 nm when it is combined with a 50-kV point

electron-beam lithography system using TFE. The resist has a low molecular weight of about 1000 and a molecular diameter of 1 nm. This negative resist almost has the highest resolution when it is compared with other negative resists reported elsewhere. By using this resist, we developed a 14-nm-gate length EJ-MOSFET for gate patterning and showed MOS device performance. This device has the minimum gate length on a silicon wafer. The high resolution resist and point electron beam-lithography system allows us to use nano-fabrication techniques in a conventional device process.

References

- Ochiai Y., Manako S., Samukawa S., Takeuchi K. and Yamamoto T.: *Microelectronic Engineering*, **30**, 415 (1996).
- Beaumont S. P., Bower P. G., Tamamura T. and Wilkinson C. D. W.: *Appl. Phys. Lett.*, **38**, 436 (1981).
- Craighead H. G., Howard R. E., Jackel L. D. and Mankiewich P. M.: *Appl. Phys. Lett.*, **42**, 38 (1983).
- Ochiai Y., Baba M., Watanabe H. and Matsui S.: *Jpn. J. Appl. Phys.*, **30**, 3266 (1991).
- Broers A. N., Harper J. M. E. and Molzen W. W.: *Appl. Phys. Lett.*, **33**, 392 (1987).
- Fujita J., Ohnishi Y., Ochiai Y. and Matsui S.: *Appl. Phys. Lett.*, **68**, 1297 (1996).
- Manako S., Fujita J., Tanigaki K., Ochiai Y. and Nomura E.: *Jpn. J. Appl. Phys.*, **37**, 6785 (1998).
- Manako S., Ochiai Y., Fujita J., Samoto N. and Matsui S.: *Jpn. J. Appl. Phys.*, **33**, 6993 (1994).
- Yoshimura T., Shiraishi H., Yamamoto J., Terasawa T. and Okazaki S.: *Appl. Phys. Lett.*, **68**, 1799 (1996).
- Gutsche C. D.: *Calixarene*, Royal Soc. Chem., Cambridge, 1989.
- Fujita J., Ohnishi Y., Ochiai Y., Nomura E. and Matsui S.: *J. Vac. Sci. Technol.*, **14**, 4272 (1996).
- Wamme N. and Ohnishi Y.: *Proc. Am. Chem. Soc. PMSE* **67**, p451 (1992).
- Nakazawa H., Takemura H., Isobe M., Nakagawa Y., Hassel Shearer M. and Thompson W.: *J. Vac. Sci. Technol.*, **B6**, 2019 (1988).
- Sakamoto T., Kawaura H., Baba T., Fujita J. and Ochiai Y.: *J. Vac. Sci. Technol.*, **15**, 2806 (1997).
- Kawaura H., Sakamoto T., Baba T., Ochiai Y., Fujita J., Matsui S. and Sone J.: *IEEE Elect. Dev. Lett.*, **19**, 74 (1998).
- Kawaura H., Sakamoto T., Ochiai Y., Fujita J. and Baba T.: *Ext. Abst. Int. Conf. Solid State Devices and Materials, Hamamatsu*, p572 (1997).
- Ochiai Y., Ogura T. and Mogami T.: *Mico- and Nano-Engineering 98 (MNE) Leuven, Belgium, 1998*. Paper will appear in *Microcircuit Eng.* 1999.

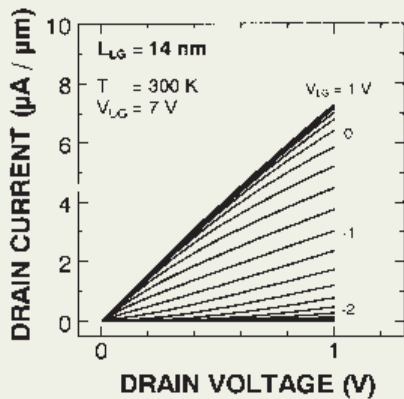


Fig.7. Drain current vs drain voltage (I_D - V_D) characteristics of EJ-MOSFET with a lower gate length (L_{LG}) of 14 nm at room temperature. The upper gate voltage (V_{UG}) was fixed at 7 V and the lower gate voltage (V_{LG}) was biased from -3 to 1 V in 0.2 V steps.

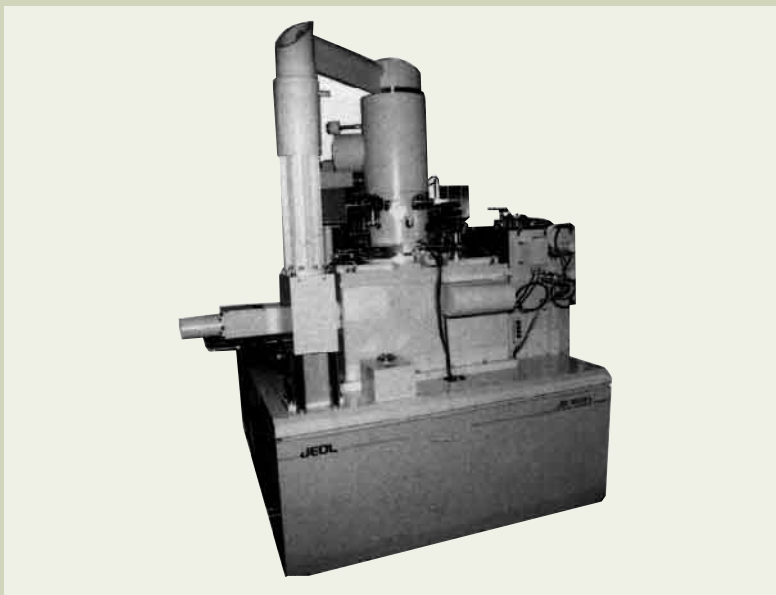


Fig.8. Photograph of a newly developed 100-kV electron-beam lithography system, JBX-9300FS.

Development of Electron Optical Technology for JEOL's Electron Probe Instruments



Akishige Ono

Engineering Management Division, JEOL Ltd.

Introduction

From 1948 to 1959, fundamental scanning electron microscopes (SEM) were investigated at Oatley's laboratory in Cambridge University [1, 2]. In 1965, the first SEM was commercialized by Stewart who was a graduate of Oatley's laboratory and a member of Cambridge Instruments. JEOL, which was developing a commercial SEM at the same time, announced and exhibited its first SEM, the JSM-1, at the International Congress on Electron Microscopy held in Kyoto (1966).

Fig. 1 shows chronological development of JEOL SEMs from the JSM-1 to the present models. It is interesting to note that the number of the multi-purpose large-sized SEMs reached its peak with the JSM-35 and the JSM-840 between the late 1970's and mid 1980's, then decreased gradually. The number of FESEMs (field emission SEM) — SEMs fitted with a field emission electron gun (FE gun) — has increased largely in the 1990's and the number of medium-sized SEMs placed in the market in the 1980's increased drastically. In the late 1990's, the market has been divided completely into two categories, one is high-resolution FESEMs and the other low-priced medium-sized SEMs. Although not shown in the figure, dedicated SEMs for the semiconductor industry developed in the 1980's form another category in the 1990's.

Here, we will describe how the electron optical technology of JEOL's electron probe instruments has evolved, by focusing mainly on the SEM product line.

Investigation of Resolution

High-brightness electron guns and objective lenses with small aberration coefficients have been developed to improve the resolution of SEMs.

High-brightness electron gun

A thermal electron gun has been used for the conventional SEM. Though an FE gun developed by Crewe [3] drew attention as an electron gun for a high resolution SEM because of its brightness of 1000 times higher than the conventional one, it took a long time to be commercialized because ultrahigh vacuum was necessary. In 1974, an FESEM, the JFSM-30, was commercialized, however it was expensive and not many were sold. Consequently, it went out of production after a very short life. It was in 1987 that a new FESEM was put on the market once again. Meanwhile, the S800 released by Hitachi Ltd. in 1982 sold well, and made a great contribution to the scanning electron microscopy from the viewpoint of practical use of the FESEM.

The FESEM, in addition to its high resolution, brought high image quality and extremely high resolution at low accelerating voltages as compared to conventional SEMs with a thermal electron gun. As the FESEM had great advantages to observe true specimen surfaces and uncoated insulating materials, it increased its market in the late 1980's. Around this time in the semiconductor industry, the pattern size was being reduced to less than 1 μm due to large integration of devices. The FESEM became an indispensable tool for process

inspection and earned wide acceptance in the semiconductor application.

Objective lenses with small aberration coefficients

Conventional objective lenses have been used for a long time in electron probe instruments. However, their aberration coefficients cannot be reduced so much even if the working distance is decreased. Also, reducing the working distance affects the collection efficiency of secondary electrons. On the other hand, the so-called in-lens type objective lens, which was developed as an attachment for transmission electron microscopes [4] in which the specimen is placed in the magnetic field, has one-tenth the aberration coefficients of a conventional objective lens. In fact, a resolution better than 0.7 nm was obtained with the JSM-890, an in-lens FESEM commercialized in 1987. However, the in-lens type objective lens imposed a limit on the maximum size of the specimen, and in practice the size of the specimen had to be no more than several mm.

To overcome this, a so-called semi-in-lens type objective lens based on a snorkel lens proposed by Mulvey [5] was developed. In this design the principal plane of the objective lens is formed below the objective lens by allowing a strong magnetic field to be intensely leaked under the pole piece. As a result the aberration coefficients can be reduced. In order to collect the secondary electrons which are directed back up the beam axis, a detector is positioned just above the lens. Therefore, a specimen can be placed just below the objective lens, enabling even large specimens to be observed

with high resolution. A semi-in-lens SEM, the JSM-6320F developed in 1994, guaranteed 2.5 nm resolution at an accelerating voltage of 1 kV [6].

Fig. 2 shows historic models with various electron optics.

Analytical SEM, EPMA and Auger Microprobe

Once the SEM was put to practical use, demands arose to enable it to be used not only for observing images, but also for investigating the physical and chemical properties of specimens by utilizing the various electrons, photons, and so on, emitted from the specimen. As a result, the SEM came to be fitted with an X-ray spectrometer. The first SEM that was developed for this purpose was the JSM-U3 (1969). The philosophy of placing importance on the functions of the SEM as an analyzing instrument was carried over to subsequent multi-purpose large-sized SEMs, and the number of SEMs sold increased.

In the case of a SEM, unlike an EPMA (electron probe microanalyzer), qualitative analyses are carried out mainly with high-reso-

lution observation of surface topography. Therefore, the principal method employed recently is an energy dispersive X-ray spectrometer because it is easier to use, requires less beam current and can be mounted with few restrictions on the specimen chamber.

The theory of EPMA analysis was published by Castaing *et al.* in 1949 [7]. Subsequently, a scanning type EPMA was developed by Cosslett *et al.* in 1956 [8]. JEOL had already put the JXA-1 into production (1960) ahead of a SEM. With the EPMA, emphasis is placed on X-ray analysis over a minute area, hence it is necessary to obtain a sufficiently small probe diameter even when the probe current is increased. On the other hand, an optical microscope is necessary to align a specimen height so as to satisfy the analytical condition of a wavelength dispersive spectrometer properly. Taking into account these requirements, an electron optical system with different characteristics as compared with a conventional SEM was required. A unique electron optical system was developed for the JXA-733 with the objective lens which incorporated an optical microscope, with the high take-off angle of the

X-ray spectrometer maintained (1978). As the result, a probe diameter of 1 μm was obtained with a probe current of 1 μA and an accelerating voltage of 10 kV.

Because surface-sensitive measurements require an ultrahigh-vacuum specimen chamber in Auger analysis, a unique instrument, the JAMP-3, was developed independently of a SEM (1972). In the case of Auger microprobe, a fine electron probe should be obtained with a large probe current as in the case of an EPMA. In addition, a high-brightness electron gun is required as the analysis is mainly carried out at comparatively low accelerating voltage. For this purpose, an FE gun was employed for the JAMP-7800F (1995). A spatial resolution of 10 nm was obtained with a probe current as large as 10 nA at 25 kV, by combining a T-FE gun (temperature FE gun) and electric-magnetic-field overlapped condenser lens [9].

Dedicated SEM for Semiconductor

With the increased integration of semiconductor devices, shrinking pattern features have exceeded the resolution of an optical micro-

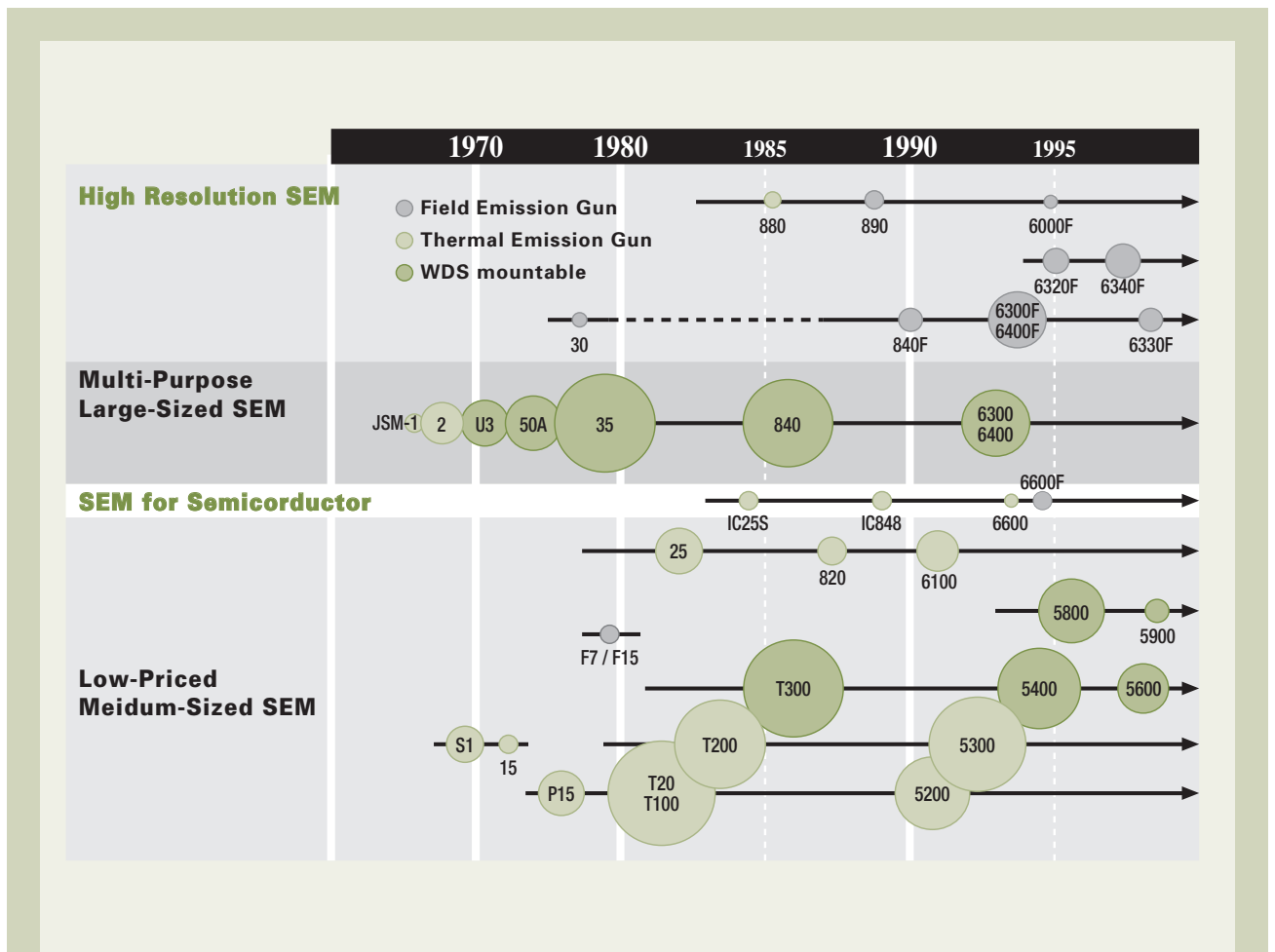


Fig.1 Chronological development of JEOL SEM's. The area of each circle indicates the approximate number of instruments produced up to March 1999.

scope and inspection now must be carried out with a SEM. From such a background, the JEPAS-1000, an electron beam line width measuring system, was developed based on the JSM-25 (1982). The JWS-7500 series introduced in the 1990's is a wafer inspection SEM to observe and analyze defects and foreign dust particles on a wafer. It features high resolution observation of a highly tilted wafer at low accelerating voltage. To realize this capability, a low-aberration objective lens with a small conical angle was developed [10] and a very stable T-FE gun was employed. Thus, wafers are now routinely observed obliquely at 60-degree tilted position with high resolution.

In the JFS-9800, a dual beam FIB (focused ion beam) instrument, the ion optical column was added to the JWS-7500. The ion optical column and the electron optical column were arranged at a 60 degree angle between the beam axes [11]. With this instrument, foreign particles or defects buried in a lower level of the wafer were able to be cut with the FIB and

the exposed cross section to be observed with a SEM or a SIM (scanning ion microscope), and hence defect inspection has advanced one more step.

Summary

Development of the electron optical technology for electron probe instruments of JEOL was reviewed by focusing mainly on the SEM, over the last 40 years or so. Fundamental technologies that support individual instruments cover an extremely wide range of fields. It should be added that those described here are only a part.

References

1. Nixon W.: *Scanning Electron Microscopy* / 1968, 57 (1968).
2. McMullan D.: *J. Microscopy*, **139**, 129 (1985).
3. Crewe A. V., Eggenberger D. N., Wall J. and Welter L. M.: *Rev. Sci. Instr.*, **39**, 576 (1968).
4. Koike H., Ueno K. and Watanabe M.:

- Proc. 8th Int. Congr. Electron Microsc., Grenoble, Vol.1*, p241 (1970).
5. Mulvey T.: *Scanning Electron Microscopy*, **1**, 44 (1974).
6. Nakagawa S.: *JEOL News*, **31E**, 36 (1994).
7. Castaing R. and Guiner A.: *Proc. 1st Int. Congr. Electron Microscopy, Delft*, p60 (1949).
8. Cosslett W. E. and Duncumb P.: *Nature*, **177**, 1172 (1956).
9. Yamada T., Kudo M., Ando Y., Sekine T. and Sakai Y.: *JEOL News*, **32E**, 50 (1996).
10. Takashima S.: *JEOL News*, **31E**, 35 (1994).
11. Sekine T. and Sakata T.: *JEOL News*, **33E**, 44 (1998).



a. JSM-1 (first SEM).



b. JFSM-30 (first FESEM).



c. JSM-890 (first in-lens FESEM).



d. JSM-6320F (first semi-in-lens FESEM).

Fig.2. Outer views of historic SEM models with characteristic electron optics.

Observation of Protein Structures through an Electron Beam



Yoshinori Fujiyoshi

Department of Biophysics, Faculty of Science, Kyoto University

I. Introduction

Electron microscopy plays an important role for structural studies in various fields of basic sciences such as physics, chemistry, and biology, because it can provide structural information from a very small region of a specimen and especially because it does not require a periodic structure of the specimen. The high sensitivity of the electron microscope is due to the strong interaction of electrons with all matter. This strong interaction, however, results in two inevitable problems for biological specimens, namely damage to the specimen by the irradiating electrons and the necessity of a vacuum for the electron beam.

In 1973, when I began to work in electron microscopy, the performance of electron microscopes was generally considered to be sufficient to yield atomic resolution for most inorganic materials which are stable in the electron beam. However, it was uncertain whether electron microscopy was actually suitable for the direct visualization of atoms because irradiation with high energy electrons was thought to lead to vibrations of the atoms in the specimen and thus would cause images recorded by an electron microscope to be blurred. One pessimistic theory had even argued that multiple scattering of the electrons by the specimen (dynamical scattering) would distort the electron microscopic images to a degree that it would prevent interpretation of the images. Therefore, I still remember clearly the knee-shaking sensation when I saw our initial successful micrograph of the molecular structure of chlorinated copper phthalocyanine. This image clearly resolved for the first time individual atoms (**Fig. 1**) [1] and convinced me of the potential of electron microscopy for structure analysis at atomic resolution. We, however, encountered severe difficulties, when

we subsequently tried to use electron microscopy for the analysis of biological molecules. Organic molecules, especially biological ones appeared to be too sensitive to withstand the electron beam without significant damage even for a very short time, although we had developed a minimal dose imaging system (MDS) to record high-resolution

images without no excess illumination of electrons [2].

In the case of biological molecules, the resolution of an image is not limited by the resolution of the microscope, which nowadays achieves a resolution of better than 0.2 nm, but by the damage of the specimen caused by the electron beam. Because it was found that this

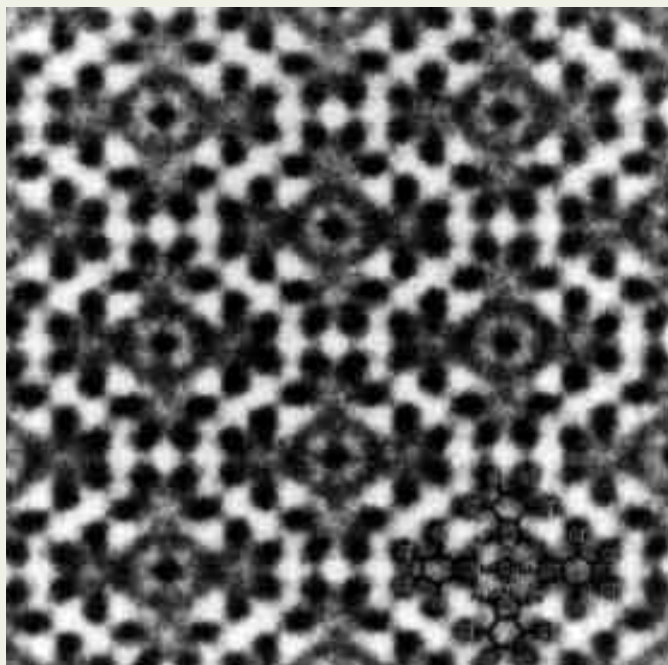


Fig.1. Electron microscopical image of chlorinated copper phthalocyanine crystal. The chemical structure of this compound is superimposed on the high-resolution image. This micrograph was the first prove that electron microscopy is capable to visualize individual atoms in an organic molecule.

irradiation damage can be significantly reduced by lowering the temperature of the specimen and because we wanted to realize electron microscopic structure analysis of proteins to a resolution of 0.3 nm or better, we set out to develop an electron cryo-microscope equipped with a specimen stage cooled by liquid helium as a three years project from 1983. We developed a superfluid helium stage to be built into a conventional transmission electron microscope in 1986 by working hard together with Y. Aoki (JEOL).

An electron microscopic image yields only projection (2D) information. Therefore, to produce a complete 3D density map of a protein based on electron crystallography, many images of untilted and tilted specimens must be recorded, processed, and combined. This approach was used for the first time by Henderson and Unwin (1975) who determined the 3D structure of bacteriorhodopsin (bR) to a resolution of 0.7 nm [3]. After publication of this 0.7 nm map, another 15 years were needed for further development of the methodology for electron crystallographic structure determination before Henderson and co-workers could present the structure of bR at a resolution of 0.35 nm [4].

Another example for the successful determination of an atomic structure by electron crystallography is the plant light-harvesting complex II (LHC-II). The atomic model for this membrane protein was published in 1994 by Kuhlbrandt *et al.* [5]. So far, only these two membrane proteins, bR and LHC-II, have been analysed to atomic resolution by high-resolution electron microscopy (Tubulin structure which is a soluble protein was also analysed by K. Downing and co-workers [6]). However, many more membrane proteins have already been crystallized in two dimensions and the 2D crystals of several of these proteins will eventually allow determination of their atomic structure by electron crystallography.

Because bR forms very stable and well-ordered 2D crystals *in situ*, the purple membranes in the plasmamembrane of *Halobacterium salinarum*, this membrane protein has proven an ideal specimen for electron crystallographic structure determination and thus the progress of this technique is closely linked to the study of the structure of bR. In this review I will, therefore, primarily refer to bR as an example to discuss the current state and the future prospects of electron crystallography.

II. High-Resolution Electron Cryo-Microscopy

The mechanism of radiation damage of an organic molecule is thought to be a two step process. First, deposition of energy on the specimen by inelastic scattering events causes breakage of chemical bonds and subsequently the produced radicals, ions and/or molecular fragments diffuse away, leading to a complete collapse of the initial structure. After many attempts to find solutions to overcome this problem, only cooling of the specimen appears to reduce the effects of radiation damage by limiting the diffusion of the newly formed components. The irradiation damage to both tRNA and catalase crystals was found to be reduced to about 1/10 and 1/20 of the value at

room temperature when the specimen was cooled below 20 K and 8 K, respectively.

Based on these measurements, we decided to develop an electron cryo-microscope equipped with a specimen stage cooled by liquid helium. However, mechanical vibrations caused by the boiling of the coolant, as well as specimen drift induced by temperature changes in the specimen stage, presented difficulties which had to be overcome in the design of a high-resolution electron cryo-microscope. We attribute our success of earlier development of a superfluid helium stage to the guidance of T. Mizusaki (Kyoto University) as well as many trials of the stage design. A paper describing details of design and construction of that stage which achieved a resolution of 0.26 nm was published in 1991 [7]. An instrument yielding a resolution better than 0.26 nm would, however, be highly beneficial for structure analysis of biological molecules at atomic resolution, because biological molecules consist mainly of light atoms which have very small values for their atomic scattering factors in the high-resolution range. Furthermore, resolutions higher than 0.20 nm enable us to observe the lattice lines of gold crystals which are helpful for the calibration of the instrument. Therefore the specimen stage and the pole pieces of the objective lens of our initial helium-cooled electron microscope were modified to reduce the spherical aberration of the lens from 2.6 mm to 1.9 mm at an acceleration voltage of 400 kV. These modifications improved the Scherzer's limit [8] of the 2nd version of our electron cryo-microscope from 0.26 nm to 0.20 nm.

High-resolution structure analysis of proteins based on electron microscopy requires high-resolution images, including many images from highly tilted specimens. So far, the success rate in collecting high quality images from highly tilted 2D crystals is relatively low. Often the image quality is deteriorated by image drift and/or shift (very rapid drift) which are attributed to the electric charge-up of the irradiated area of the specimen. The low yield of high-resolution images forces us to spend many days on the microscope and to look at many specimens. Ease of operation of an electron cryo-microscope is therefore a tremendous help in the tedious task of electron microscopic data collection and thus very important for the three-dimensional structure analysis of biological molecules.

The superfluid helium stage of our electron cryo-microscope enabled us to collect high resolution images at a stage temperature of 1.5 K and from 4.2 K up to room temperature. However, as described previously [7], at a temperature of 1.5 K we were confronted with a serious problem of high frequency vibration of the stage. The main cause for the stage vibration was overcome by cutting off the turbulent flow of liquid helium through the capillary by heating a part of the capillary just above the BeCu wire inside the capillary near the helium tank. This modification stabilized the stage at 1.5 K and enabled us to record high-resolution images at this temperature. To collect images at 4.2 K, the evacuation of the pot through the exhaust pipe had to be stopped but a fully charged pot of liquid helium was

sufficient to work for 15 minutes; during this time high-resolution images could reproducibly be obtained. However, this method required time to manipulate two valves in order to cool down the pot and to allow the pressure to again rise to atmospheric pressure after evacuation of the pot. This inconvenience was resolved by optimizing the helium flow through the capillary which enables us now to record high resolution images at 4.2 K without further manipulation for up to 5 hours.

A cross section through the 3rd version of our superfluid helium stage is shown in **Fig. 2**. The cryo-stage consists of 4 major parts: the liquid nitrogen tank, the liquid helium tank, the 1.5 K pot, and the specimen stage. The yellowish brown part is cooled by liquid nitrogen and kept below a temperature of about 95 K. The specimen stage is connected to the liquid nitrogen tank by flexible copper braids. The green parts represent the helium tank which is kept at 4.2 K. The blue and dark green areas depict the 1.5 K pot and the specimen holder, respectively. The capillary and exhaust pipe are connected to the pot. Both pot and specimen holder are cooled down to 1.5 K when the helium in the pot is evacuated through the exhaust pipe by means of a big rotary pump, because the liquid helium in the pot changes to the superfluid phase when it is cooled below 2.17 K under a saturated vapor pressure of $4.16 \cdot 10^3$ Pa. There is no temperature gradient across the liquid helium under a finite heat input. Evaporation of helium occurs without formation of bubbles, because the effective thermal conductivity of superfluid helium is extraordinarily high. The pot is mounted on a thermal insulator made of fiber-reinforced plastic (FRP) which is fixed on the specimen stage. The specimen stage is also made of FRP and is firmly connected to the lower part of the thermal shield which is cooled with liquid nitrogen by flexible copper braids. While the stage is thermally very strongly coupled to the nitrogen tank, the mechanical coupling is only very weak. This mechanical uncoupling of our specimen stage from vibration sources such as the nitrogen and helium tanks is a very important feature of the stage.

It should be noted that we constructed and arranged all parts of our cryo-stage, namely the nitrogen tank, helium tank, pot, pot support, upper and lower thermal shields, and flexible copper braids, with an axial symmetry in order to minimize the drift induced by any temperature change in an individual part of the stage. This is one of the main reasons why a top-entry design was chosen for our specimen stage instead of a more commonly used side-entry design. Only a top-entry stage can be constructed symmetrical about the electron-optical axis and this symmetrical construction of the cryo-stage enables us now to record easily and reproducibly images of gold crystals displaying a resolution better than 0.1 nm at a stage temperature of 4.2 K.

The low consumption rates of liquid nitrogen and liquid helium, which are 170 ml/h and 140 ml/h, respectively, is another important feature of our stage. After refilling the two coolants, the working time of our cryo-stage is about 5 hours, during which no maintenance is required. From our experimental perspective,

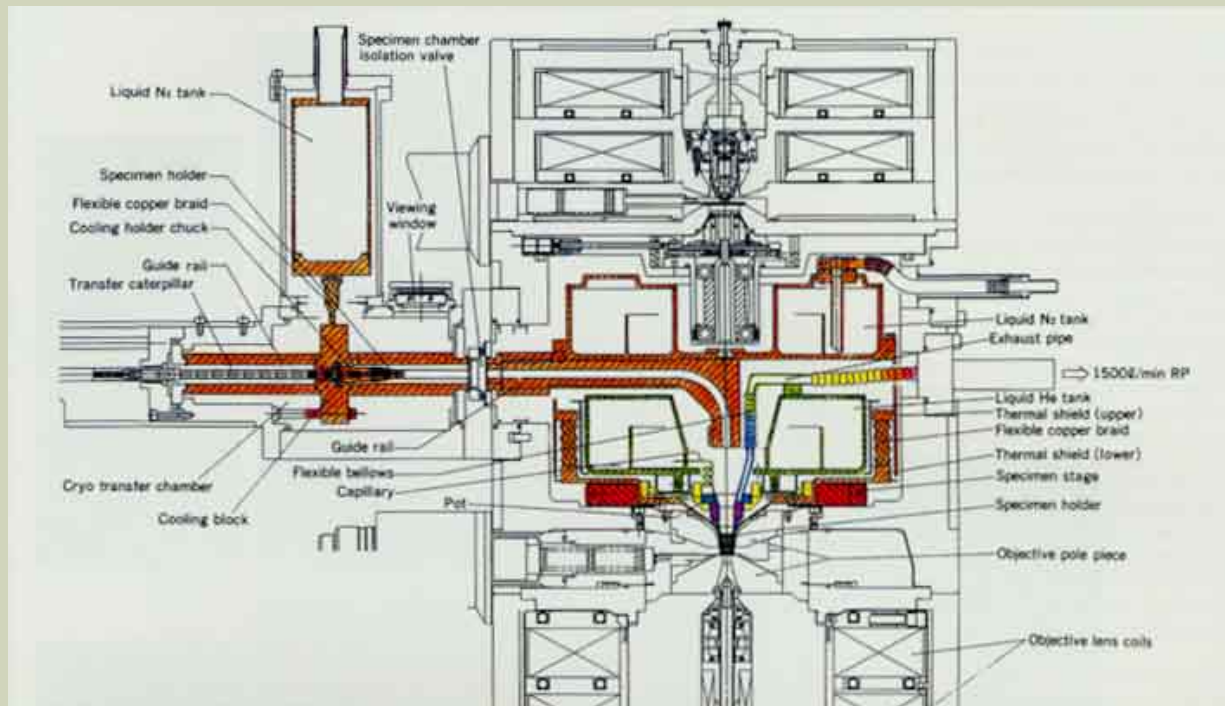


Fig.2. Cross-section through the superfluid helium stage including a cryo-transfer device for the top entry stage of the 3rd version of our electron microscope. The colour in the figure refers to the temperature of the various components of the stage, indicating progressively higher temperatures with the increase in the wavelength of the coloured light (purple indicates the lowest temperature and red the highest one). The yellowish brown parts are cooled to a temperature of about 100 K by liquid nitrogen.

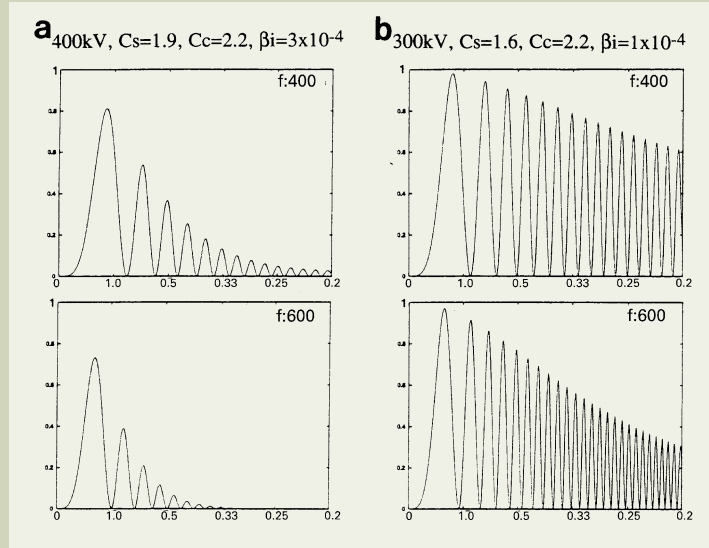


Fig.3. Squared contrast transfer functions (CTF) under two different defocus conditions (400 nm and 600 nm). The attenuation of the CTF due to energy spread and partial coherency is much less pronounced for a field emission gun (b) when compared to a LaB₆ filament (a). Horizontal axis indicates resolution in nm unit.

these low consumption rates are very important for efficient and successful high-resolution electron cryo-microscopy.

The side chains of amino acids are well resolved when the structure can be analysed at a resolution of 0.3 nm or better. The deterioration of the contrast transfer function (CTF) strongly affects the S-N ratio of the Fourier components of images, especially in the high resolution range. The 2nd version of our microscope was equipped with a LaB₆-filament

and the images were clearly affected by the attenuation of the intensity of the CTF, especially in images which were recorded at a high defocus value as shown in Fig. 3 a.

The 3rd and also the 4th version of our electron cryo-microscope, the latter enabling us to observe a larger area of the specimen than the former, are equipped with a 300 kV field emission gun (FEG) which gives less attenuation of the CTF at high-spatial frequency and is therefore more suitable for high-resolution imaging

of biological samples. A biological sample has generally low scattering amplitudes in the high spatial frequency range, because it is composed of light atoms such as hydrogen, carbon, nitrogen, and oxygen. Therefore, biological samples require a coherent electron beam as the one provided by the FEG, which leads to a reduced attenuation of the CTF at high-spatial frequencies even under highly defocused imaging conditions as shown in Fig. 3 b.

Optimizing the specimen preparation is

another very important task remaining in electron cryo-microscopy. Ice-embedding has proven to preserve the specimen structure even under the high-vacuum conditions of an electron microscope. However, specimen preparation is a trial and error procedure as there are no generally applicable rules. For example, optimizing the thickness of the ice film in which the specimen is embedded is purely empirical.

In 1986, we developed a special cryo-transfer device for our top-entry microscope. However, it had a remaining instrumental inconvenience in that it required a long time to exchange the specimen and the handling was difficult. An instrument suitable for high-resolution data collection for electron crystallographic structure determination must provide a fast, smooth, and reliable specimen exchange mechanism. From the user's point of view, the cryo-transfer device is actually one of the most important parts of an electron cryo-microscope; therefore, we spent a lot of time trying to improve the cryo-transfer device. The volume of a liquid nitrogen vessel of a specimen transfer holder was optimized by changing the construction of the specimen transfer device from a bottom setting, which was shown in Fig. 8 of ref. 6, to a side setting (Fig. 2), because the side setting enabled us to minimize the cooling liquid nitrogen for the specimen holder. By using this cryo-transfer device, a new specimen can be placed into the microscope and observed in less than 10 minutes after observation of the previous specimen has been completed.

III. Structure of Bacteriorhodopsin

bR is a membrane protein found in *Halobacterium salinarium* [9] with a bound retinal molecule which serves to absorb light energy. bR functions as a very efficient proton pump and absorption of a single photon by the retinal suffices to transport a proton from the inside of the cell to the outer medium. Many studies have been performed on bR and revealed the functional intermediates of the bR photocycle [10]. Continuing on from the pioneering work with Unwin [3], Henderson was able to determine an electron crystallographic density map of bR at a resolution of 0.35 nm. Based on this 3D map, Henderson and his coworkers built an atomic model of the protein including the retinal molecule [4] and deposited the atomic co-ordinates in the Brookhaven Protein Data Bank (PDB). They, thereafter, improved their atomic model by crystallographic refinement [11]. The atomic coordinates of the resulting new atomic model of bR have also been registered in the PDB (2BRD). We, however, set out to analyse the structure of bR at a higher resolution independent of the structure analysis by Henderson and co-workers, because X-ray crystallography has already achieved structure analysis at much higher resolutions than 0.35 nm, even with some membrane proteins. Moreover, confirmation of the reliability of structure analysis by electron crystallography is still thought to be useful for the method. While Henderson *et al.* proposed a model for the proton transport mechanism within the bR channel [4], we were also inter-

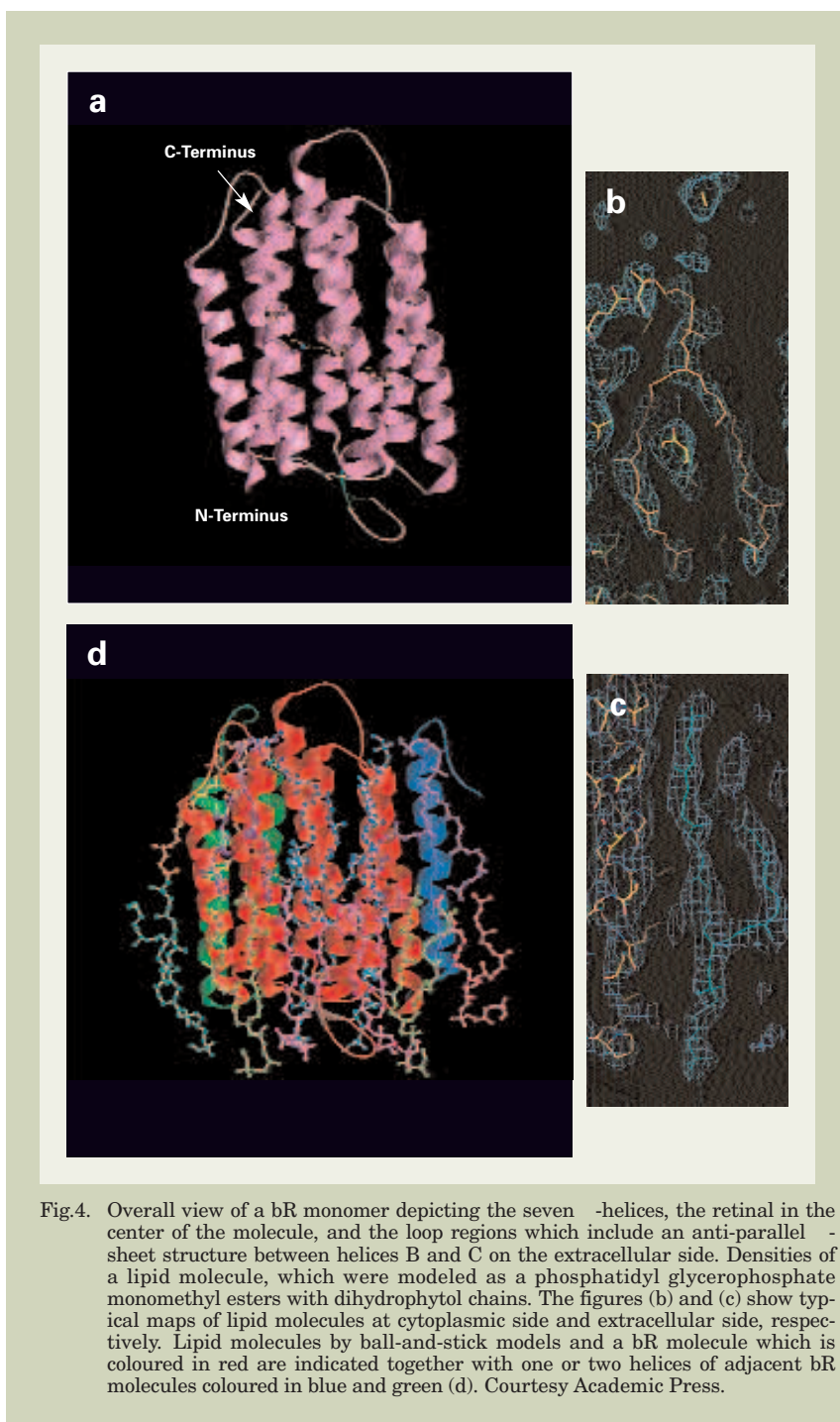


Fig.4. Overall view of a bR monomer depicting the seven α -helices, the retinal in the center of the molecule, and the loop regions which include an anti-parallel β -sheet structure between helices B and C on the extracellular side. Densities of a lipid molecule, which were modeled as a phosphatidyl glycerophosphate monomethyl esters with dihydrophytol chains. The figures (b) and (c) show typical maps of lipid molecules at cytoplasmic side and extracellular side, respectively. Lipid molecules by ball-and-stick models and a bR molecule which is coloured in red are indicated together with one or two helices of adjacent bR molecules coloured in blue and green (d). Courtesy Academic Press.

ested in the mechanisms by which protons are efficiently guided to the narrow opening of the bR channel and by which the protons are released from the other protein surface. For the aim, we tried to clearly analyse the structure of not only the inside of bR molecule but also surface of it. Another goal of our work was to confirm the possibility that electron crystallography could detect the ionization state of charged amino acid residues. We earlier attempted to detect charge transfer on chlori-

nated copper phthalocyanine based on quantitative analysis of the images at 0.18 nm resolution [12]. The results were, however, ambiguous because the lattice constant of this organic crystal is not large enough to yield information in the low resolution range of the electron scattering factors. If the ionization conditions could actually be detected, electron crystallography would be a very promising technique to trace the proton movement along essential amino acids in the bR channel. Detection of

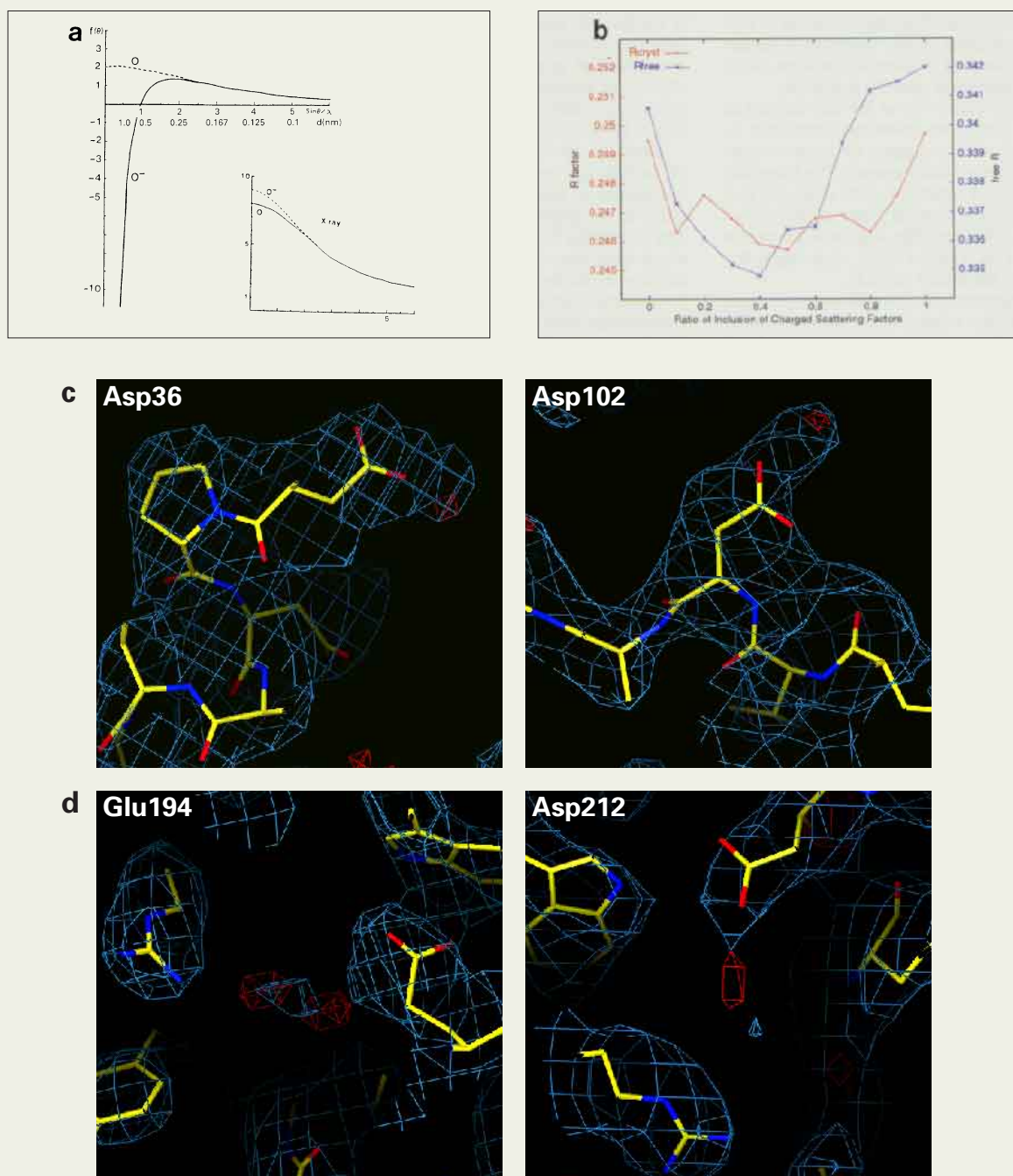


Fig.5. Scattering factors of a neutral (a; broken line) and an ionized (a; continuous line) oxygen atom for electrons (larger graph in a) and for X-rays (smaller graph in a), R-factors and free R-factors calculated using scattering factors of partially charged atoms for carbon and oxygen atoms in the polypeptide carbonyl (b). The R-factors and the free R-factors are shown in red and in blue, respectively. The minimum value for these factors are at the ratios of approximately half charge separation on the carbonyl group (b). Densities above the 3.5 \AA^{-3} level in the $|F_o| - |F_c|$ map around Asp 36, Asp 102, Glu 194 and Asp 212 are shown by red cages and we suggested that these intensities represent positively charged atoms (c, d). No peaks above 3.5 \AA^{-3} were observed in the difference maps calculated without the low-resolution data. The densities in (c) are observed inside the corresponding densities of the $2|F_o| - |F_c|$ maps, which are contoured at the 1.0 \AA^{-3} level indicated in blue, while the densities in (d) have small regions of densities above 1.0 \AA^{-3} of the $2|F_o| - |F_c|$ map that are about 0.1 nm apart from them. We think former type densities represent cations such as sodium or potassium ions and later ones do positively charged Hydrogen ions. Courtesy Academic Press.

the ionization states would tell us exactly the localization of the amino acids to which the proton is bound in the various intermediates of the bR photocycle. The discrimination of ionization conditions is also important to understand the detailed relationship between structure and function of proteins in general.

The high quality of our 3D map enabled us not only to trace the seven transmembrane α -helices but also to interpret all loops in terms of the bR amino acid sequence. The loops displayed distinct structures, such as an anti-parallel β -sheet and quick turns at the end of extended α -helices (Fig. 4 a), which were not visualized by a recent X-ray crystallographic analysis of bR at 0.25 nm [13].

Our experimental 3D map revealed eight lipid molecules related to one bR molecule. In the crystallographic refinement these lipid molecules were modeled as phosphatidyl glycerophosphate monomethyl ester with dihydrophytol chains (Fig. 4 b, c, d) [14] which is a major phospholipid found in purple membranes [15]. Interactions between the molecules in the bR trimer are mainly formed by hydrophobic-hydrophobic contacts of the transmembrane helices, while in the case of LHC-II, the trimer is stabilized primarily by protein interactions just outside of the lipid bilayer.

Analysis of the potential map calculated from our atomic model and the trimer structure including the arrangement of the lipid molecules revealed a characteristic charge distribution on both surfaces of the protein. This characteristic distributions of surface charge of the bR trimer enabled us to propose hypothetical mechanisms for efficient guidance of protons to the small channel entrance opening on one side of the protein and for the efficient release of the protons from the other side. The detailed mechanism was described in previous review [16].

While the scattering factor of a neutral and a charged oxygen atom are very similar for X-rays (Fig. 5 a), they differ greatly for electrons in the low resolution range. The electron scattering factor of a negatively charged oxygen atom even has a negative value in the low resolution range as shown in Fig. 5 a. Therefore, the density of a negatively charged atom in the simulation of a potential map appears weak or even to have a negative contrast, while a neutral oxygen atom creates a clear positive contrast in the potential map. However, such effects should disappear in the potential map if the low resolution data is omitted. This is actually helpful because it allows discrimination between a negatively charged atom and an atom which is neutral but disordered, which both would appear as weak densities in the map. For example, when we recalculated a map using only data from 0.7 nm to 0.3 nm, the initially weak density of a negatively charged atom became much stronger, while the density of a neutral but disordered atom remained weak.

The different appearance of the density of a charged and an uncharged residue could also be observed in the density map of LHC-II [5]. The positively charged Arg side chains were very well defined, whereas there was virtually no density for the Glu side chains even though

they are probably equally well ordered because they participate in the formation of salt bridges. Thus, the invisibility of the density for the Glu side chains may be due to the negative electron scattering factors of negatively charged groups. Most other acidic side chains had similarly poorly defined densities in the map which included the low resolution data of LHC at 0.34 nm resolution.

Based on our refined structure analysis of bR at 0.30 nm resolution, we examined the magnitude of polarization of the carbonyl group in the peptide bonds of the backbone. The scattering factors of partially charged atoms were approximated by a linear combination of scattering factors for neutral and ionized atoms, varying the ratio of the linear combination from 0.0 to 1.0 by steps of 0.1. The R-factors and free R-factors in the refinements were calculated for each value by assuming that all the oxygen and carbon atoms of the polypeptide carbonyl had an equal but opposite charge. The result of these calculations showed that the R-factor and the free R-factor were minimized when the relevant atoms were assumed to have a partial charge of 0.5 and 0.4, respectively, as shown in Fig. 5 b. The two values are very close to the values used in molecular dynamics calculations for partially charged oxygen and carbon atoms in the backbone [17].

We also found strong densities above the 3.5 σ level around some side-chains in our $|\text{Fo}|-|\text{Fc}|$ map, calculated with all data from resolution of 5.4 nm to 0.30 nm. In our three dimensional map of bR, the peaks above the 3.5 σ level were around five acidic residues, Asp 36, Glu 74, Asp 102, Glu 194 and Asp 212 as shown by red contour in Fig. 5 c, d (Glu 74 is not shown). We interpret these densities to reflect positive charges, because they disappeared when the $|\text{Fo}|-|\text{Fc}|$ map was calculated without the low-resolution data. We could, however, not see densities corresponding to positively charged amino acid residues, presumably because they form salt-bridges to negatively charged residues. We grouped these five density peaks in $|\text{Fo}|-|\text{Fc}|$ map into two categories depending on the appearance of the densities in the $2|\text{Fo}|-|\text{Fc}|$ map around the peaks. Two of five densities in the $|\text{Fo}|-|\text{Fc}|$ map, around Asp 36 and Asp 102, were observed inside of intensities above 1.0 level of $2|\text{Fo}|-|\text{Fc}|$ map (Fig. 5 c). We think this type density represents cation such as sodium or potassium ions. The other three densities, around Glu 74, Glu 194 and Asp 212, were visible out of 1.0 level of $2|\text{Fo}|-|\text{Fc}|$ map (Fig. 5 d, Glu 74 is not shown). The density peaks above 1.0 level were observed in $2|\text{Fo}|-|\text{Fc}|$ map about 0.1 nm apart from the densities of $|\text{Fo}|-|\text{Fc}|$ map. We think that these strong densities in the $|\text{Fo}|-|\text{Fc}|$ map (red contour in Fig. 5 c, d) and the accompanying density peaks in $2|\text{Fo}|-|\text{Fc}|$ map (blue contour in Fig. 5 c, d) can be assigned to positively charged hydrogen atoms of a hydroxonium ion or a polarized water molecule and the oxygen atoms of the water molecule, respectively.

If the electron crystallographic analysis of the intermediates could really be achieved in practice, we would be able to create a movie of the proton translocation. Since electron

crystallography can discriminate between the charged and uncharged state of the key amino acid residues in the transmembrane helices of bR based on the characteristic difference of the electron scattering factors, we were able to follow the proton on its passage through the bR channel. Therefore, electron crystallography using high resolution electron cryo-microscope will be able to provide us with new and exciting insights into the structure and function of bR and many other membrane proteins.

Acknowledgments

These studies were performed in collaboration with T. Mizusaki, K. Morikawa, H. Yamagishi, Y. Aoki, H. Kihara and Y. Harada for development of electron cryo-microscope; K. Mitsuoka, T. Hirai, K. Murata, A. Miyazawa, A. Kidera and Y. Kimura for bR. Parts of this work (bR) have been supported by the Japan Society for the Promotion of Science (JSPS-RFTF96L00502).

References

1. Uyeda N., Kobayashi T., Ishizuka K. and Fujiyoshi Y.: *Chemica Scripta*, **14**, 47 (1978).
2. Fujiyoshi Y., Kobayashi T., Ishizuka T., Uyeda N., Ishida Y. and Harada Y.: *Ultramicroscopy*, **5**, 459 (1980).
3. Henderson R. and Unwin P. N. T.: *Nature*, **257**, 28 (1975).
4. Henderson R., Baldwin J. M., Ceska T., Zemlin F., Beckmann E. and Downing K. H.: *J. Mol. Biol.*, **213**, 899 (1990).
5. Kühlbrandt W., Wang D. N. and Fujiyoshi Y.: *Nature*, **367**, 614 (1994).
6. Nogales E., Wolf S. G. and Downing K. H.: *Nature*, **391**, 199 (1998).
7. Fujiyoshi Y., Mizusaki T., Morikawa K., Aoki Y., Kihara H. and Harada Y.: *Ultramicroscopy*, **38**, 241 (1991).
8. Scherzer O.: *J. Appl. Phys.*, **20**, 20 (1949).
9. Oesterheld D. and Stoekenius W.: *Nature New Biol.*, **233**, 149 (1971).
10. Smith S. O., Pardo J. A., Mulder P. P. J., Curry B., Lugtenburg J. and Mathies R.: *Biochemistry*, **22**, 6141 (1983).
11. Grigorieff N., Ceska T. A., Downing K. H., Baldwin J. M. and Henderson R.: *J. Mol. Biol.*, **259**, 393 (1996).
12. Fujiyoshi Y., Ishizuka K., Tsuji M., Kobayashi T. and Uyeda N.: *Proc. 7th Int. Congr. on High Volt. Electron Microsc., Berkeley*, p21 (1983).
13. Peyroula E. P., Rummel G., Rosenbush J. P. and Landau E. M.: *Science*, **277**, 1676 (1997).
14. Mitsuoka K., Hirai T., Murata K., Miyazawa A., Kidera A., Kimura Y. and Fujiyoshi Y.: *J. Mol. Biol.*, **286**, 861 (1999).
15. Kates M., Moldoveanu N. and Stewart L. C.: *Biochim. Biophys. Acta*, **1169**, 46 (1993).
16. Fujiyoshi Y.: *Adv. Biophys.*, **35**, 25 (1998).
17. Brooks B. R., Brucoleri R. E., Olafson B. D., States D. J., Swaminathan S. and Karplus M.: *J. Comp. Chem.*, **4**, 187 (1983).

Transition of JEOL's Semiconductor Equipment, and Future Development



Naoki Date

Director, JEOL Ltd.

Introduction

We of JEOL have a deep relationship with the semiconductor industry. Based on technology that we have fostered over the years, we manufacture a variety of scientific and analytical instruments including transmission electron microscopes. These instruments are widely used as valuable tools for performing basic research in the field of materials and also for establishing production technology in semiconductor production plants.

Particularly, the high-level integration of recent semiconductor devices necessitates the analysis of the structure of each device at the atomic level. Here, the role played by instruments such as high-voltage transmission electron microscopes is becoming increasingly important.

JEOL, as a manufacturer of scientific and analytical instruments, has thus been involved in the semiconductor industry. One instrument that JEOL developed for use in the semiconductor manufacturing industry is an electron beam lithography system employing electron beam technology, which is our basic technology.

Development of an electron beam lithography system, and the semiconductor business

The present Semiconductor Equipment Division had its beginnings when the world's first electron beam exposure apparatus (JEBX-2A), which was developed jointly by JEOL and the Electrotechnical Laboratory of MITI, was delivered to the Electrotechnical Laboratory in 1967. Since then, this system has been used as a basic model, and progressively modified to its present form. The basic technology developed at that time is widely used even today, not only in our own instruments, but also in electron beam lithography systems throughout the world.

In 1975, the JBX-5A was completed, and in 1976 the JBX-6A, a variable-shaped electron-beam lithography system, was completed. After that, the scale of business expanded, and a business base was established. As a result, a semiconductor project was established as a new division. In 1984, this division was named the Semiconductor Equipment Division. The division bears this name even at present.

The JEBX-2A, the first electron beam exposure apparatus, was progressively modified to become the JBX-5A, JBX-6A, JBX-6AIII, JBX-7000MV, JBX-7000MVII, and JBX-9000MV, respectively, to cope with the degree of integration of the most up-to-date devices produced during each era concerned. The pattern overlay accuracy of the JEBX-2A was 1 μm . In contrast, the pattern overlay accuracy of the latest JBX-9000MV is 20 nm, or 1/50 that of the JEBX-2A. As the degree of integration of devices continues to rise in the future, further improvement in accuracy will become necessary.

Ever since the electron beam lithography system was first developed, each new model has been provided with the most up-to-date functions existing at the time, as the fine pattern writing technique for semiconductors. Particularly, JEOL's systems contributed greatly to increasing the memory capacity of the DRAM which Japanese device makers are good at manufacturing.

In order to enlarge our business base, in 1983 we developed a focused ion beam instrument (JIBL-100), and in 1985 developed and put on the market an electron beam line width measuring system (JEPAS-1000). In the midst of this, we put out guidelines for tackling the three domains of measuring and production equipment, knowledge and information service, and research equipment, as new business fields that could enable us to develop toward the 21st century. Also, in 1991 we developed a wafer inspection system (JWS-7000 series) and in 1995 developed a fine process inspection system (JFS-9800 series) that used a focused ion

beam, aiming at gaining an additional foothold in the semiconductor field.

Wafer process inspection system and fine process inspection system

The JWS series is a scanning electron microscope that is designed for process monitoring on semiconductor manufacturing lines in place of an optical microscope. It was developed for the purpose of observing and analyzing foreign matter and defects on wafers, and was used as a tool for improving yield at the commencement of full-fledged production of the 64M/DRAM in 1994. It has contributed greatly to the reduction of the period from the commencement of production at a new semiconductor plant to full-fledged production (vertical fab startup).

A dedicated electron optical system that enables wafers to be observed at high resolution while set at a high tilting angle was developed for the JWS series. Because the JWS was intended for use in semiconductor plants, the entire system, including the stage drive system and the operation system, was based on a concept that was quite different to that of the conventional scanning electron microscope, to ensure high throughput, ease of operation, high reliability (uptime 95% or more), low generation of dust. In addition, there arose demands to automate observation and analysis of defects and dust by means of a coordinate data link with an optical particle inspection system in order to reduce labor. To meet the demands we have added to the JWS series automatic functions such as automatic capturing of defects and dust (ADR), and automatic classification of captured defects and dust (ADC).

The JFS series, on the other hand, is capable of making a vertical hole in the LSI pattern using a focused ion beam, thereby allowing the operator to observe and analyze the cross-section of defects and dust particles using an electron beam or an ion beam, with the large angle



JEBX-2A.



JWS-7555.



JBX-9000MV.

tilting function. The operator can thus obtain a grasp of the internal condition of defects that cannot be known from observation of the external shape. In this way, the system enables the process in which a defect or dust occurred to be determined, and permits more reliable feedback to the manufacturing process. Previously, defect inspection was performed in two stages, namely, cross-section formation using a focused ion beam instrument followed by observation using a scanning electron microscope. This can now be done without any time delay in a single system.

Future development

The smallest line width used in the 64 • 128 M/DRAM, which is the most highly integrated device at present (1999), is between 0.18 μm and 0.15 μm . At the beginning of 2000, this will be reduced to between 0.13 μm and 0.10 μm to cope with increasingly larger memory capacity.

The JBX-9000MV electron beam lithography system was developed for the purpose of making the mask used to manufacture the 256M/DRAM and subsequent devices. However, the line width of the 256M/DRAM

and subsequent devices is close to the limit of the wavelength of light, hence research is being carried out on ARF, KRF, X-rays and other light sources. A direct pattern writing method using an electron beam, which was previously shunned because of its low throughput, is being studied once again, and research is being carried out in various countries, aiming at the realization of a method that can be put into practical application. Methods that are being advocated include the pattern writing method using a multiple electron beam column and the pattern writing method using an electron scattering mask.

Both the JWS and JFS series will, needless to say, require greater resolution along with increasingly high-level integration of devices. Also, because they are used in semiconductor production plants they will be required to have improved reliability and operability and also be automated. In addition, along with increasingly high-level integration, it is becoming necessary to inspect defects and dust that occur during the production process, including those that are less than the pattern width in size. Such defects and dust are close to the limit of the wavelength of light, hence it is becoming necessary

to use an electron beam type defect inspection system instead of an optical type defect inspection system.

As mentioned above, the level of integration of semiconductor devices is approaching the limit of the wavelength of light, and the application of our electron beam technology that we fostered with our sights on the 21st century is becoming indispensable for the manufacture of semiconductor devices. The 21st century will test JEOL's true worth, and will be a century in which we will leap forward.

I have described about the transition of the Semiconductor Equipment Division, and also its future development. Here, I would like to take the opportunity to express my profound gratitude to our customers for the guidance and support that you gave us during the development of JEOL's semiconductor equipment, as well as to all of our predecessors who laid the foundations of the Semiconductor Equipment Division. I intend to continue to strive for further development of semiconductor equipment and ask you for your continued guidance and encouragement.

Application of Semi-in-lens FE-SEM for Chargeless Observation



Youti Yamamoto, Atsushi Yamada, Hiroshi Kazumori, Tsutomu Negishi and Masaki Saito

Electron Optics Division, JEOL Ltd.

We have applied a fully digital field emission scanning electron microscope (FE-SEM), the JSM-6340F, to observe non-conducting surfaces. For leading electrons into the built-in-lens type secondary electron detector (SED), newly developed accelerating and retarding electrodes are installed in the objective lens (OL) to tune the surface potential and applied to observe a diatomaceous earth surface. Further, the JSM-6340F can select ten scan speeds, and under every selected scan speed averaging and integration of secondary electron (SE) image signals are possible. This function is applied to observe an aluminum oxide surface. The backscattered electron (BE) image of an iron oxide surface was observed using a single crystal scintillator BE detector based on yttrium aluminum garnet (YAG).

Introduction

Electron beam bombardment produces electron- and hole-traps in insulators and causes surface charging [1]. The charging polarity depends on the total secondary electron (TSE) yield, which varies with the energy and angle of the incident electron beam [2]. If the TSE yield exceeds unity, the insulator surface is charged positively, while if it is smaller than unity, the surface is charged negatively. In the SE images, it is known that if the charging polarity is positive, the topographic feature of insulator surface can be observed like the conductor surface [3], but if the charging polarity is negative, the observing area is brightened without topographic contrast [4].

In recent years, the integration scale of semiconductor devices and the nanometer fabrication scale of new materials have become smaller and smaller, and for their research and development a high resolution FE-SEM has become indispensable. Since these materials are non-conducting, the minimum electron dose technique and rapid scanning have been applied to prevent the sample charging. For the purpose of easy observation of non-conducting surfaces with high resolution, we have applied a semi-in-lens fully digitalized FE-SEM, the JSM-6340F with multi-functions, to compensate the charging up on the non-conducting surfaces [5].

Experimental

In the JSM-6340F, the electron optics sys-

tem is composed of a cold field emission gun, two condenser lenses, an aperture angle control lens, and a semi-in-lens type OL [5].

The semi-in-lens type OL induces a strong magnetic field on the sample and the field rolls up almost all of the SEs into the OL. A built-in-lens type SED is positioned in the OL. For guiding the electrons into the SED, a set of accelerating and retarding electrodes are installed in the OL as shown in **Fig. 1**. The voltages at these electrodes are selectable in 3 different combinations. These are named as mode numbers "0", "1" and "2", which can be selected appropriately in accordance with the surface potential of insulating, semiconductor or metallic sample.

The detection efficiency of SEs was estimated by computer simulation using the three-dimensional finite difference method. In the simulation, all elements are assumed to be metallic, because the simulation cannot be performed when the surface potential of the sample changes by the charging. It is confirmed that all the SEs are gathered to the SED in the mode "2", where the accelerating voltage is 30V and the retarding voltage -10V. In fact, the S-N ratio of the mode "2" is more improved by a few times of no electrode case in SEM observations. In the mode "1", the accelerating voltage is similar to that of the mode "2" and the retarding voltage is -5V. In the mode "0", the accelerating and retarding voltages are not supplied. The voltages used in the "1" and "0" modes are decided experimentally against non-conducting samples. If the

charging polarity is negative and the ejection energy shifts to higher side, the mode "0" is useful to observe the charging sample.

Compared to the SE image, the BE image of a non-conducting sample is affected by charging to a smaller degree [6]. A single crystal scintillator BE detector based on YAG is installed in the JSM-6340F. The BE detector shows a good S-N ratio at low accelerating voltages, fast time response and chargeless observation.

Results

To eliminate the sample charging, it is necessary to use the minimum electron dose method during observation. Averaging and integration at a fast scan speed is useful in observing non-conducting samples. The combination of electrode potential, dose quantity and scan speed can be selected according to the change in the sample surface potential.

Figures 2 (a), (b), and (c) are SE images of diatomaceous earth. Accelerating voltage of the primary electron beam is 1.5kV, WD 3mm and magnification 10,000. Fig. 2(a) was taken with the mode "1" and single scan at 80s, (b) with the mode "0" and single scan at 80s, and (c) with mode "1" and 64 times integration at 0.28s. The sample is charging up in (a), the charges are almost compensated in (b), and the charges are completely compensated in (c). However, the detection efficiency of SEs in the mode "1" is larger than that in the mode "0". The difference of accelerating voltage between the mode "1" and the mode "0" is a

few tens V, and that of retarding is a few V. The voltages of the mode "0" are lower than the mode "1" in the accelerating electrode and higher in the retarding electrode. Available voltages are set up according to the surface potential of the non-conducting samples. The selection of the modes is the first way of chargeless observation techniques.

It is also possible to select ten scan speeds from 0.28s to 121s in the vertical direction with 1280 1024 pixels and to average and integrate the SE image signals at the selected scan speed. **Figures 3 (a), (b) and (c)** show SE images of aluminum oxide taken with an emis-

sion current of 12 A, accelerating voltage 1kV, WD 2mm and the mode "0". The magnification is 100,000 and single scan is used at 80s in the vertical direction in (a). The magnification is 100,000 and the integration is 128 times at a scan speed of 0.28s in (b), and the magnification is 200,000 and the integration is 128 times at a scan speed of 0.28s in (c). In (a), charging up is almost compensated. In (b) charging up is improved in comparison with that in (a). It is confirmed from (c) that image drift due to mechanical and electric stability of the JSM-6340F is less than 1nm/min.

Figures 4 (a) and (b) show SE and BE

images of an iron oxide surface. The BE image is observed using YAG detector. In the SE image, an anomalous contrast is confirmed. Contrarily, the BE image is not affected by charging. These images are saved using an image filing software, SMILE VIEW installed in an external personal computer connected to the JSM-6340F.

Summary

We have applied a fully digital FE-SEM with multi-functions to compensate the charging up of non-conducting surfaces. Minimum electron dose, variable scanning speed, averag-

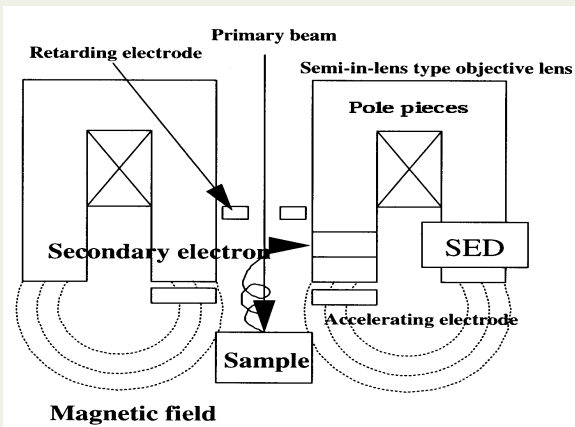
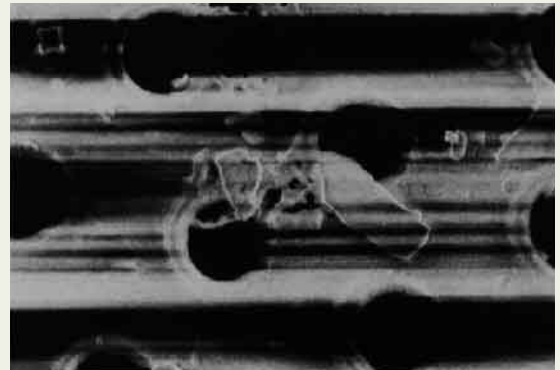
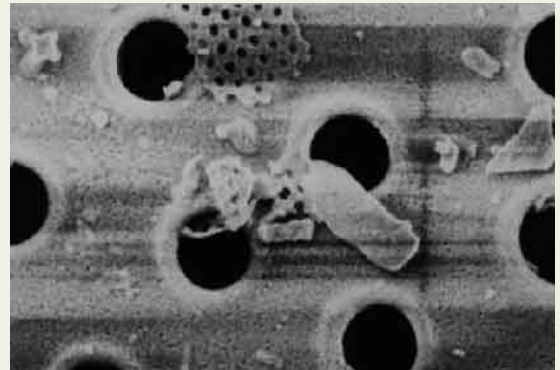


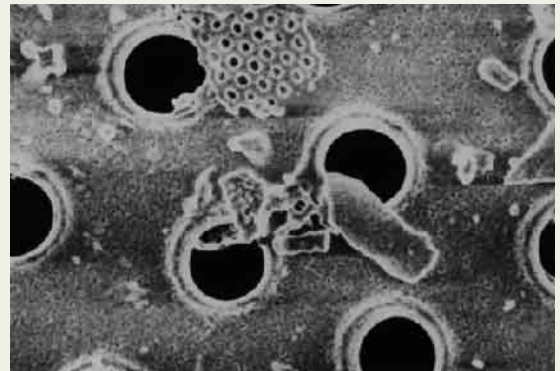
Fig.1. Accelerating and retarding electrodes installed in the OL.



(a)



(b)



(c)

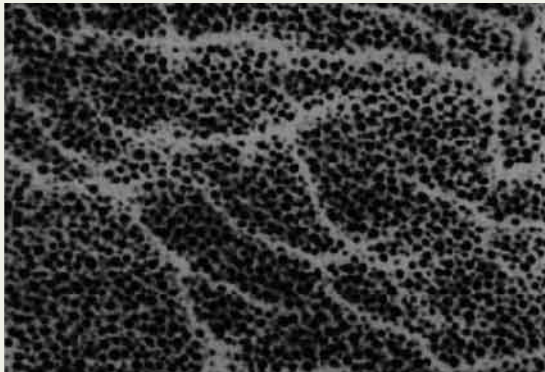
Fig.2. SE images of diatomaceous earth taken at accelerating voltage of 1.5kV, WD 3 mm, and magnification 10,000. (a) the mode "1" and a single scan at 80s, (b) the mode "0" and a single scan at 80s, (c) the mode "1" and 64 times integration at 0.28s.

ing, integration, tuning of surface potential, and cyclotron movements of secondary electrons have been achieved. The JSM-6340F has been successfully applied to observe diatomaceous earth and aluminum oxide surfaces. It is confirmed that the BE image using YAG detector is useful to observe the non-conducting iron oxide surface.

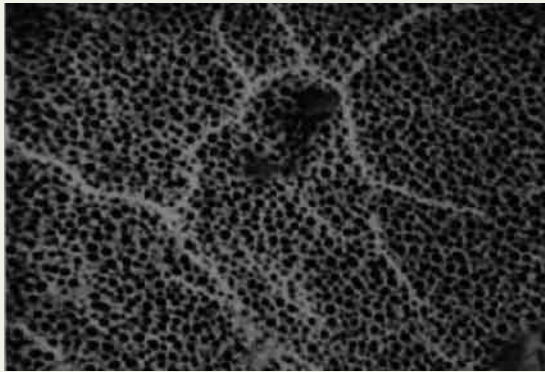
References

1. Vigouroux J.P., Duraud J.P., LeMoel A., LeGressus C.: Electron trapping in amorphous SiO₂ studied by charge buildup under electron bombardment, *J. Appl. Phys.*, **57**, 5139-5144 (1985).
2. Kodama T. and Uchikawa Y.: Conditions of Energy and Incident Angle of Primary Beam for Observation of Insulators' Surface by SEM, *J. Electron Microscopy.*, **41**, 65-69(1992).
3. Postek M.T., Keery W.J., Larrabee R.D.: Specimen biasing to enhance or suppress secondary electron emission from charging specimens at low voltages, *SCANNING*, **11**, 111-121(1989).
4. Brunner M., Schmid R.: Charging effects in low-voltage scanning electron microscope metrology, *Scanning Electron Microscopy* II, 377-382(1986).
5. Yamamoto Y., Yamada M. and Negishi T.: Development of High-Resolution Field Emission Scanning Electron Microscopy with Multifunctions for Chargeless Observation of Nonconducting Surface, *SCANNING*, **19**, 505-511(1997).
6. Autrata R.: Backscattered electron imaging using single crystal scintillator detectors, *Scanning Microscopy*, **3**, 739-763(1989).

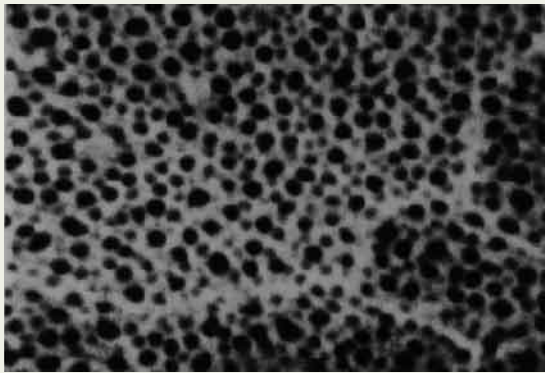
I. Vigouroux J.P., Duraud J.P., LeMoel A., LeGressus C.: Electron trapping in amorphous SiO₂ studied by charge buildup under electron bombardment, *J. Appl. Phys.*, **57**,



(a)



(b)



(c)

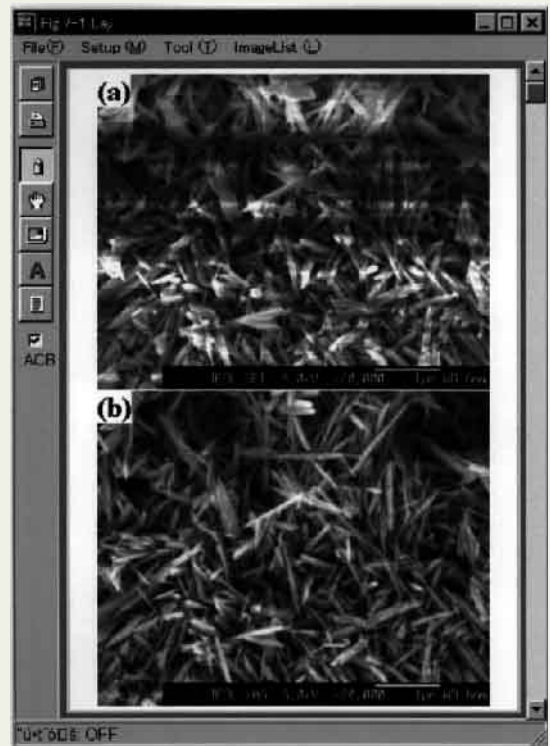


Fig.4. Iron oxide observed at accelerating voltage 5kV and WD 6mm. (a) SE image, (b) BE image.

Fig.3. SE images of aluminum oxide obtained at the mode "0" under emission current of 12 A, accelerating voltage 1kV, and WD 2 mm. (a) magnification 100,000 and a single scan at 80s in the vertical direction, (b) magnification 100,000 and the integration 128 times at a scan speed of 0.28s, (c) magnification 200,000 and the integration 128 times at a scan speed of 0.28s.

Development History of JEOL's Transmission Electron Microscopes



Yoshiyasu Harada

Senior Managing Director, JEOL Ltd.

Introduction

JEOL Ltd. was established for the purpose of developing and commercializing transmission electron microscopes (TEM). The forerunner of JEOL Ltd. was the Denshi Kagaku Kenkyusho, which was established in August 1947. In September, immediately after the establishment of this company, a DA-1 type electron microscope that used an accelerating voltage of 50 kV, a single-stage illumination lens, and a 2-stage image forming lens was developed. Subsequently, in May 1949, the Japan Electron Optics Laboratory Co., Ltd. was established as a breakaway organization of the Denshi Kagaku Kenkyusho, and in 1971 it was renamed JEOL Ltd., the name that it bears today. Development and manufacture of TEMs started in earnest after the establishment of the Japan Electron Optics Laboratory. Since the development of the JEM-1 in 1949, some 8000 TEMs, ranging from small to medium and large instruments, were manufactured and sold over a period of 50 years to 1999. As a TEM manufacturer, we are very proud of the fact that our products are widely used by many customers.

Figure 1 shows the history of the development of TEMs by JEOL. The horizontal axis represents time in decades. Each TEM is classified according to its maximum accelerating voltage, and the number of instruments in each series sold is represented relatively as the area of a circle. As can be seen from this development history, TEMs have been developed from small to medium ones, then from medium to large ones. During this period, both the accelerating voltage and magnification increased, and also the resolution improved. For example, the JEM-1, which was the first TEM that JEOL put on the market, used an accelerating voltage of 50 kV, and had a maximum magnification of 5,000 and a point resolution of 3 nm. The JEM-100C, which was put on the market some

25 years later in 1973, used an accelerating voltage of 100 kV, and had a maximum magnification of 500,000 and a point resolution of 0.3 nm; half a century later in 1999, the JEM-2010F, which is the main TEM used in the field of materials science, uses an accelerating voltage of 200 kV, and has a maximum magnification of 1,500,000 and a point resolution of 0.19 nm. The development of the TEM over the past half century is indeed remarkable.

It is not possible here to mention each and every one of these TEMs in detail. I will therefore describe mainly the design philosophy of the objective lens, which is the heart of a TEM, concerning the JEM-100B, JEM-2000FX, and JEM-ARM1250, which are representative models that JEOL has produced during its history of half a century, while mentioning episodes concerning the development of these models.

JEM-100B Electron Microscope

The JEM-100B (**Fig. 2**) was announced at the European Congress on Electron Microscopy (EUREM) held in Rome in 1968. The design of this instrument was markedly different to that of TEMs produced up to that time. For example, the electron optical system used a 4-stage image forming lens, the evacuation system was automated, and the design and operation were based on ergonomic principles. Particularly, this model was developed with maximum priority given to high resolution, so the objective lens used was an asymmetrical type based on a top-entry stage. In other words, the diameter of the upper pole piece bore of the objective lens was made large and the lower pole piece bore was made small, to enable the specimen holder to be inserted into the pole pieces, and thereby minimize the spherical aberration coefficient (C_s) [1]. As a result, at the 7th International Congress on Electron Microscopy (ICEM), which was held in Grenoble in 1970, we succeeded in showing directly to the participants,

via a binocular magnifier, the 0.34 nm lattice image of graphitized carbon black which was formed on the fluorescent screen of this TEM. The stability of the high voltage power supply, objective lens power supply, specimen stage, and other parts of this instrument was verified, and the JEM-100B came to be acknowledged by the market as a high-resolution TEM. Also, at this conference, two papers were presented, one jointly between JEOL and a university, and the other by JEOL alone.

The first paper, which attracted much attention, was the projected image of a chlorinated copper phthalocyanine crystal photographed using the JEM-100B, which was presented jointly by Professor Uyeda, Institute for Chemical Research, Kyoto University and JEOL [2, 3]. This phthalocyanine crystal was the same kind of organic crystal whose crystal lattice image Menter in Britain first succeeded in observing in 1956 [4]. However, in order to reduce damage caused by the electron beam, chlorinated copper phthalocyanine, a substance obtained by replacing all 16 atoms of hydrogen on the outside of copper phthalocyanine with chlorine, was prepared by an epitaxial method, and used as the observation specimen in the JEM-100B. The observation method selected was a multi-beam interference imaging method in which the diffracted electron beams were acquired into the objective aperture down to the theoretical resolution of 0.34 nm, which was determined by the C_s (≈ 1.4 mm) of the objective lens of the JEM-100B. As a result, we succeeded in observing the projected image of the molecules in the crystal. Subsequently, images that were observed using this method came to be called crystal structure images. The resolution was improved along with the use of higher accelerating voltages, and TEMs were increasingly used to observe crystals of inorganic substances and metals that are relatively undamaged by the electron beam, thus contributing to the field of materials science.

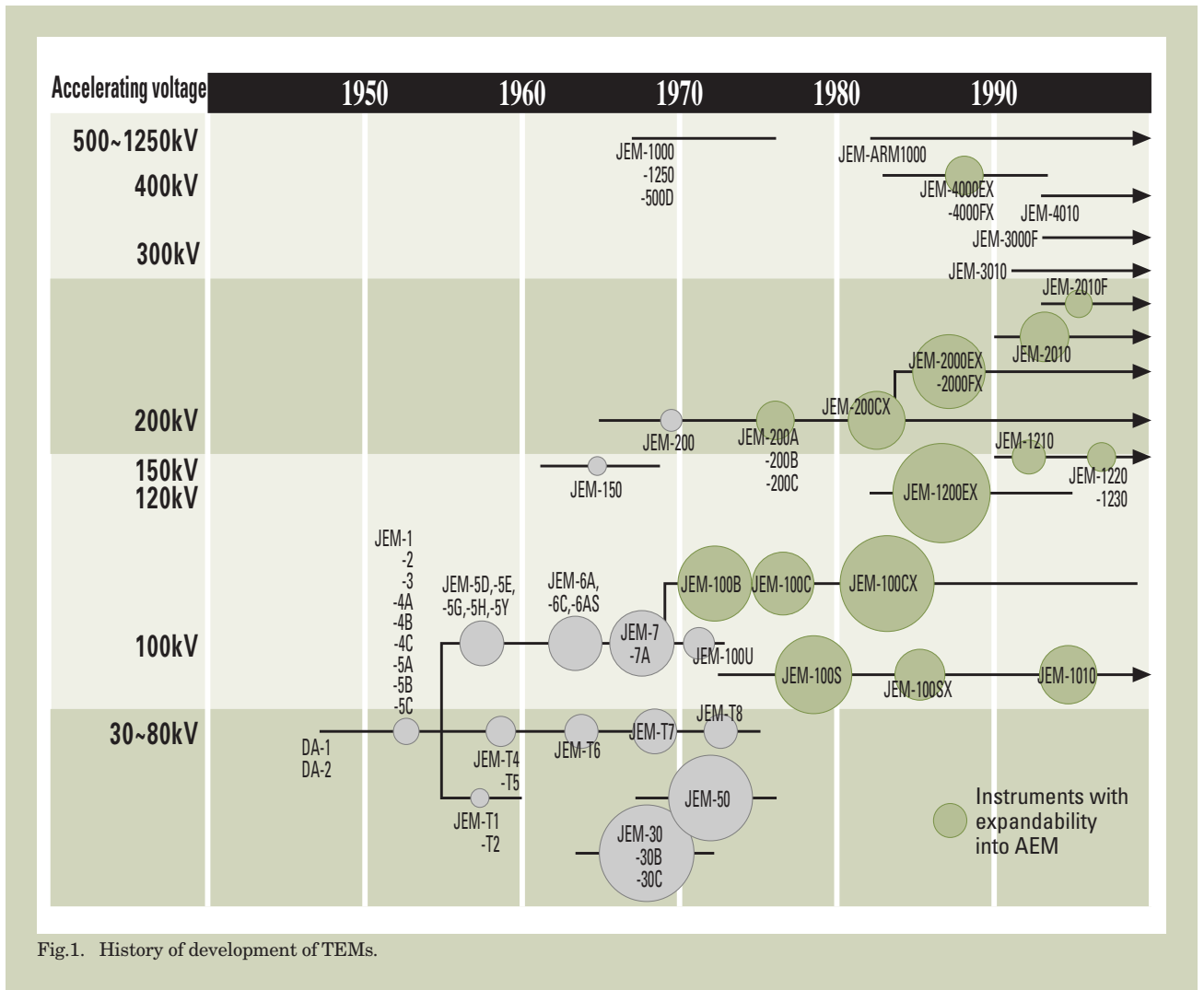


Fig.1. History of development of TEMs.

The second paper was on the research and development of a TEM incorporating the functions of a scanning electron microscope (SEM) [5]. Normally, in a TEM, the specimen is located in the gap between the pole pieces of the objective lens. However, in order to illuminate the specimen with a parallel beam, the objective prefield is made as small as possible, and in order to attain a high resolution the objective postfield is made as large as possible. If the objective lens is strongly excited from these TEM observation lens conditions, the objective prefield will act as a lens, enabling a small electron probe to be created on the specimen. By scanning this electron probe, the secondary electrons emitted from the specimen are confined along the optical axis by the objective prefield. These electrons are detected by the secondary electron detector located above the objective lens, enabling SEM functions to be incorporated in the TEM.

Subsequent to the announcement of this kind of TEM, in October 1970 a scanning image observation device (ASID) was marketed as an auxiliary unit for a TEM. This permitted observation not only of TEM images, but also

of secondary electron images (SEM images) and scanning transmission electron images (STEM images). Also, by installing an energy dispersive X-ray spectrometer (EDS) for analyzing the characteristic X-rays generated from the specimen, on a TEM, it was possible not only to perform observation of TEM images, SEM images and STEM images, for example, but also to acquire data concerning the composition of the specimen from the characteristic X-rays. In this way, the range of applications of the TEM increased considerably [6]. This design philosophy was carried over to the JEM-100C/CX and JEM-200CX models. Subsequently, these instruments came to be called analytical electron microscopes (AEM), and they were further developed to the extent that they are now indispensable in the field of materials science.

JEM-2000FX Electron Microscope

Overseas, in the first half of the 1980s, the Philips EM400T(ST) was gradually conquering the market in the field of materials science, and as a result JEOL was having a hard time

selling its products. The EM400T differed from JEOL's TEM in that it uses a symmetrical Condenser-Objective (C-O) lens [7] as the objective lens, permitting switchover between a TEM image and a SEM/STEM image without any need to change the excitation of the objective lens. In the case of the C-O lens, the objective prefield could be increased by placing the specimen at roughly the center of the lens. This enabled a small electron probe to be easily produced on the specimen, not only in the SEM/STEM mode but also in the TEM mode as well. However, in the TEM mode, because the objective prefield was large, it was difficult to either widen the beam on the specimen or obtain a parallel beam. Philips overcame this problem by placing a mini-lens directly above the C-O lens [8]. In the case of this instrument, when the AEM configuration was used, it was possible in the TEM mode not only to obtain high resolution, but also to obtain a nano-probe. In the TEM mode, EDS analysis and convergent beam electron diffraction (CBED) in the nanometer region were also possible, hence the instrument was highly evaluated in the materials science field.

At that time, JEOL had just commercialized the JEM-1200EX, which employed a 6-stage image forming lens system and a dry vacuum evacuation system and was the first electron microscope to contain a microprocessor for controlling the electron lenses [9, 10]. We were making an all-out effort to increase the degree of perfection of the instrument. Also, we received strong demands from the overseas sales personnel to develop a product that could compete with the Philips instrument. In response to these demands, we concentrated our energies on developing elemental technology that would lead to the development of a new product. In the midst of this situation, the 10th ICEM was held in Hamburg in 1982. JEOL exhibited only the model JEM-1200EX AEM, partly because it was handicapped by the physical remoteness of the convention site. Philips, on the other hand, boldly exhibited a series of products consisting of the EM410, 420 and 430 because of its proximity to the site and also because it was in a rush to put out new products. At that time, we were absolutely dazzled by the power of Philips, and the vexation that I felt is still clearly etched in my memory.

At that convention, our sales personnel and myself engaged in tough negotiations with Professor Gj nnes of Oslo University, who was a world authority on CBED. These negotiations, which took place in the midst of competition with Philips, were aimed at enabling us to obtain an agreement under which we would supply an instrument that would rival the new EM420. During the convention, we carried out tough negotiations with Professor Gj nnes on two occasions. As a result of the negotiations, and also partly because the results concurred with the direction in which we believed that we should proceed, we concluded an agreement to supply an AEM configuration instrument that would have high resolution, a nano-probe, and a CBED function, by January 1984. This agreement was made possible firstly because we had carried out basic tests under a different philosophy to the design of the Philips instrument, which used a mini-lens located directly above the C-O lens, and also because development of the JEM-2000EX [11], which was both the successor to the JEM-200CX and an upper rank JEM-1200EX model, was proceeding smoothly.

For all practical purposes, these negotiations constituted the commencement of commercialization of the JEM-2000FX (Fig. 3), which was the sister instrument to the JEM-2000EX that was completed in 1983. In January 1984, the instrument was tested in the Akishima Factory, and installation was commenced in April. We were able to satisfy the requirements set out by Professor Gj nnes.

The JEM-2000FX was progressively refined while being subjected to the severe appraisal of Professor Tanaka of Tohoku University, an authority on CBED, and finally it was accepted by the market as a TEM that could truly compete with Philips. Like the Philips instrument, the JEM-2000FX used a C-O lens as the objective lens; however, instead of a mini-lens located directly above the objective lens, it had a condenser mini-lens located roughly midway between the objective lens and the condenser



Fig.2. JEM-100B.

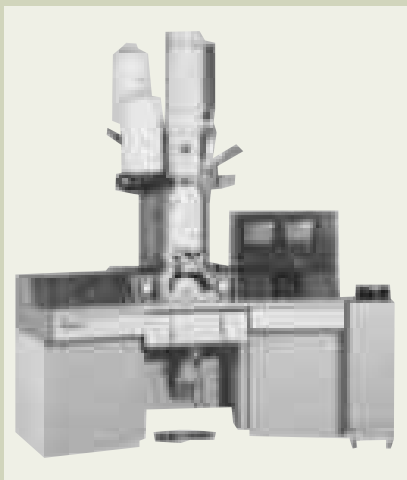


Fig.3. JEM-2000FX.

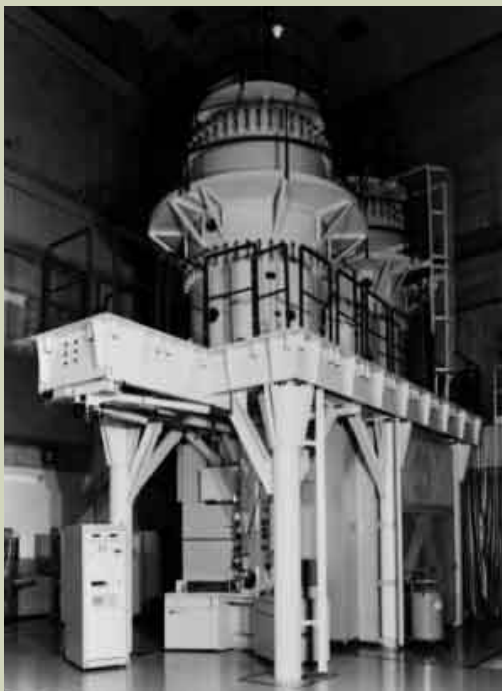


Fig.4. JEM-ARM1250.

lens. This enabled the difficulties attendant to the C-O lens in the TEM mode to be overcome [12]. This design philosophy is also incorporated in the JEM-2010, which is the main model currently used in the field of materials science, the JEM-3010 and JEM-4010, which are high acceleration voltage TEMs, and the JEM-2010F [13] and the JEM-3000F [14], which are provided with a field emission gun (FEG).

JEM-ARM1250 Ultrahigh Voltage Electron Microscope

Between the second half of the 1980s and the first half of the 1990s, we received orders for four ultrahigh voltage TEMs in the domestic market. We also received an order from the German Max Planck Institute (MPI) in June 1986. The order conditions were to actually achieve the theoretical resolution of 0.105 nm at an accelerating voltage of 1250 kV ($C_s = 1.6$ mm). In the case of conventional TEMs, it has been realized to obtain the theoretical resolution, which was determined by the accelerating voltage and the C_s of the objective lens, by means of the optical diffraction method (ODM), only for TEMs that had an accelerating voltage of up to 400 kV ($C_s = 1.0$ mm) [15]. This resolution was 0.168 nm. In the case of an accelerating voltage of 1250 kV, it was considered virtually impossible to attain a resolution of 0.1 nm.

However, we established an in-house project team for the purpose of achieving this aim. This team carried out various studies including those related to technology and production, and commenced manufacturing an actual TEM. We constructed a new building with a large, high performance vibration isolating base, in order to adjust the instrument and confirm that a resolution of 0.1 nm could be obtained in-house as well. The instrument was completed (Fig. 4), and in March 1992 three persons for MPI came to JEOL, and a witnessed inspection prior to shipment of the top entry stage was carried out. The instrument cleared almost all of the inspection items; however, unfortunately the resolution of 0.1 nm could not be achieved. MPI's staff members and JEOL's engineering team jointly carried out various studies in order to find out why it was not possible to attain a resolution of 0.1 nm, but it was not possible to find any apparent reason for this. However, partly because of the situation in Germany, we decided to ship the instrument leaving the most important test item unachieved.

MPI had already completed an excellent installation room that was superior to JEOL's installation environment, and delivery of the instrument commenced in November 1992. Three months later, in February 1993, we were able to verify the electron beam pattern on the screen. Subsequently, we rechecked the receiving inspection items that were performed in-house, one at a time, and finally all that remained was to verify that a resolution of 0.1 nm could be remained. Like the in-house inspection, we found it extremely difficult to obtain a resolution of 0.1 nm. We rechecked all of the factors that could conceivably affect the resolution, such as the electron optical

characteristics, the mechanical stability, the electrical stability, and the specimen conditions, and as a result found that the electrical characteristics, particularly the high voltage stability, were questionable. Under these circumstances, the MPI staff suggested that if noise was being detected, the high voltage could perhaps be made more stable by feeding back the noise. We made a prototype electrical circuit for this purpose, and once again took up the 0.1 nm challenge. We selected the specimen carefully, and took several photographs while changing the focus of the objective lens a little at a time, then checked the developed negative film by means of the ODM, and obtained an optical diffraction pattern that indicated a resolution of 0.1 nm. Next, we used films with different foci, and confirmed that the pattern changed according to theory, and also that the specimen information was definitely transferred to the film. The fact that we achieved a resolution of 0.1 nm for the first time ever was a great source of joy to the persons concerned in both MPI and JEOL.

Subsequently, in November 1993, MPI's staff established a working committee. This committee formally verified the fact that we had completed a TEM with a resolution of 0.1 nm, and that this result was due to the wonderful system of cooperation between MPI and JEOL. Professor Rühle, who was the person-in-charge on the MPI side, signed the receiving inspection sheet, thus enabling delivery of the entire system to be completed within one year. This result is summarized in a paper put out jointly by MPI and JEOL [16].

Conclusion

I have described about three representative models of TEMs that JEOL developed during its 50-year history. At present, the JEM-2010F, which is a TEM with a FEG mounted on it, is widely used in the most up-to-date research in the field of materials science [13]. Also, as a recent trend, TEMs, with an electron energy filter built into the image forming system for eliminating the effect of inelastic scattered electrons from the TEM image and the electron diffraction pattern, have started to appear on the market [17, 18]. At the research level, attention is being paid to correcting the C_s of the objective lens, in order to increase the resolution [19], and it is likely that a TEM with a corrected lens will appear on the market in the near future.

Finally, looking back over JEOL's history of half a century, it is clear that JEOL is a company that has always been based on technology. In other words, JEOL always lends its ear to the voice of the customer, and uses the obtained information in the development of new products. JEOL has also developed TEMs while carrying out joint development with the customer. Here, I would like to take this opportunity to express my appreciation for the valuable guidance and support that we have received from our customers. I believe that the continuing development of technically superior products in the future is JEOL's *raison d'être*. For this reason, I intend to devote myself to the development of products that are useful to the customer, while maintaining a spirit of challenge. I ask you for even more guidance

than that which you have given us over the last half century.

References

1. Yanaka T. and Watanabe M.: *Proc. 6th Int. Congr. Electron Microsc., Kyoto*, Vol.1, p141 (1966).
2. Uyeda N., Kobayashi T., Suito E., Harada Y. and Watanabe M.: *Proc. 8th Int. Congr. Electron Microsc., Grenoble*, Vol.1, p23 (1970).
3. Uyeda N., Kobayashi T., Suito E., Harada Y. and Watanabe M.: *J. Appl. Phys.*, **43**, 5181 (1972).
4. Menter J. W.: *Proc. Roy. Soc.*, **A236**, 118 (1956).
5. Koike H., Ueno K. and Watanabe M.: *Proc. 8th Int. Congr. Electron Microsc., Grenoble*, Vol.1, p241 (1970).
6. Harada Y., Kokubo Y., Goto T., Tamura N., Iwatsuki M. and Koike H.: *JEOL News*, **14c**, 2 (1976).
7. Riecke W. D. and Ruska E.: *Proc. 6th Int. Congr. Electron Microsc., Kyoto*, Vol.1, p19 (1966).
8. Le Poole J. B., van der Mast X. D., and Rakels C. J.: *United States Patent*, No.4,306,149 (1981).
9. Arai Y., Ishida Y., Watabe T. and Harada Y.: *Proc. 39th Ann. Meet. Electron Microscopy Soc. Amer., Atlanta*, p374 (1981).
10. Harada Y., Ishida Y., Arai Y., Ooi K. and Obara Y.: *Proc. 39th Ann. Meet. Electron Microscopy Soc. Amer., Atlanta*, p376 (1981).
11. Tomita T., Iwatsuki M., Arai Y., Ishida Y., Ibe K. and Kersker M.: *Proc. 42nd Ann. Meet. Electron Microscopy Soc. Amer., San Francisco*, p622 (1984).
12. Tomita T. and Harada Y.: *Proc. 11th Int. Congr. Electron Microsc., Kyoto*, Vol. 1 p727 (1986).
13. Honda T., Tomita T., Kaneyama T. and Ishida Y.: *Ultramicroscopy*, **54**, 132 (1994).
14. Bando Y., Kitami Y., Tomita T., Honda T. and Ishida Y.: *Jpn. J. Appl. Phys.*, **32**, L1704 (1993).
15. Hashimoto H., Endoh H., Tomita M., Ajika N., Kuwabara M., Hata Y., Tsubokawa Y., Honda T., Harada Y., Sakurai S., Etoh T. and Yokota Y.: *J. Electron Microsc. Technique*, **3**, 5 (1986).
16. Phillipp F., Höschel R., Oosaki M., Möbus G. and Rühle M.: *Ultramicroscopy*, **56**, 1 (1994).
17. Probst W. Benner G. Bühr J. and Weimer E.: *Advanced Materials*, **5**, 297 (1993).
18. Tsuno K., Kaneyama T., Honda T., Tsuda T., Terauchi M. and Tanaka M.: *J. Electron Microscopy*, **46**, 357 (1997).
19. Haider M., Rose H., Uhlemann S., Schwan E., Kabius B. and Urban K.: *Ultramicroscopy*, **75**, 53 (1998).